

2013-01-01

Application Of Various Remote Sensing And Aerial Photography Data Sets To Resolve Surface Structure In Areas Of Poor Exposure: Examples From Kamchatka Peninsula, Russia And Katalla Area, Alaska USA

Sarah Natalie Heinlein

University of Texas at El Paso, snheinlein@live.com

Follow this and additional works at: https://digitalcommons.utep.edu/open_etd



Part of the [Geology Commons](#), and the [Geomorphology Commons](#)

Recommended Citation

Heinlein, Sarah Natalie, "Application Of Various Remote Sensing And Aerial Photography Data Sets To Resolve Surface Structure In Areas Of Poor Exposure: Examples From Kamchatka Peninsula, Russia And Katalla Area, Alaska USA" (2013). *Open Access Theses & Dissertations*. 1836.

https://digitalcommons.utep.edu/open_etd/1836

This is brought to you for free and open access by DigitalCommons@UTEP. It has been accepted for inclusion in Open Access Theses & Dissertations by an authorized administrator of DigitalCommons@UTEP. For more information, please contact lweber@utep.edu.

APPLICATION OF VARIOUS REMOTE SENSING AND AERIAL PHOTOGRAPHY DATA
SETS TO RESOLVE SURFACE STRUCTURE IN AREAS OF POOR EXPOSURE:
EXAMPLES FROM KAMCHATKA PENINSULA, RUSSIA AND KATALLA AREA,
ALASKA USA

SARAH NATALIE HEINLEIN
Department of Geological Sciences

APPROVED:

Terry L. Pavlis, Ph.D., Chair

Kristine M. Garza, Ph.D.

Jasper G. Konter, Ph.D.

Laura F. Serpa, Ph.D.

Aaron A. Velasco, Ph.D.

Benjamin C. Flores, Ph.D.
Dean of the Graduate School

Copyright ©

by

Sarah Natalie Heinlein

2013

Dedication

This Dissertation is dedicated to my family.

APPLICATION OF VARIOUS REMOTE SENSING AND AERIAL PHOTOGRAPHY DATA
SETS TO RESOLVE SURFACE STRUCTURE IN AREAS OF POOR EXPOSURE:
EXAMPLES FROM KAMCHATKA PENINSULA, RUSSIA AND KATALLA AREA,
ALASKA USA

by

SARAH NATALIE HEINLEIN, M.S.

DISSERTATION

Presented to the Faculty of the Graduate School of
The University of Texas at El Paso
in Partial Fulfillment
of the Requirements
for the Degree of

DOCTOR OF PHILOSOPHY

Department of Geological Sciences
THE UNIVERSITY OF TEXAS AT EL PASO

May 2013

Acknowledgements

I would like to express my gratitude to my advisor, Dr. Terry L. Pavlis, for his guidance and support. With his encouragement and insight he has made me a better geologist. I would also like to thank Terry for introducing me to the magnificent geology of southern Alaska and Death Valley as well as motivating me to pursue my own geology interest in Kamchatka Russia and continue my interest in the Rio Grande Rift. I will always think of him as a mentor and friend.

I would like to thank the remaining members of my dissertation committee, Aaron Velasco, Laura Serpa, Jasper Konter, and Tina Gaza. Each one in their own way gave of themselves to aid me throughout my Ph.D. studies. Aaron always had inspiring words of encouragement, funding, and advice on self-learning. Laura's actions spoke volume to me. Jasper's door was always open for me to ask questions and provided guidance. Tina's divine support picked me up when I needed it the most.

Many individuals have directly or indirectly supported me during my five years in and outside the graduate program at the University of Texas at El Paso (UTEP). This research was supported by a number of National Science Foundation programs; UTEP GK-12 DGE-0947992 and DGE-0538623, PIRE-Kamchatka, STEEP, and UAF. The UTEP Geological Science Department faculty and staff provided inspiration along with computer equipment and software assistance. The UTEP CyberShARE for providing their wonderful facility to me to use. ConocoPhillips and Vernon G. and Joy Hunt Endowed Scholarship Fund also provided support for this research. I would also like to acknowledge NASA for the data granted to me, and ASF support. Thanks to Ph.D. classmates Tina Carrick, Ezer Patlan and Lennox Thompson; Tina for her help with reviews on this dissertation manuscript; Ezer and Lennox for their aid with GMT and other software, and numerous discussions of remote sensing and seismic data resources.

Abstract

For many years now remote sensing data sets and application techniques of these various data have been routinely used in geological studies. Some of these studies are as basic as using Google Earth applications for general reconnaissance to more sophisticated methods for energy exploration or development of active tectonic models for a region. This dissertation presents data from two study areas within the northern pacific region utilizing a number of remote sensing and aerial photography data: 1) Kamchatka Peninsula, Russia, and 2) Katalla area of southern Alaska, USA. The Kamchatka Peninsula, Russia study evaluates surface geomorphology which includes the morphology of faults and diffusion modeling to estimate κ and slip-rates. The Katalla area study evaluates both 1) the surface geomorphology along the Ragged Mountain fault and 2) mapping bedrock geology. These regional maps can be used to develop 3D and 4D models either directly through 3D visualization or through reconstruction of cross-sections to develop a 3D model. The results show that these data sets allow construction of improved regional maps of bedding, and fault traces in areas of poor outcrop.

Table of Contents

Acknowledgements.....	v
Abstract.....	vi
Table of Contents.....	vii
List of Tables	ix
List of Figures.....	x
Chapter 1: Kumroch Fault - Kamchatka Peninsula, Russia.....	1
1.1 Abstract.....	1
1.2 Introduction.....	3
1.3 Tectonic Setting.....	7
1.4 Previous Work.....	9
1.5 The Study Area: Kumrock Fault.....	11
1.6.1 Methods: Morphologic Dating.....	14
1.6.2 Methods: The datasets	17
1.7.1 Results: Morphologic Dating.....	21
1.7.2 Results: Observations from the datasets	25
1.8 Discussion.....	29
1.9 Conclusion	33
1.10 Summary.....	34
Chapter 2: Ragged Mountain - Katalla Area, Alaska.....	35
2.1 Abstract.....	35
2.2 Introduction.....	36
2.3 Tectonic Background and Rrevious work	37
2.4 The SStudy Area: Ragged Mountain.....	40
2.5 Methods	45
2.5.1 Method: The Datasets	45
2.5.2 Method: 3D Virtual Mapping and Surveying.....	47
2.6 Results of Investigation - 3D Virtual Mapping and Surveying	50
2.6.1 The Nature of the Ragged Mountain fault scarp	50
2.6.2 The Quaternary Geology Along the Trace of Ragged Mountain	55
2.6.2.1 Slope Map Analyses	64

2.6.2.2 Topographic Profile Analyses	65
2.6.2.3 Kinematic Model for the Ragged Mountain fault system	68
2.7 Discussion.....	72
2.7.1 Pros and cons of virtual mapping approaches in this study.....	73
2.7.2 Slip sense problem for the Ragged ountain scarp based on geomorphology	74
2.7.3 Application of the fault flexure model for the extensional scarp	80
2.7.4 Fault Slip Rate on Ragged Mountain fault	82
2.8 Conclusion	82
2.9 Summery.....	84
References.....	86
Vita.....	100

List of Tables

Table 1.1:	23
------------------	----

List of Figures

Figure 1.1:	3
Figure 1.2:	5
Figure 1.3:	6
Figure 1.4:	12
Figure 1.5:	18
Figure 1.6:	21
Figure 1.7:	22
Figure 1.8:	23
Figure 1.9:	24
Figure 1.10:	26
Figure 1.11:	28
Figure 1.12:	32
Figure 2.1:	37
Figure 2.2:	41
Figure 2.3:	42
Figure 2.4:	44
Figure 2.5:	47
Figure 2.6:	49
Figure 2.7:	50
Figure 2.8:	52
Figure 2.9:	54
Figure 2.10:	55
Figure 2.11:	61
Figure 2.12:	63
Figure 2.13:	65
Figure 2.14:	65
Figure 2.15:	67
Figure 2.16:	69
Figure 2.17:	70
Figure 2.18:	71
Figure 2.19:	72
Figure 2.20:	76
Figure 2.21:	78
Figure 2.22:	79
Figure 2.23:	80

Chapter 1: Kumroch Fault - Kamchatka Peninsula, Russia

1.1 Abstract

Remote sensing data sets are widely used for evaluation of surface manifestations in active tectonic areas. This study utilizes ASTER GDEM and Landsat ETM+ data sets with Google Earth images draped over terrain models. This study evaluates the surrounding surface geomorphology of the study area with these data sets and the morphology of the Kumroch Fault using diffusion modeling to estimate diffusion constants (κ), as well as to estimate slip-rates by means of real ground data measured across fault scarps by Kozhurin et al. (2006). The study area is located southeast of the Bezymianny Volcano within the Central Kamchatka Depression. It is part of the Kumroch Fault Zone. The area contains numerous geomorphic features indicative of active deformation, such as fault scarps, ponds, offset streams, and glacier moraines. The ASTER GDEM and Landsat ETM+ data together with Google Earth imagery were used to create accurate geomorphic maps of specific sites within the study area along the western flank of the East Kamchatka Range. Previous studies have estimated the time elapsed since slip initiation of the faulted surface on the Kumroch Fault and the slip-rate by dividing the offset of moraines by the age of the ruptured surface. Slip-rates along the Kumroch Fault vary from 2.0 mm/yr – 2.5 mm/yr, determined from previous C^{14} studies with time frames of 11.5 ka to 14 ka. Other slip-rates for the Kumroch Fault were determined from previous studies through tephra and stratigraphic chronology. These produced rates of 0.6 mm/yr, with time frames of 3.2 ka – 10.5 ka. Models of the evolution of fault scarp morphology provide the amount of time elapsed since slip initiated on a faults surface. They may therefore provide more accurate estimates of slip-rate than those calculated by dividing scarp offset by the age of the ruptured surface. Profile modeling of scarps collected by Kozhurin et al. (2006) show that the scarps were formed by several events distributed over time. They were evaluated using a constant slip-rate (CSR) solution which yields a value A/κ (1/2 slip rate/diffusivity). Time elapsed since slip initiated on the fault is determined by establishing a value for κ

and measuring total scarp offset. For this study, CSR nonlinear modeling assisted in estimates of κ which along the Kumroch Fault range from $8\text{m}^2/\text{ka} - 14\text{m}^2/\text{ka}$. Slip-rates have been estimated to range from $0.6\text{ mm/yr} - 1.0\text{ mm/yr}$ since $3.4\text{ ka} - 3.7\text{ ka}$. This method provides a quick and inexpensive way to gather data for a regional tectonic study and establish estimated rates of tectonic activity.

1.2 INTRODUCTION

The Geophysical Institute at the University of Alaska Fairbanks (UAF) has been working alongside the Institute of Volcanology and Seismology in Russia through an NSF program known as Partnerships in International Research and Education (PIRE). The PIRE-Kamchatka project focuses on studying the causes and mechanics of explosive volcanism and sector collapse of the Bezymianny and Shiveluch volcanoes, located in northeastern Kamchatka Peninsula of Russia (Figures 1).

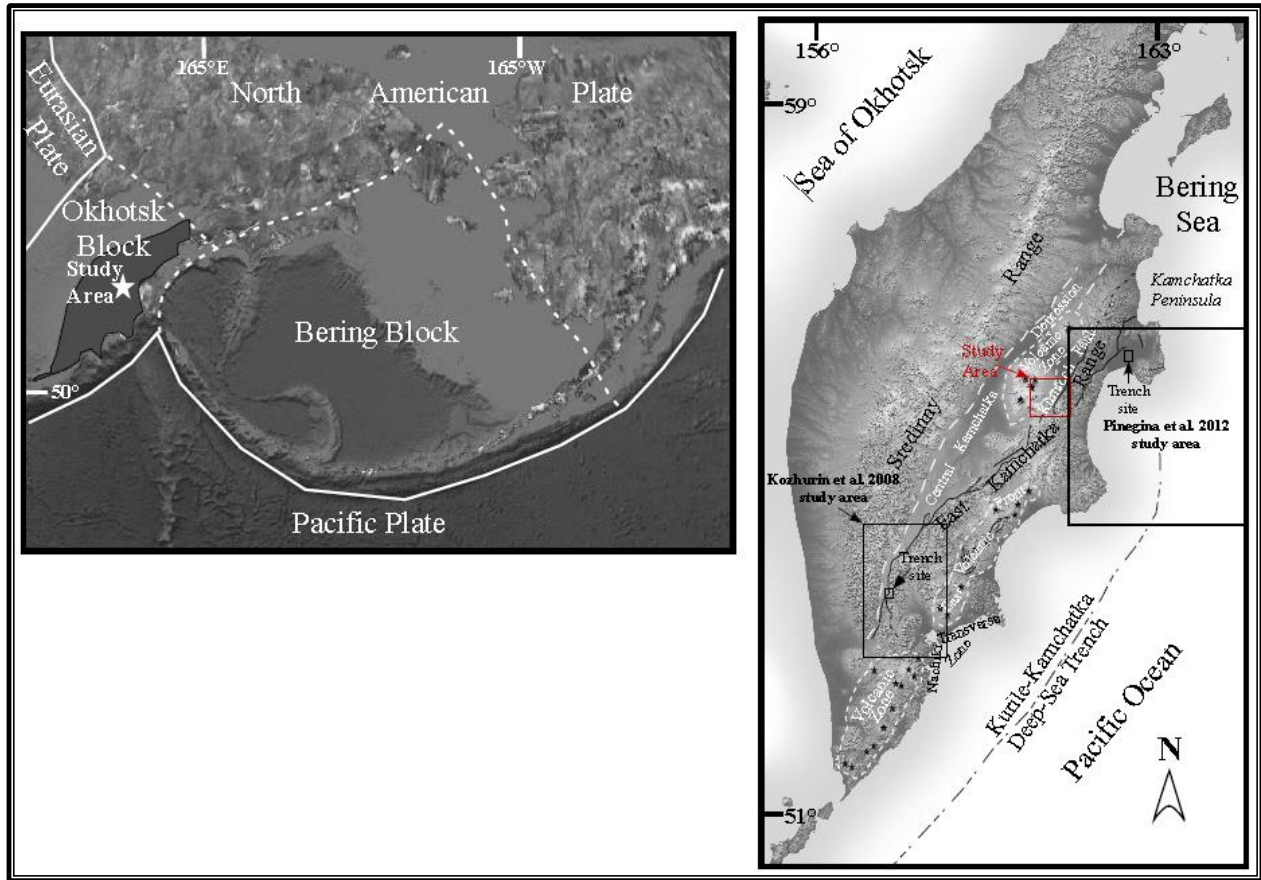


Figure 1.1: Inset map shows Bering Block regional tectonics. White lines indicate plate boundaries. Dashed white lines indicate assumed plate boundaries. Black outlined polygon marks the area of the Kamchatka Peninsula. White star indicates study area. Figure reproduced and modified from Google Earth 2011. Large map shows major Neotectonic elements of the Kamchatka Peninsula. Solid black lines are active faults. Dashed lines are inferred faults. Black stars mark major Holocene volcanic centers. Areas bounded by dotted white lines are volcanic zones. Large thick black box location of Pinegina et al. 2012 study area, smaller black box within the Pinegina study area is location of their 2012 trench site. Large thin black box is location of Kozhurin et al. 2008 study area, smaller black box within the Kozhurin study area is the location of their trench site. Red box is the location of this articles study area. Image modified from NASA and Kozhurin et al. 2006 paper.

The results presented in this paper reveal new details on fault scarp morphology within this important region. These details have major implications in evaluating the active tectonics, including volcanic and earthquake potential, thereby furthering the overall goal of the PIRE-Kamchatka project by contributing to the Kamchatka regional geological background and active deformation history. There is a remarkable rarity of Quaternary scarps that can be directly associated with major faults in the system, given the abundant evidence for active deformation in the region. Not only is the region volcanically active, it is also seismically active (Figure 2). Numerous seismic studies have already been conducted in the region, examining the double Wadati-Benioff seismic zones, the structure of the Kamchatka subduction zone, volcanic eruptions in the region, and tomography, all of which were used to aid in the interpretation of this study (DeMets et al., 1990; Kao & Chen, 1994; Gorbatov et al., 1997; Gorbatov & Kostoglodov, 1997; Mackey et al., 1997; Gorbatov et al., 1999; Eichelberger & Izbekov, 2000; Izbekov et al., 2002; Izbekov et al., 2004; Belousov et al., 2007; Ruppert et al., 2007; Potnyain & Manea, 2008). Only a few studies of paleoseismology, structural geology (some of which were done through photogrammetry), plate interactions, volcanology, and tephrochronology have been conducted in the study area (Kozhurin, 1990; Kozhurin, 2004; Kozhurin et al., 2006; Pedoja et al., 2006; Kozhurin, 2007; Pinegina et al. 2012).

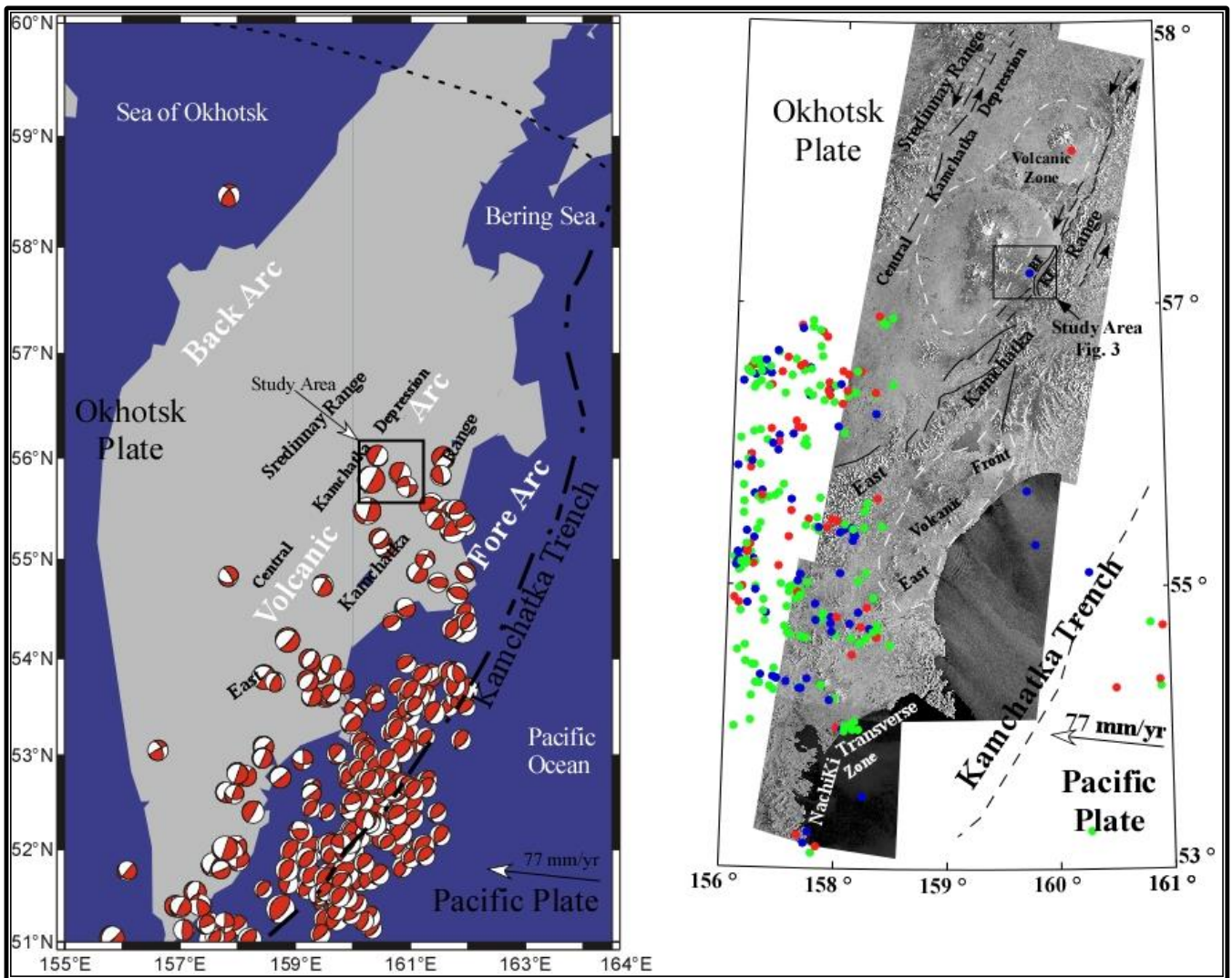


Figure 1.2: Large map (left) showing regional tectonics of the Kamchatka Peninsula and seismic focal mechanisms distribution indicating that the study area has both normal and strike-slip motion. Hillside shaded relief of Synthetic Aperture Radar (SAR) data of the study area and surrounding region in the Kamchatka Peninsula, Russia modified, from the UAF. Blue dots indicate deep seismicity (35-80 km), green dots indicate mid to deep seismicity (10-35km), and red dots indicate shallow seismicity (0-10 km). Seismic data is from the International Seismological Centre. Small white dashed line indicates Central Kamchatka Depression (CKD). Large white dash polygon lines indicate volcanic zones. Solid black lines indicate known active faults and black arrowheads indicate dextral motions. Black dashed line indicates Kamchatka trench and open arrowhead shows the direction of convergence. Images show how seismically active the region has been in the last 5 years.

The area is located southeast of Bezymianny Volcano within the Central Kamchatka Depression (CKD) and includes a part of the Kumroch Fault Zone (KFZ) (Figure 2). Two surface ruptures, one of known age (11.5 ka to 14 ka) and the other of unknown age, and the surrounding surface features are the focus of this study. These features trend parallel with the Bol'shaya Khapitsa River Valley, NE – SW

(Figure 3). The Kumroch Fault (KF) is a well-studied and well-dated fault that was used as a calibrator to explore geomorphic diffusion equation analysis methods. The fault with the rupture of unknown age is referred to here as the Bezymianny Fault (BF) scarp and is known to have ruptured multiple times in the Holocene. In this study basic geomorphic surface structures such as the trace of the KF and BF were identified through 3D virtual mapping and with the use of anaglyph 3D models to classify other active surface features using Advanced Spaceborne Thermal Emission and Reflection Radiometer (ASTER), Global Digital Elevation Model (GDEM) Version 2, and Landsat Enhanced Thematic Mapper Plus (Landsat ETM+) data sets with Google Earth Pro images draped over the data sets terrane models. These models aided in the description of the Holocene and Historic paleoseismic history, and the active tectonics and geomorphic evolution.

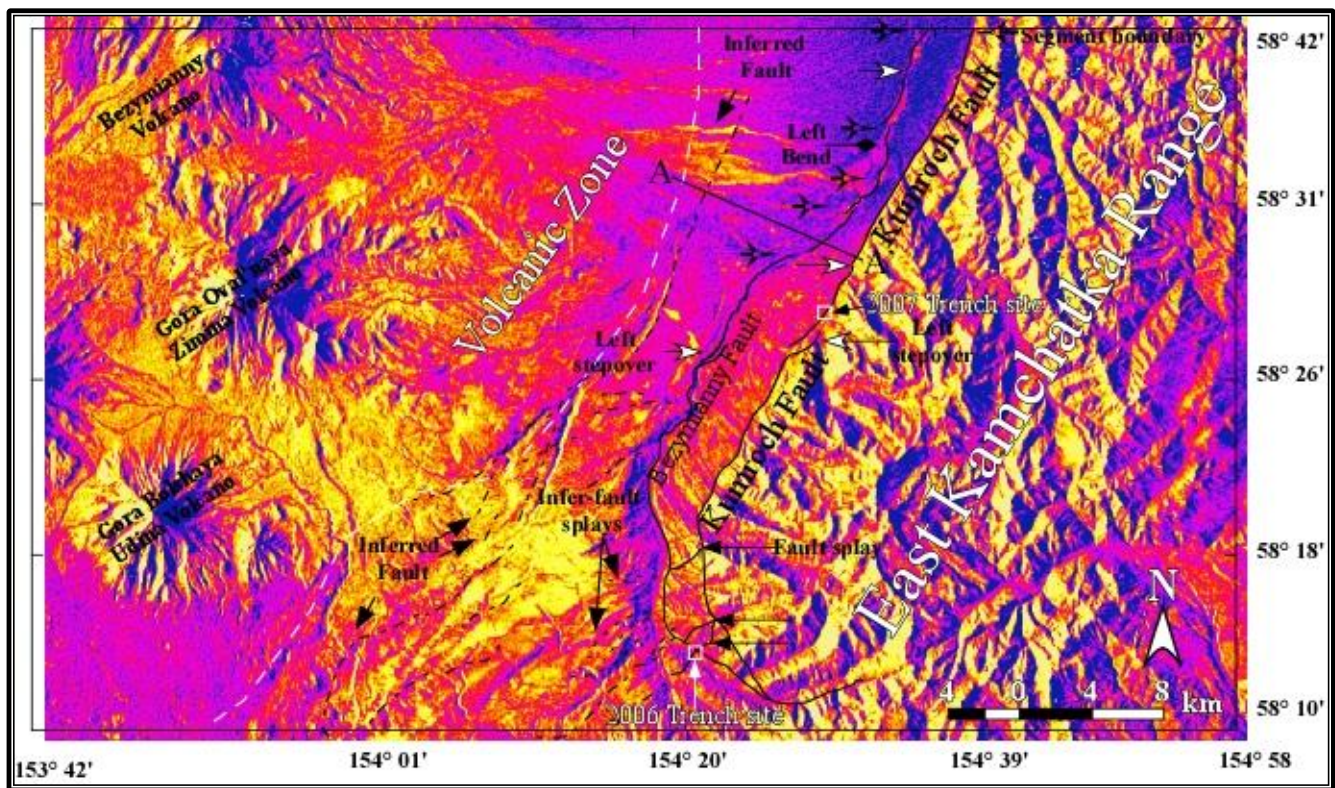


Figure 1.3: Map showing surface features observed during 3D virtual mapping. Long black arrows indicate fault splays, arrows with white arrowheads are left stepovers, and black arrows with hole in center of arrowhead indicate segment boundaries. Large black arrows are inferred faults or inferred fault splays. Black diamond arrows indicates left bend. Segments of the Kumroch Fault (KF) and the Bezymianny Fault (BF) are indicated by heavy black lines. Note both the KF and BF left bend geometry in the south portion of the map. Holocene volcanic centers (areas bounded by heavy white

dashed lines) are volcanic zones. Image modified from 27 m SAR image draped over Landsat ETM+ band 8 data. Image can be view with ChromaDepth 3D glasses.

The research begins by identifying tectonic geomorphic surface features, followed by the production of topographic profiles through computer application software. These are used to describe the surface expressions in the study area. Geomorphic diffusion analyses are used to establish diffusion constants (m^2/ka) along the KF and within the region, with previously collected real ground data from Kozhurin et al. 2006; Kozhurin, 2007; Kozhurin et al. 2008; and Pinegina et al. 2012. Determination of these geomorphic surface features, patterns, and timing assist in the understanding of active faulting associated with the active tectonics. 3D virtual mapping and geomorphic analysis for this region are then compared and evaluated to previous studies conducted in the region and summarized.

1.3 Tectonic Setting

The Kamchatka-Kurile subduction zone (Figure 1) marks the northwestern margin of the Pacific plate (PAC). It is one of the most seismically active tectonic margins in the world (Gorbatov et al., 1997; Kozhurin et al., 2006; Ruppert et al., 2007; Potnyain & Manea, 2008). The zone extends for ~2,000 km from the Bering Sea in the north to Hokkaido Island in the south. Along the Kamchatka-Kurile arc (Figures 1 and 2), the plate motion is almost purely convergent. In the Kurile and Kamchatka, relative plate motions are ~8–9 cm/yr (DeMets, 1992; Ruppert et al., 2007). The Kamchatka Peninsula lies in the interior of the northern end of the Kamchatka-Kurile trench, close to the junction with the Aleutian-Komandorsky chain that is believed to be colliding with Kamchatka at the Kamchatsky Peninsula Cape (Geist & Scholl 1994; Gaedicke et al., 2000; Kozhurin et al., 2006).

Some argue that the Kamchatka Peninsula (Figure 1) belongs to either the North American plate (DeMets et al., 1990; Kozhurin et. al., 2006; Pedoja et al., 2006) or to the separate Okhotsk plate that may be bounded in the north by either the North American plate or the Bering microplate (Kozhurin et al., 2006; Pedoja et al., 2006). The Kamchatka Peninsula is above the westward-dipping subducting slab

of the PAC (Gorbatov et al., 1994). The slab dip decreases from 55° to 35° at its northern end, with the probable loss of a slab fragment. This loss produces a westward step in the volcanic front with the formation of the volcanoes of the Kliuchevskoy group and the more isolated Shiveluch volcano (Yogodzinski et al., 2001; Levin et al., 2002; Park et al., 2002; Kozhurin et al., 2006). These volcanoes began to develop at $\sim 2\text{Ma}$ (Figures 1 and 2) and have been active in the 20th century (Izbekov et al., 2002). The relative plate motion changes from underthrusting of the PAC at the Kuril-Kamchatka arc to strike-slip motion along the Aleutian arc at the junction of the Kamchatka and Aleutian trenches (Gorbatov et al., 1997; Ruppert et al., 2007).

The subduction process is accompanied by a chain of active volcanoes along the Kamchatka subduction zone (KSZ). There are two bathymetric structures related to this subduction zone, the Meiji seamounts and the Kruzenstern fracture zone (Gorbatov et al., 1997). The Meiji seamounts, which are the northernmost segment of the Emperor Seamounts chain, enter the Kamchatka trench at $\sim 54^{\circ}\text{N}$ (Gorbatov et al., 1997). This is the most prominent bathymetric feature being subducted. The Kruzenstern fracture zone subducts at $\sim 52^{\circ}\text{N}$ (Gorbatov et al., 1997).

The Kamchatka Peninsula contains about 30 active volcanoes and hundreds of monogenetic vents, according to personal communications with Dr. Pavel Izbekov in August 2009. Earthquakes within the overriding plate above the subduction zone are rare, usually of moderate magnitudes (Gordeev et al., 2004), and show no clear correlation with the major fault system of Kamchatka (Kozhurin et al., 2006). The current structure and tectonics of Kamchatka are reflected in the topography (Kozhurin et al., 2006) and reveal margin-parallel uplifted and subsided blocks, a regime replacing the thrust dominated pre-Pliocene tectonics related to terrane collision (Konstantinovskaya, 2003; Kozhurin et al., 2006).

The structures of the CKD in Figures 1 and 2 contain two ranges. The Sredinny Range to the west and the East Kamchatka Ranges to the east are separate elevated zones made up of three

promontories on the eastern side of the peninsula (Kozhurin et al., 2006). Southern Kamchatka is much less structurally and topographically differentiated. Its northern boundary can be drawn along the NW–SE striking lineament known as the Nachiki Transverse Zone (NTZ), which terminates at the southern end of the CKD (Figures 1 and 2).

Kozhurin et al. (2006) describe the CKD as asymmetric with a gently sloping flank to the west and a steep faceted flank to the east. The CKD depression to the north is volcanically active, but to the south it is free of volcanism. Formation of the CKD dates back to at least the Late Pliocene and its present morphology developed mainly during the middle-late Quaternary (Melekestsev, 1974; Kozhurin et al., 2006).

1.4 Previous work

In 2006, Kozhurin et al. presented trenching data on Holocene faulting events along the KF and found that none of the data permitted any comprehensive correlation to volcanic activity. They did, however, compare at least some of the dated faulting events to the eruptive histories of adjacent volcanoes. Studies by Russian scientists Svyatlovsky (1967); Tikhonov (1968); Erlich (1973, 1974); Legler (1976); Kozhurin (1988, 1990, 2004) identified, mapped and characterized active faults above the subduction zone, especially during the Holocene volcanic arc development. These studies help to refine the geology of the area and aid in the understanding of the tectonics and geodynamics of this plate boundary. In particular, their applicability includes estimates of tectonic deformation rates, seismic hazard evaluation, and relationship with volcanic activity in the arc (Kozhurin et al., 2006).

Some have argued that the overriding plate of the Kamchatka volcanic arc and subducting plate have strong coupling (Gorbatov et al., 1997; Kozhurin et al., 2006). This coupling is suggested by the frequent high-magnitude earthquakes in the region (Figure 2). Volcanism is also widespread and displays a high rate of magma output (Fedotov & Masurenkov, 1991; Kozhurin et al., 2006). Of the

numerous studies carried out on recent tectonics in Kamchatka, many have been on various aspects of the subduction process (Kepezhinskias, 1987; Hochstaedter et al., 1994; Fedorov & Shapiro, 1998; Levin et al., 2002 & Kozhurin et al., 2006).

Kozhurin et al. (2006) Kozhurin (2007) and Kozhurin et al. (2008) and Pinegina et al. 2012 have been the only field-based structural Neotectonics studies done within the study area and the Kamchatka Peninsula region. Kozhurin et al. (2006) used structural evidence of past earthquakes, combined with known volcanic eruption markers, to reconstruct a paleoseismic history. Kozhurin et al. (2006) methodology combines field and aerial photographic examinations of fault structures and offset features, detailed studies of tephra stratigraphy within artificial and natural exposures, ^{14}C dating, and logging of trench wall exposures created in excavations across active fault scarps. The results allowed them to define a major active fault system crossing the Kamchatka Peninsula, characterize its kinematics and geometry, and document the occurrence of several major Holocene faulting events.

Kozhurin et al. (2008) conducted geomorphic studies examining major Quaternary depressions and active faults south of the CKD (Figure 1). Within these depressions, loose sediment accumulation was observed and a number of faults were identified and described (Kozhurin et al. 2008). The trench site was located in the Poperechnaya valley where observations were made of a number of Quaternary flood terraces, low fluvial terraces, aprons, shallow washouts, surfaces of fluvioglacial material (of the second phase of the Late Quaternary glaciations), fluvioglacial sediments (flatland), Late Pleistocene moraine, and portions of active faults with the early Holocene Most Recent Event (MRE) movements (Kozhurin et al. 2008). The trench itself was dug in respect to fluvioglacial terrace risers and a Holocene fault scarp.

The Pinegina et al. (2012) study examined seismic and tsunami hazard as well as active crustal faults for the Ust-Kamchatsk village, Kamchatka through trenching and geomorphic investigations. According to the data obtained for the last few thousand years, strong tsunami wave height exceeded 6.8

m and a horizontal splash of several km has occurred in the area on average once every 300 years (Pinegina et al. 2012). From this investigation, Pinegina et al. 2012 showed that there was repeated movement on one crustal fault on average every 2.5 thousand years, due to the magnitude of the ground quakes, which were estimated to be $M \sim 6.5-7.5$.

1.5 THE STUDY AREA: KUMROCH FAULT

Kozhurin et al. (2006) determined that the KF was a normal fault with a dip angle of $65-70^\circ$ to the west, and in their 1990 study observed that the KF was active; determined through offset moraines of the last glaciation, post-glacial terraces, and debris fans. They established that the maximum postglacial vertical offset of the Pleistocene moraine surfaces is 27-30 m, and that the rate of vertical movement is approximately 2.0-2.5 mm/yr. This was done by using the vertical offset of the moraine surfaces and Kozhurin's (1990) estimated ages of the moraine surfaces, which were between 11500 and 14000 calibrated ^{14}C years BP. They also observed that there was evidence for a component of right-lateral movement of the fault, comparable to that of the normal component (Kozhurin et al, 2006).

Furthermore, Kozhurin et al. (2006) describe how, at the southern end of the East Kumroch Range, the KF bends to a NE-SW strike and branches into three splay faults. Two of these faults are relatively short, while the third (southeastern) fault extends further south (Figure 3 and 4). This third fault crosses the Bol'shaya Khapitsa valley (Figure 3 and 4), producing a prominent escarpment, though significantly smaller than that of the KF (about 200 m and 1000 m high, respectively; Kozhurin et al., 2006). South of the East Kumroch Range this fault forms the principal boundary between the CKD and East Kamchatka Range. Several observations were made by Kozhurin et al. (2006) in and north of the Bol'shaya Khapitsa valley, which suggest that the fault, in the same way as the KF, combines roughly equal right lateral and vertical movements.

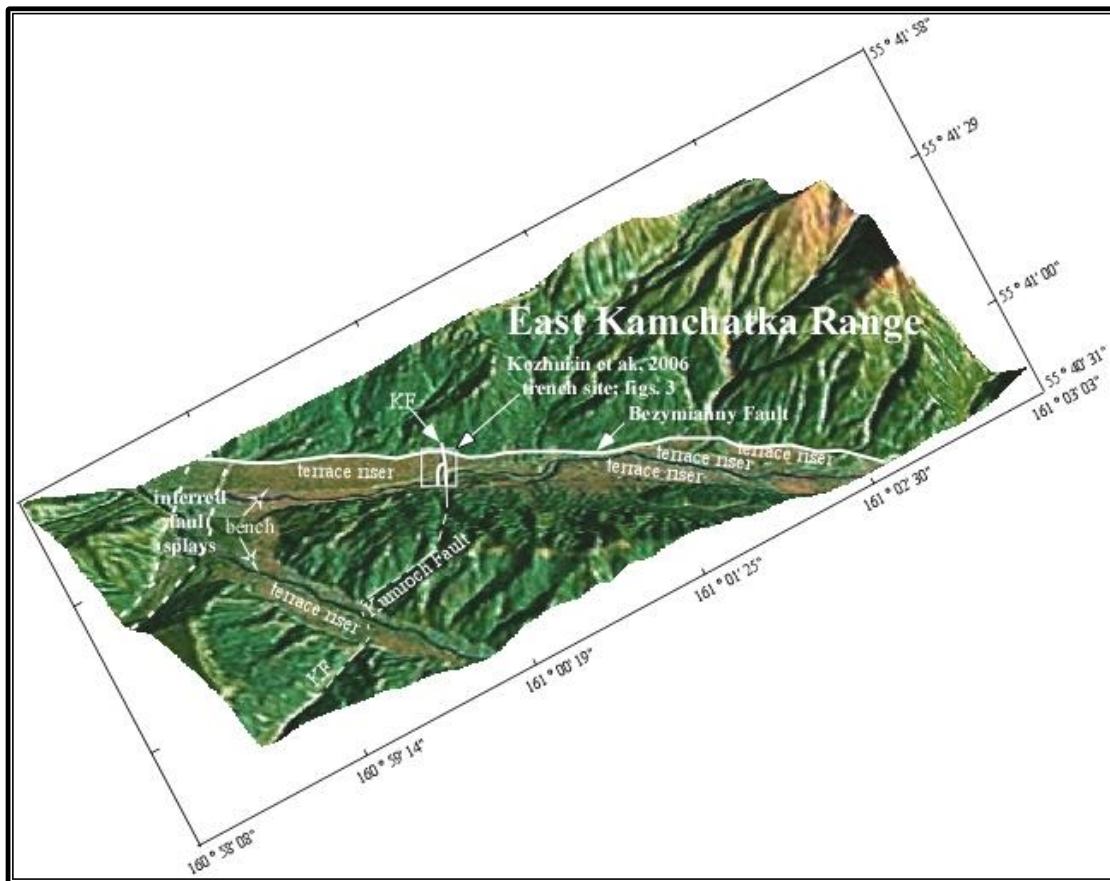


Figure 1.4: Kozhurin et al. 2006 trench sites and surrounding area (see Figure 3 for location). The traces of the KF and BF are indicated by white solid lines dashed where inferred. White dashed lines located in the northwest corner of the map are inferred faults splays. Benches are indicated by white arrowheads with hole in center. Image is a Satellite photo reproduced and modified from Google Earth Pro 2004 draped over Landsat ETM+ band 8 and has been modified with computer applications for geomorphic mapping.

Kozhurin et al. (2006) explain that within the river valley, faulting produces northwest-facing scarps across a series of terraces (Figure 4). Their observations show that on the highest river terrace, which they labeled (t5), a single scarp is produced with 3.3 m of ground surface vertical separation (Kozhurin et al. 2006; Fig. 8). They describe how, on the succeeding terrace (t4), the scarp bifurcates into two lower scarps, and determine a total amount of vertical separation (across two faults) remaining roughly the same at 3.2 m (Kozhurin et al. 2006; Fig. 8). Their observations show that the three scarp profiles differ from east to west, evident in the slope angle of the terrace surface between scarps. They could only place limits on the amounts of vertical separation across each scarp separately

(0.9 m – 1.35 m and 1.25 m and 1.6 m; Caskey, 1995). Kozhurin et al. (2006; Fig.8) illustrate that on the youngest of the faulted terraces (t2), there is again a single scarp with only 0.8-0.9 m of vertical separation. They explain that the observed decrease in amplitude of vertical ground surface offsets from t5 to t2 indicates that the larger surface offset measured is a cumulative vertical displacement (Kozhurin et al. 2006; Fig. 8). They suggest that it is also likely that the 0.8-0.9 m vertical offset is a one-event offset and that the terrace t2 has been ruptured only once. They argue, however, that based on the above values, it cannot be said with certainty by what increments the higher fault scarps have been growing (Kozhurin et al. 2006; Fig. 8).

Three trenches were dug across the fault scarps and 22 exploratory pits and natural outcrop excavations were conducted within the terrace sequence adjacent to the trenches. More widely, the study in the valley that Kozhurin et al. (2006) conducted shows that the terraces were mantled with a clearly defined succession of pyroclastic deposits with intervening soil development. Individual faults of the East Kamchatka zone reveal combined normal right-lateral strike slip fault movements (Kozhurin, 1990). Amplitudes of observed late Quaternary normal displacement do not exceed 30 m (by late Pleistocene moraines) and those of right-lateral offset reach 70 m - 80 m (Kozhurin, 1990).

In 2007, Kozhurin collected geomorphic and trenching data that suggested that the west-dipping planes of the faults of the East Kamchatka Fault Zone are likely to flatten with depth, namely, having listric morphology. The 2007 study also defined the faults in the trench location as being extensional, confined to the volcanic zones of the eastern, southern and northern regions of Kamchatka, and manifested by either surface scarps or fissures beneath linear rows of monogenic cones (Kozhurin 2007). In the Kozhurin (2007) study one trench (named the “Berezhnyachishkovaya-1”) was dug perpendicular to the KF (see Figure 3 for location: 161.12575°E, 55.83677°N). The scarp height was 3 m and Kozhurin determined that the scarp formed in the interval of 3.3 ka -3.5 ka, ~2.3 ka -2.5 ka. These results confer a vertical slip-rate of 1.2 mm/yr to 1.3 mm/yr.

1.6.1 Methods: morphologic dating

Determining fault-scarp chronologies is important in the assessment of active tectonics, earthquake hazards and in paleoseismology (Ayarbe et al., 1998; Bruhn et al., 2004; Plafker and Thatcher, 2008). There have been multiple investigations using fault scarp diffusion models in arid environments (Wasatch fault of Utah and the East Potrillo fault of southeastern NM). These settings contain a low abundance of organic carbon, which often prevents Carbon-14 dating of displacements; therefore, in arid regions fault scarp diffusion modeling and morphologic dating are applied to date scarps (Black et al., 2003; Chang 1998; Chang and Smith 2002; Cluff et al., 1973; DuRoss & Bruhn, 2004; Friedrich et al., 2003; Hanson et al., 1981; Harty et al., 1997; Jackson, 1991; Cervera, 2006). The use of the Constant Slip Rate (CSR) method in this instance is the first of its kind to be done in this region and relatively new in this type of environment.

Fortunately, the Kamchatka Peninsula is a region of wet humid conditions. The KF has been trenched, and trench profiles have been reconstructed. These profiles record good quality chronologies, which are used here in comparison with this study's geomorphologic techniques.

Fault ruptures are the surface expression of the displacement or mechanical failure of rock along a fault plane at depth. Spatial patterns of surface faulting reflect the geometry of slip on the fault plane, and temporal patterns indicate the rate at which stress accumulates to some critical level inducing rupture, or the behavior of the seismogenic cycle (DuRoss & Bruhn, 2004). Collectively, the spatial and temporal rupture trends have important implications for the fault system, segmentation of fault systems, and recurrence intervals of paleoearthquakes.

Fault trenches excavated normal to the scarp reveal the number, timing, and size of surface-faulting earthquakes at the sites, but have a limited spatial and temporal window (DuRoss & Bruhn, 2004). Alternatively, fault trenches along strike supply observations of fault surface ruptures (e.g., Nelson and Personius, 1993) and provide insight into the behavior and distribution of slip along the entire length of the fault, but are restricted in their ability to identify individual surface-faulting

earthquakes (DuRoss and Bruhn, 2004). Thus, to identify and understand the spatial and temporal components, meter-to-kilometer-scale ruptures and scarp analyses must be used in concert with centimeter-to-meter-scale fault-trench studies (DuRoss and Bruhn, 2004).

Profile modeling of scarps formed by several events distributed through time is done using a Constant Slip Rate (CSR) solution and yields a value of A/κ [$1/2$ slip-rate/diffusivity] (Mattson & Bruhn, 2001). The CSR method is used when the rupture history is not known or when the history exceeds that determined by trenching (Mattson & Bruhn, 2001).

Erosion and deposition play an important but widely unrecognized part in fault scarp evolution, as can be seen in many trenching studies. Wallace (1977) noted that the geomorphic characteristics of degraded scarps of comparable heights with steeper free faces are younger, whereas scarps which are less steep are older. A drawback to the fault-scarp diffusion technique is that the geomorphic diffusivity is often unknown and must be estimated. Because the diffusivity of unconsolidated material can vary by three orders of magnitude, a large amount of uncertainty is introduced into the calculated age of a scarp (Hanks, 2000; Ayarbe et al., 1998). It is worth noting here that Mattson and Bruhn (2004) concluded that scarps with topographic relief greater than about 20 m or so appeared to degrade by processes other than diffusion, perhaps by land sliding or slumping of scarp faces prior to degradation.

To determine diffusion constants (κ) in the study area, the relative timing of fault displacements (Wallace, 1977; DuRoss & Bruhn, 2004), and the timing of the most recent surface-faulting event (Bucknam & Anderson, 1979; Nash, 1980; Avouac, 1993; Arrowsmith et al., 1998; DuRoss & Bruhn, 2004) fault-scarp morphology methods were used on Kozhurin et al. (2006) ground data from their trench profiles. One method used in morphological analyses of fault scarps is the diffusion equation to model the erosion of fault scarps over time, estimating the time of faulting for a single-event scarp (Hanks, 2000; DuRoss & Bruhn, 2004) or the time of initial scarp formation for composite scarps (Mattson & Bruhn, 2001; DuRoss & Bruhn, 2004). Diffusion-equation modeling of scarps is an

efficient reconnaissance method, based on the premise that the rate of change in elevation of points on the scarp face is a function of the slope curvature and scarp κ , which is a function of climate and material properties (Culling, 1963; Nash, 1980; Hanks et al., 1984). Hanks et al. (1984) found the product of scarp diffusivity and time to be dependent on scarp height or vertical displacement, which implies nonlinear transport processes (DuRoss and Bruhn, 2004).

In this method, a nonlinear diffusion model was used (Equation 2, Andrews & Bucknam, 1987) to minimize the effect of vertical displacement on diffusivity (DuRoss and Bruhn, 2004). The model includes a nonlinear frictional sliding transport law, in which particles move as a function of weight, energy and velocity, the coefficient of friction, and the slope angle (DuRoss and Bruhn, 2004). The nonlinear transport model reduces to a linear transport model at small slope angles (DuRoss and Bruhn, 2004). The CSR model approximates a multiple-event or composite scarp by incrementally displacing and eroding an initially planar geomorphic surface at a constant rate through time (Mattson & Bruhn, 2001). The CSR model is preferred in the study, and it is best applied to scarps younger than ~10 ka with an unknown rupture history.

In using the diffusion equation to model the erosion of scarps on unconsolidated material, a number of assumptions are made. These assumptions were discussed in the Diffusion Modeling Technique section of DuRoss' and Bruhn's (2004) article. Such assumptions are acceptable, as a large scarp profile dataset accounts for variability in scarp erosion and vertical displacement. Scarp mapping has revealed the surface rupture locations. However, caution must be taken in interpreting the results, as a potentially variable diffusivity constant (e.g., during the Pleistocene) and the possibility of unrecognized or completely eroded fault scarps may lead to erroneous results.

The CSR, nonlinear diffusion model compares a suite of synthetically generated profiles with the observed, natural scarp profile. The upper half of the natural profile was modeled (DuRoss and Bruhn 2004 Fig. 6), as the lower half is commonly subject to nondiffusive processes such as fan deposition,

gullying, surface tilt, and graben formation. The shape of each synthetic profile corresponds to a discrete time since initiation of faulting on a geomorphic surface (DuRoss and Bruhn 2004; Fig. 6). The best-fit synthetic profile is defined as the one with minimal misfit between it and the natural profile. In this case, misfit is defined as the standard deviation between the elevation points along natural and synthetic profiles. The time at which surface displacement began on the best-fit synthetic profile is the modeled initiation of scarp formation, or the scarp initiation time.

Following each simulation, the vertical displacement, best-fit scarp initiation time and slip-rate (vertical displacement divided by scarp initiation time) were logged (DuRoss and Bruhn 2004; Fig. 7). A typical solution involved 10,000 simulations for a single scarp profile, generating a mean scarp initiation time and mean slip-rate ($\pm 1 \sigma$). For a positively skewed distribution of scarp initiation times, a trimmed mean was used in place of the mean. The trimmed mean is the mean of the data set with the outliers (upper and lower 5% of the data values) eliminated, effectively reducing the positive shift of the mean due to high-valued outliers.

1.6.2 Methods: The datasets

The natural topography of the location used in this study contains hills, glacier moraines, and fault traces. The study area is an ideal location to understand the relative importance and interactions of data from different remote sensors, all with meter level spatial resolution. For this study, ASTER GDEM Version 2, Landsat ETM+ image and Google Earth Pro imagery were collected and utilized (Figure 5).

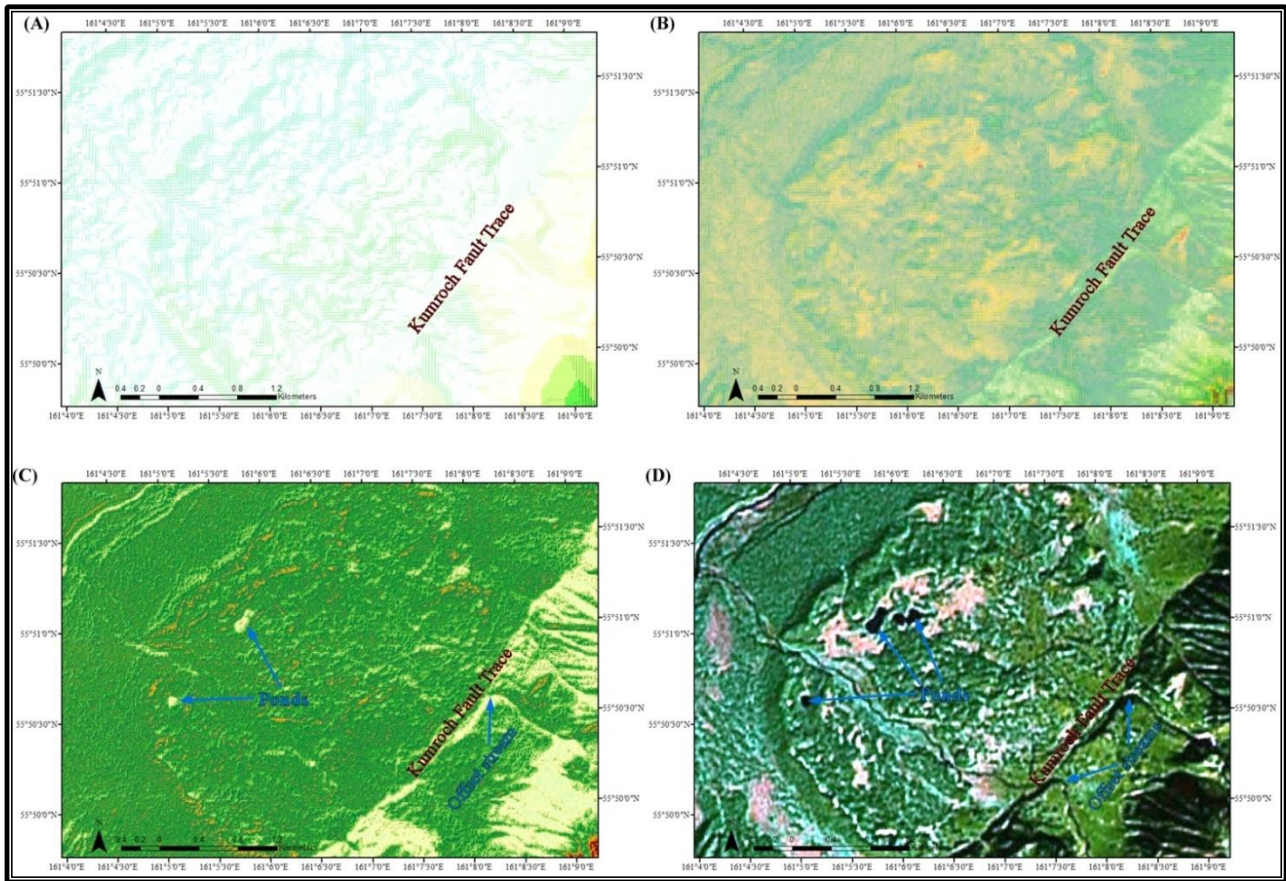


Figure 1.5: 1:5000 scale images illustrating the various data sets pixel resolutions. (A) ASTER GDEM Version 2 image in false color from the USGS Earth Resources Observation and Science (EROS) Center webpage. DEM has vertical (root-mean-squared-error) accuracies generally between 17 m at the 95 % confidence level, and a horizontal resolution on the order of 75 m. The ASTER GDEM large scene revealed large active tectonic features such as the Kumroch Fault (KF) trace. (B) Landsat ETM+ image bands 1 to 5 and 7 data in false color from the Alaska Satellite Faculty (ASF) with a spatial resolution of 30 meters. (C) Landsat ETM+ image band 8 in false color with the resolution of 15 m. The Landsat band 8 revealed large active tectonic features KF trace and geomorphic features such as ponds. The approximate scene size for each scene is 170 km north-south by 183 km east-west. (D) Georeferenced Google Earth Pro image, spatial resolution of the Google Earth images is 5 m. The approximate scene size is 10 km north-south by 8 km east-west. Small scale surface features were visible with the Google Earth imagery, such as offset streams.

The ASTER GDEM Version 2 data were collected from the USGS Earth Resources Observation and Science (EROS) Center webpage (Figure 5A). Four single-scenes with the same gridding and tile structure as GDEM 1.0 (60– x 60- km) were used for this study. The DEMs have vertical (root-mean-squared-error) accuracies generally between 17 m at the 95 % confidence level, and a horizontal resolution on the order of 75 m. The ASTER GDEM data were posted on a 1 arc-second (approximately

30 m at the equator) grid. [*For more detailed information of ASTER GDEM Version 2 data set see; (http://eros.usgs.gov/#/Find_Data/Products_and_Data_Available/Aster).*] The four single scene ASTER GDEM Version 2 data sets were “mosaicked” into one large scene with horizontal resolution of 30 m and vertical resolution of 17 m. The large scene was displayed and inspected for quality, clarity and details captured by the image. The ASTER GDEM large scene revealed large active tectonic features such as the Bezymianny, Gora Oval’naya Zimna, and Gora Bolshay Udina volcanos and the KF trace.

The Landsat ETM+ image data were collected from the Alaska Satellite Facility (ASF). Landsat ETM+ image data consist of eight spectral bands, with a spatial resolution of 30 m of bands 1 to 5 and band 7. The resolution for band 6h/6L (thermal infrared) is 60 m or 30 m (Figure 5B). The resolution for band 8 (panchromatic) is 15 m (Figure 5 C). The approximate scene size of the Landsat ETM+ data is 170 km north-south by 183 km east-west. [*For detailed information on the Landsat satellite, the ETM+ sensors, and Landsat data products, visit the Landsat Science Data Users Handbook (http://tpwww.gsfc.nasa.gov/IAS/handbook/handbook_toc.html).*] For this study, bands 1 to 5 and 7 were chosen because their pixel resolution is similar to ASTER GDEM and were compared. Band 8 was selected because of its high resolution and details captured by the image reveal greater detail of the active tectonic surface features, for example volcanoes, facet spares, terrace risers and the trace of the KF, and BF.

Images were collected from Google Earth Pro (Figure 5D). The Google Earth images were georeferenced in ArcGIS10 using the Landsat band 8 data. This procedure allowed for the detailed exploration of the study area, and specific sites were selected to construct geomorphic mapping and topographic profiles, primarily to examine surface ruptures that are observed throughout the Google Earth imagery. The spatial resolution of the Google Earth images is 5 m. The approximate scene size is

10 km north-south by 8 km east-west. Small scale surface features were visible such as offset streams and fault scarps.

Interpretations and identification of the origin of fault scarps and normal and reverse faulting were possible using field evidence from Kozhurin et al. 2006, Kozhurin 2007, and computer application techniques used on the various data sets by means of GIS and reconstruction software, as well as Esri's ArcGIS 10 and Midland Valley's Move 2012. By draping Google Earth images over the ASTER GDEM and Landsat band 8 data, realistic 3D models were created. Computer application techniques and the use of red blue 3D glasses and ChromaDepth 3D glasses were used on the normal 2D and 3D images (Figures 2, 3, and 4). This allowed observation, mapping and collection of topographic profiles, which assisted greatly in resolving geomorphic features. This technique confirmed the fault trace of the KF that was observed in the ASTER GDEM and Landsat band 1 to 5 and 7.

The resolution (pixel size) of each data set affected each of the images and the posting of elevations (vertical) and distances (horizontal), which also affected the ability to resolve features of various sizes. For example, small geomorphic feature like offset streams and fault scarps were not visible in the ASTER GDEM or the Landsat bands 1 to 5 and 7 data (Figure 5A and 5B). However, these same small-scale geomorphic surface features were visible in the Landsat band 8 and Google Earth imagery (Figure 5C and 5D). Fault scarp profiles were determined using the 3D analyst extension tool in ArcGIS10. All topographic profiles were drawn from east to west for consistency. Horizontal and vertical errors are estimated to be ~15 m and 17 m, respectively based on the Landsat band 8 dataset. Scarp profile curves were initially compared with two dimension dislocation fault models to determine fault type of the scarps and assist in resolving the origin of the surface ruptures, but this did not provide any insight and this method was eventually abandoned.

1.7.1 RESULTS: MORPHOLOGIC DATING

The Kozhurin et al. 2006 (tephra and stratigraphy) calibrated ages are used in the CSR analysis to estimate κ and estimate slip-rates at both the 2006 trench sites (profiles AK2006A, AK2006B, AK2006C) and the Kozhurin 2007 trench site (profile Berezhnyachishkovaya-1). The results from this analysis are shown in Figures 6, 7, 8 and 9 and Table 1. These same calibrated ages and diffusion method were then used to evaluate other ground collected data (trench sites) within the Kamchatka Peninsula region, Kozhurin et al. 2008 (profile Poperechnaya), and Pinegina et al. 2012 (profile Izvilistaya) (Table 1 and Figures 8 and 9). This paper's results (CSR method) are then compared to these previous studies results for consistency.

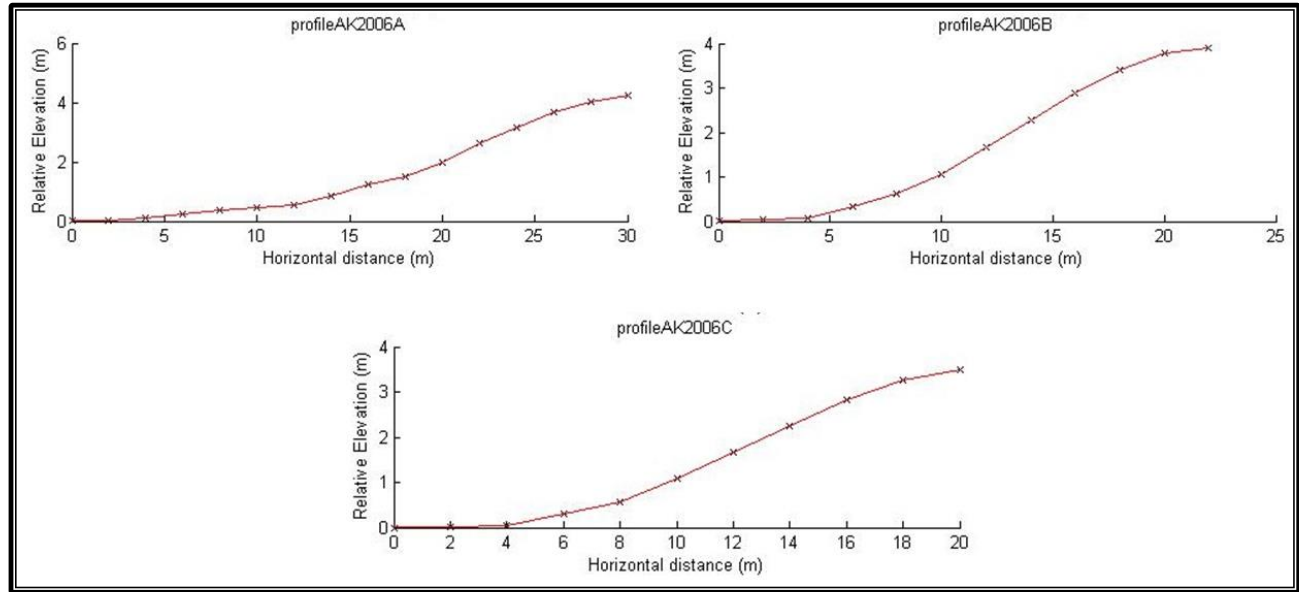


Figure 1.6: Fault scarp profiles of the scarp diffusion modeling, based on determination of the vertical displacement between upper and lower far-field slopes. The rupture history is known from paleoseismic trench data Kozhurin et al., 2006, see figure 1.3 for location within study area.

Kozhurin et al.'s (2006) ground data were used to reconstruct fault scarp profiles (Figure 6) to determine two data sets of estimated κ , timing of the MRE along the KF, estimated slip-rates, and displacements (Figure 7; Table 1). One set of slip-rates and κ along the KF were estimated based on Kozhurin et al. (2006) fault event ages (tephra chronology), which range from 3.2 ka to 3.3 ka, that produced 0.6 mm/yr to 1.0 mm/yr slip-rates, and 8 m²/ka to 14 m²/ka κ [Table 1- profiles AK2006A

(tephra), AK2006B (tephra), and AK2006 (tephra)]. Displacements were estimated to range from 2.5 m to 3.2 m (Table 1). Other sets of estimated κ and estimated ages of the MRE were based on Pleistocene moraine surfaces with slip-rates of 2.0 mm/yr to 2.6 mm/yr. The κ range from 20 m²/ka - 30 m²/ka and the MRE ages range from 1.4 ka to 1.6 ka [Table 1 - profiles AK2006A (moraine), AK2006B (moraine), and AK2006 (moraine)]. Displacements were estimated, and range from 2.4 m to 3.2 m (Table 1).

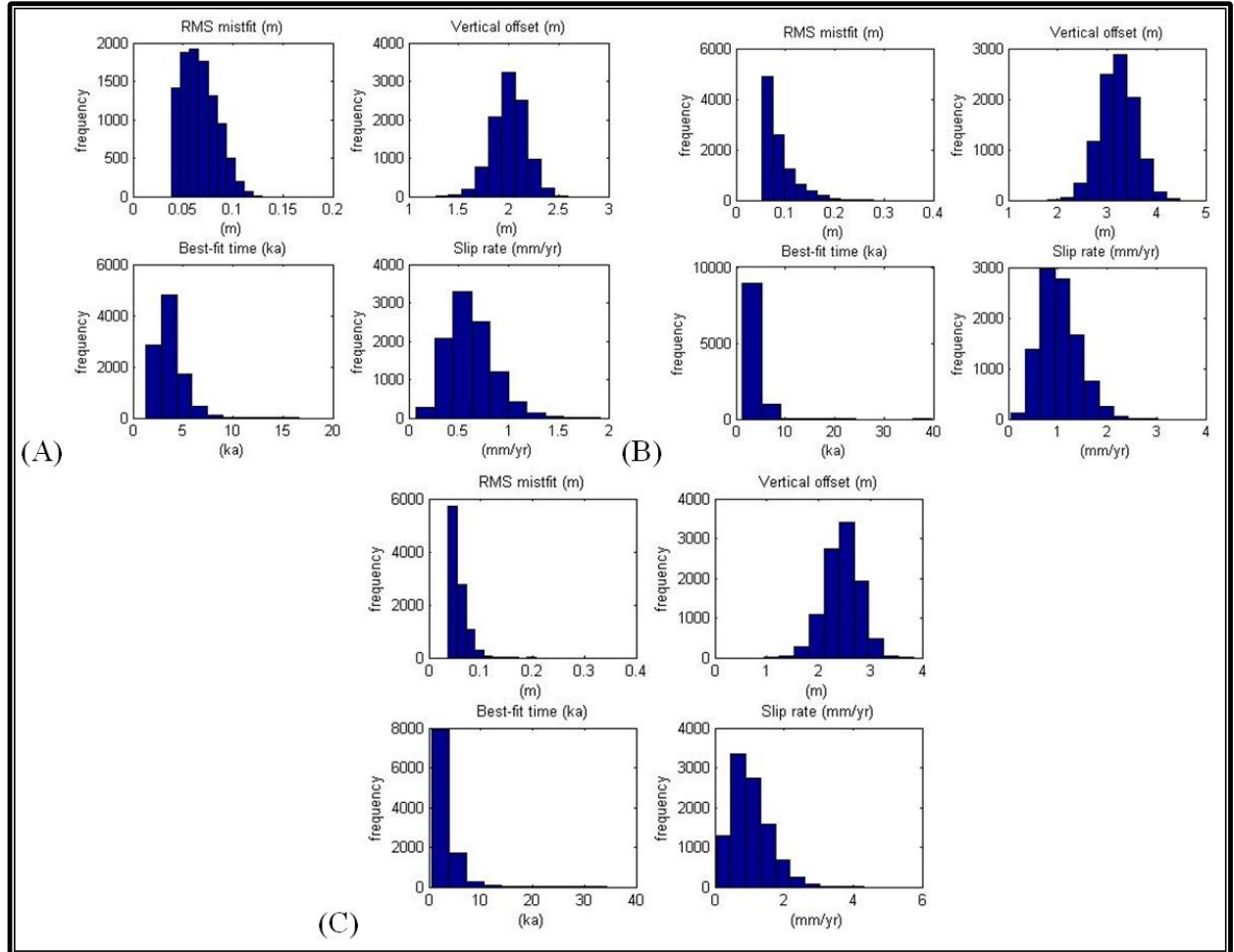
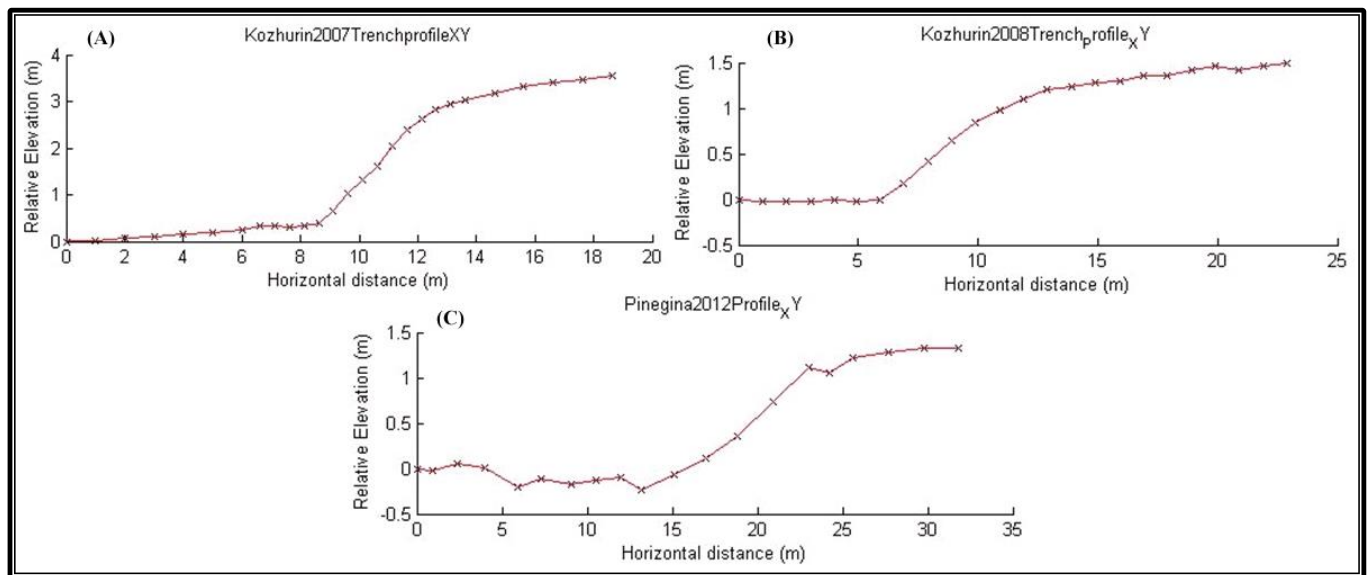


Figure 1.7: Diffusion modeling results from 10,000 simulations on the three trench profiles (AK2006A, AK2006B, and AK2006C) of Kozhurin et al. 2006. Graph sets show results from diffusion modeling from mean of diffusion model RMS misfit values (standard deviation between synthetic and natural profile points), Vertical displacement between upper and lower far-field slopes, Best-fit time scarp initiation time (upper and lower 5% of data discarded), and Vertical slip-rate. Values are mean $\pm \sigma$.

Table 1.1: Results from fault scarp diffusion models of Mattson and Bruhn (2001) and DuRoss and Bruhn (2004) and Kozhurin et al. (2006), Kozhurin (2007), Kozhurin et al. (2008) and Pinegina et al. 2012 trench profiles of the KF as calibrated age fault scarp diffusion rates were estimated. (-) mean that no data could be determined.

Profile	Diffusion constant κ (m ² /ka)	Vertical offset (m)	Trimmed best-fit (ka)	Best-fit lowest RMS (ka)	Vertical slip rates (mm/yr)
AK2006A (tephra)	11	2.0 +/- 0.1	3.6 +/- 0.9	3.7 +/- 1.3	0.6 +/- 0.2
AK2006A (moraine)	20	2.4 +/- 0.3	1.3 +/- 0.4	1.4 +/- 0.6	2.0 +/- 0.9
AK2006B (tephra)	8	3.2 +/- 0.2	3.4 +/- 0.9	3.5 +/- 1.4	1.0 +/- 0.4
AK2006B (moraine)	20	3.2 +/- 0.2	1.4 +/- 0.4	1.4 +/- 0.5	2.6 +/- 0.9
AK2006C (tephra)	14	2.5 +/- 0.1	3.1 +/- 1.2	3.4 +/- 2.1	1.0 +/- 0.5
AK2006C (moraine)	30	2.5 +/- 0.2	1.4 +/- 0.9	1.6 +/- 1.4	2.1 +/- 1.1
Bereznayachishkovaya-1 Kozhurin et al. 2007	11	2.1 +/- 0.1	-	0.2 +/- 0.0	10.5 +/- 1.0
Poperechnaya Kozhurin et al. 2008	30	1.1 +/- 0.1	0.3 +/- 0.1	4.8 +/- 1.3	4.7 +/- 0.8
Izvilistaya Pinegina et al. 2012	30 to 70	1.3 +/- 0.1	0.8 +/- 0.1 to 0.3 +/- 0.1	0.8 +/- 0.1 to 0.3 +/- 0.2	1.8 +/- 0.5 to 4.0 +/- 1.1

Figure 8A shows Kozhurin's (2007) fault scarp profiles from his trench site "Bereznayachishkovaya-1", which was processed using the CSR method (Figure 9A). The estimated κ for this trench site is 11 m²/ka (Table 1). The MRE age estimate is 0.2 ka, and a displacement of 2.1 m was determined (Table 1). Slip-rates were also estimated at 10.5 mm/yr (Table 1).



1.8: Fault scarp profiles of the scarp diffusion modeling, based on determination of the vertical displacement between upper and lower far-field slopes. The rupture history is known from paleoseismic trench data (A) Kozhurin 2007, see figure 1.3 for location within study area, (B) Kozhurin et al., 2008, and (C) Pinegina et al. 2012.

Kozhurin et al. (2008) conducted fieldwork resulting in a trench site named “Poperechnaya”.

This trench site is located about 337 km southwest of the study area and northwest of the city of Petropavlovsk-Kamchatka (location: 157.67488°E, 53.38805°N). In their investigation Kozhurin et al. 2008 estimated vertical offset of 1 to 1.2 m, estimated ages from ^{14}C samples of 8900 \pm 50 years or \sim 10 ka in calendar years. Kozhurin et al. 2008 suggested that the MRE fault movement in this region took place between 10 ka and 8.4 ka based on C^{14} and tephra chronologies. The Kozhurin et al. 2008 trench fault scarp profile was analyzed using the CSR method (Figure 8B and Figure 9B). The estimated κ determined for this trench site is $30 \text{ m}^2/\text{ka}$ (Figure 9B and Table 1). The MRE age was estimated at 0.2 ka. A displacement for this location is 1.1 m (Figure 9B and Table 1). Slip-rates were estimated at 4.7 mm/yr (Figure 9B and Table 1).

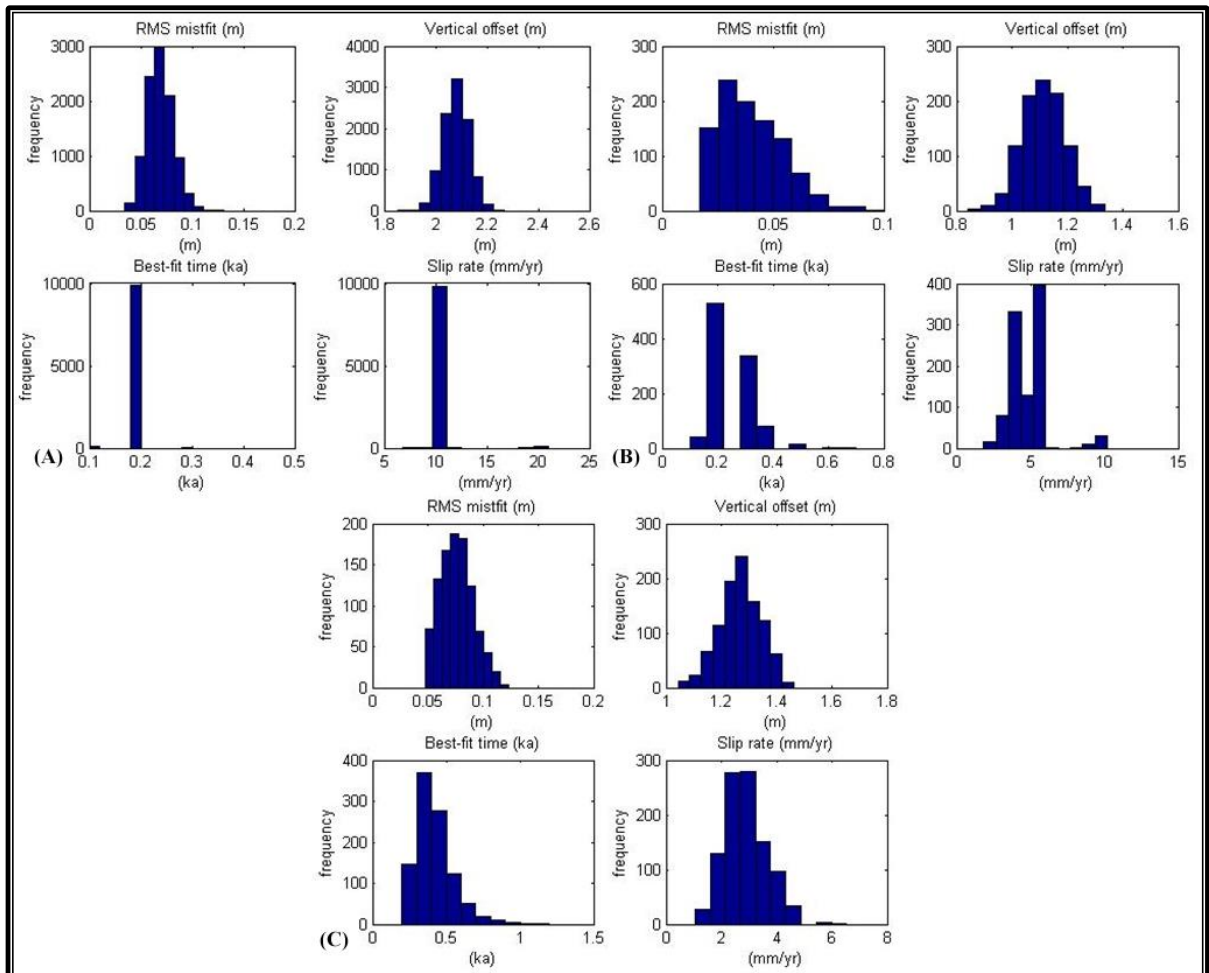


Figure 1.9 Diffusion modeling results from 10,000 simulations of the three trench profiles (A) Bereznyachishkovaya-1, (B) Poperechnaya, and (C) Izvilistaya from the Kozhurin 2007, Kozhurin et al.

2008 and Pinegina et al. 2012 articles, respectively. Graph sets show results from diffusion modeling from mean of diffusion model RMS misfit values (standard deviation between synthetic and natural profile points), Vertical displacement between upper and lower farfield slopes, Best-fit time scarp initiation time (upper and lower 5% of data discarded), and Vertical slip-rate. Values are mean $\pm \sigma$.

Pinegina et al. 2012 conducted seismic and tsunami hazard evaluations that include a trench site (named “Izvilistaya”). It is about 106 km northeast of the study area near the village of Ust-Kamchatka (location 162.311714°E, 56.318725°N). In this investigation they estimated that the MRE took place between 800 and 300 years BP and formed a scarp of 0.4 m high. The Pinegina et al. 2012 trench fault scarp profile was analyzed using the CSR (Figure 8C and Figure 9C). Based on Pinegina et al. (2012), trenched profile estimated κ for this trench site range between 30 m²/ka to 70 m²/ka (Figure 9C and Table 1). The MRE ages were estimated between 0.8 ka to 0.3 ka. A displacement for this location is 1.3 m (Figure 1.9C and Table 1). Slip-rates were also estimated between 1.8 mm/yr to 4.0 mm/yr (Figure 9C and Table 1).

1.7.2 Results: Observations from the datasets

3D virtual mapping of the study area defined the extent and geometries of fault traces and geomorphic surface features along the western edge of the KF and BF. Normal active dip-slip motion was observed along with sinistral strike-slip fault motion, fault splays, reverse faults, right and left bends, right and left step-overs, and segment boundaries of faults, which were mapped and surveyed along both the length of the KF and BF (Figures 3, 4, 5 and 10). Figure 3 aided in choosing specific field sites, and put results in a local and regional context. Geomorphic surface features such as fault scarps, fault scarp segment boundaries, faceted spurs, benches, terrace risers, beheaded stream channels, and sinistral offset stream channels were mapped, and aided in the interpretation (Figures 4 and 10). Figure 10 is an example of the geomorphic mapping of these specific sites. The site locations were chosen to compare with Kozhurin et al. (2006) and Kozhurin (2007) trench sites (Figure 3, 4 and 10).

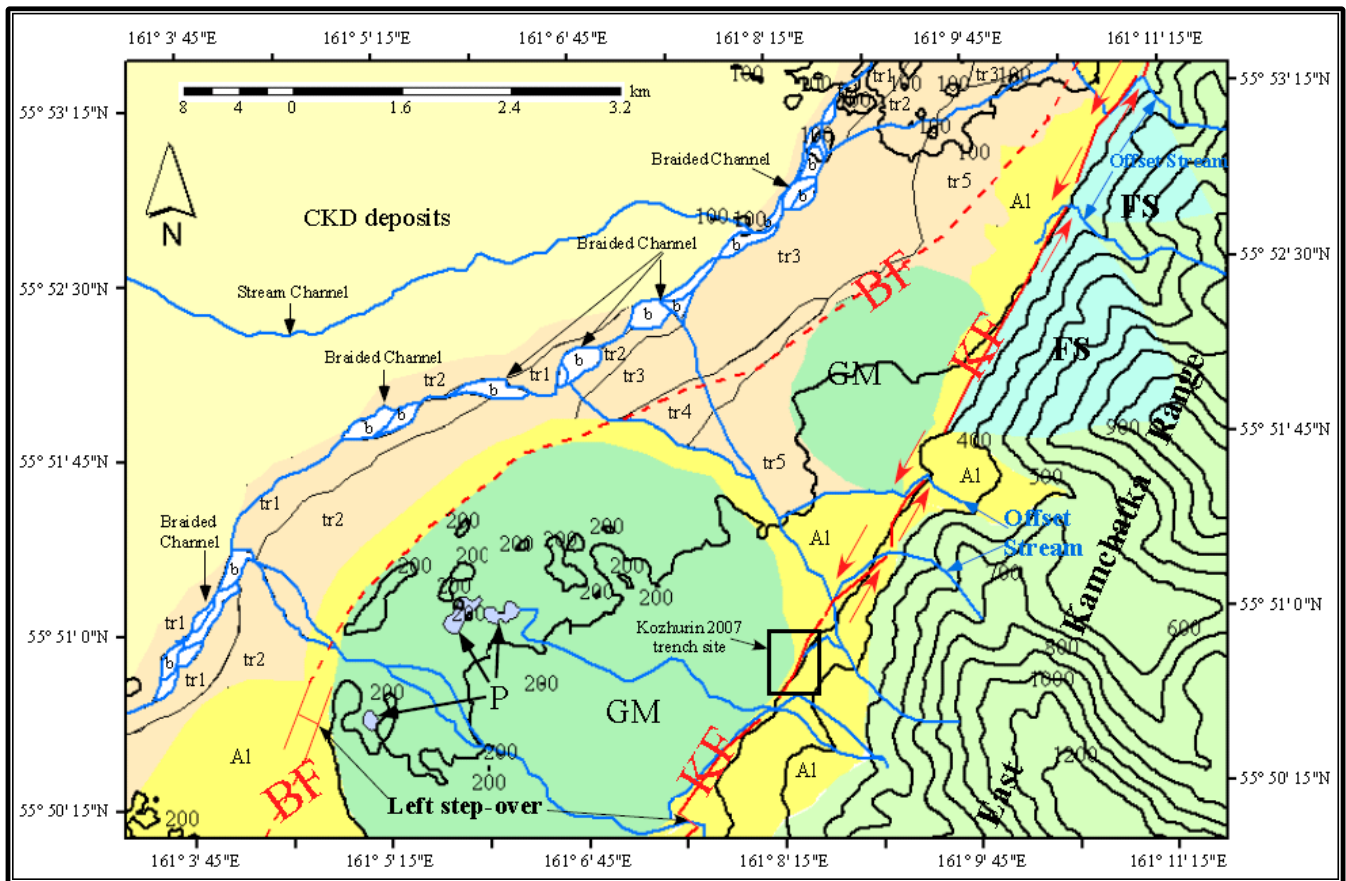


Figure 1.10: Geomorphic map of one of the focus sites made with the Landsat ETM+ band 8 data sets with Google Earth images draped over terrain model (5 m - 15 m accuracy). Contour intervals are 100 m designated by black lines. East Kamchatka Range is sage color located in southeast corner of map. The Kumroch Fault (KF) trace = red lines, red arrows indicate left-lateral motion and the Bezymianny Fault (BF) trace = red dashed lines. Stream channels = blue lines, offset stream channels = blue lines with blue arrows, braided channels = blue lines with white polygons, bars (b) = white polygons, and ponds (P) = blue polygons. Central Kamchatka Depression (CKD) deposits = tan polygon, terrace risers (tr1-tr5) = beige polygons, alluvial fans (A1) = yellow polygons, glacier moraines (GM) = green polygons, facet spars (FS) = teal color triangle shaped polygons.

Neither the KF nor BF traces are simple linear features at the surface. Both have a geometry that is irregular and segmented (Figure 3). These irregularities of geometry and segmentation are identified by segment boundaries, left step-overs, and left bends (Figures 3, 4, and 10). This left bend is also observed in the virtual mapping, and agrees with Kozhurin et al. 2006 observations as to where the KF bends NE-SW and branches into three splay faults, where one splay crosses the Bol'shaya Khapitsa valley and forms the principal boundary between the CKD and East Kamchatka Ranges. In 2006, Kozhurin et al. reported that the KF had evidence of a component of approximately 15 m of right-lateral

movement comparable to the normal component of a river terrace formed at a large Late Pleistocene fan, Central Kumroch Range, Topolovaya River (Kozhurin et al. 2006; Fig. 5B). They observed in the north of the Bol'shaya Khapitsa valley that this fault splay occurred in the same way as the KF, combining roughly equal right-lateral and vertical movements (Kozhurin et al. 2006; Fig. 6). Conformity of these right-lateral motions is difficult to confirm from the Kozhurin article due to the position of the photographs taken by Kozhurin et al. 2006 and such conformity was not observed in the virtual mapping. Any horizontal movement occurring on the fault zones has been debated at length by Erlich (1973), Erlich et al. (1974), and Legler (1976). The Erlich (1973) interpretation of left-lateral motion was based on the echelon plane-view arrangement of Z-shaped individual ranges within the elevation of the East Kamchatka Ranges and the presence of approximately N-S striking grabens between the ranges. This was inferred as a component of along-strike extension, although no strike-slip offsets of geomorphic features were observed along individual faults of the system (Erlich et al. 1974). It had been concluded that movements along the fault zone were dominantly left-lateral, based on the assumption that the fault zone was the western boundary of a block that had been moving northeast throughout the Quaternary due to the oblique Pacific plate/arc (Legler, 1976). Legler's (1976) model also predicted that this left-lateral back-arc strike-slip faulting would only affect the northern half of the Kamchatka-Kurile arc, and that in the southern Kurile the sense of strike slip faulting must change to right-lateral.

Observations in this study show that the KF trace is relatively linear in the northern 2/3 of the mapped area (Figure 3 and 10) and trends parallel with a glacial trough, but shows a large left-stepping bend to the south where the trace then picks up again through a complex series of splays in the south of the mapped area (Figure 3 and 4). The geomorphic mapping observations indicate that the trace of the KF contains evidence of left-lateral motion, based on four sinistral offset stream channels and a left step-over along the KF trace (Figure 10). The offset stream channels observed were then evaluated by

measuring their length, which ranged from 100 m (+/- 15m) to 400 m (+/- 15m). These stream channels may have been attributed to postglacial movement of roughly 10 ka. Using the offset stream channels measuring length divided by the roughly 10 ka postglacial age, this would yields lateral slip-rates of 10 mm/a - 40 mm/a. Topographic profile A - A' illustrates the characteristics of the faults observed in the mapped area (Figure 11). Section A - A' was drawn across strike from the main trace of the KF, across the BF, and into the faults array to the west, where they abut a volcanic landscape (Figures 3, 10, and 11). This section illustrates the basic graben structure between the master KF and reverse faults related to the KF that separate the valley from the volcanic uplands to the west.

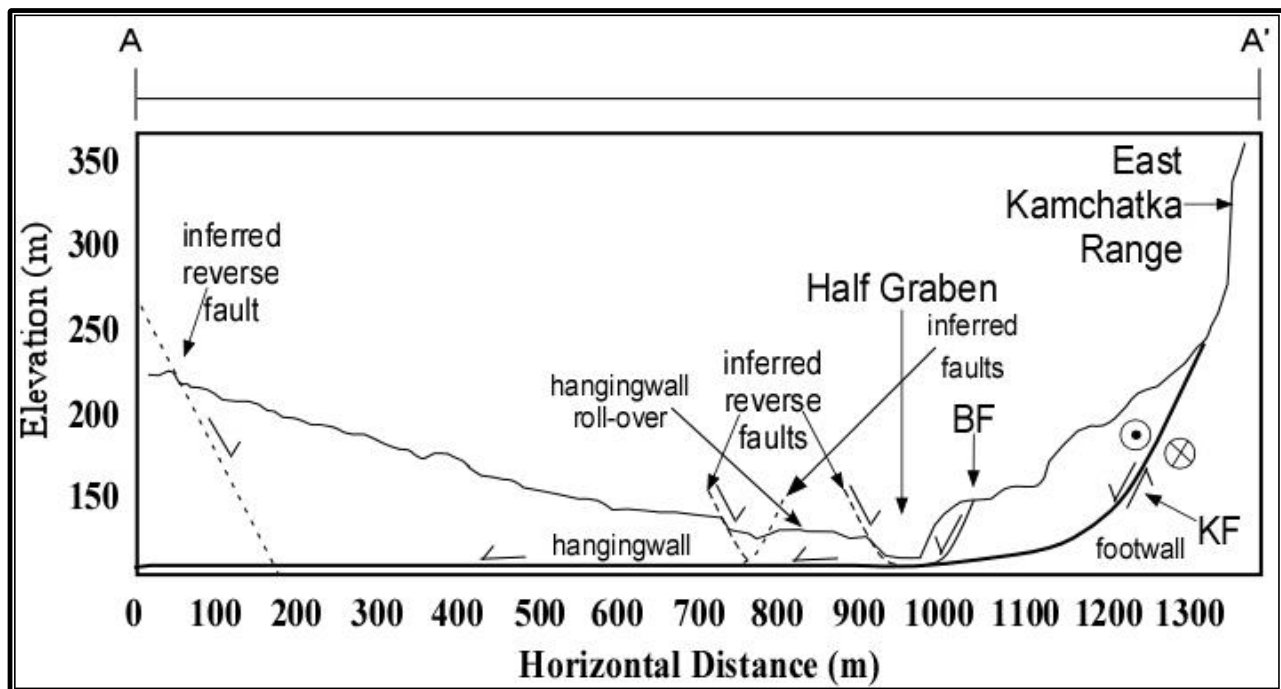


Figure 1.11: Topographic profile A – A' located on Figures 3. This section shows a system of normal faults characterized by the main KF. Note that both the KF and BF have sinistral strike-slip component, evidence for this motion is seen in the offset stream channels (Figure 10). Black arrows indicate sense of motion for the normal dip-slip component. Circle with black dot in the center indicate sinistral motion (or fault block moving toward the reader) and circles with X in the center indicate sinistral motion (or fault block moving away from the reader).

The numerous geomorphic surface features observed along the KF trace, and just to the west of it, indicate a second fault, the BF. This BF parallels the KF and merely for this reason deserves mentioning (Figure 3, 4, 10 and 11). The BF trace shows a relatively linear trace, segmentations, and

step-overs, as well as both left and right bends in the northern 2/3 of the mapped area (Figure 3). The BF does show a large sharp left bend to the south, as does the KF, but the left-step-over is inferred to link up to the BF through a complex series of fault splays that have been inferred in the south of the mapped area (Figure 3). Due to the resolution (15 m) of the data sets, the BF could not be confirmed (Figure 3). The alternative interpretation to the BF is that it could simply be a terrace riser of a Holocene river incised into a fluvio-glacial surface, skirting the terminal moraine.

1.8 DISCUSSION

The purpose of this research was to identify and map tectonic geomorphic surface features by means of ASTER GDEM Version 2, and Landsat ETM+ data sets, using Google Earth Pro images draped over the data sets' DEM models, along the trace of the KF on the east flank of the East Kamchatka Range (Figure 3, 4, and 10). With these data sets, topographic profiles were produced (Figure 11) through the use of computer application software and were utilized to define the basic surface expressions in the study area. This process allowed for measurement of the surface deformation associated with large earthquakes known to occur within the Kamchatka Peninsula region. The deformation mapping capability demonstrated in this research represent an additional benefit of Landsat ETM+ band 8 data set with the use of Google Earth Pro images draped onto the terrain models, in addition to its previously known use in recognizing volcanoes and fault traces. Offset streams were observed and measured for lateral motion.

In this study, observation of a second fault, the BF, was observed in the data sets, but due to the poor quality resolution (15 m) of the data, this could not be confirmed (Figure 3). In their finding, Kozhurin et al. 2006 discussed a second scarp within their 2006 trench site north of the Bol'shaya Khapitsa valley that is related to the KF, which bends to a NE-SW strike and branches into three splay faults and forms the principal boundary between the CKD and East Kamchatka Ranges. They

concluded that this fault, in the same way as the KF, combines roughly equal right-lateral and vertical movements. In this research, the fault discussed by Kozhurin et al. (2006) is interpreted to be the BF.

Geomorphic analyses are used to establish κ (m^2/ka) along the KF, using previously collected real ground data from Kozhurin et al. 2006 and Kozhurin 2007 (Table 1). Other parts of the Kamchatka Peninsula regions were examined using calibrated ages from Kozhurin et al. 2006 to estimated κ and slip-rates from other ground data collected by Kozhurin et al. 2008; and Pinegina et al. 2012 (Table 1). The results obtained from the CSR geomorphic analyses illustrate the utility of applying nonlinear diffusion equation models to multiple event fault scarp profiles along the KF and other areas of the Kamchatka Peninsula region.

The major advantage provided by the CSR solution is an estimated slip-rate independent of the age of the offset geomorphic surface. The CSR slip-rates must be equal to or more than the slip-rate found by dividing scarp offset by the age of the geomorphic surface, because the model predicts time elapsed since slip initiation. If the CSR slip-rate is significantly higher than that calculated from the offset and age of the faulted surface, then a period of tectonic quiescence should have preceded the onset of faulting. The Berezhnyachishkovaya-1 trench site may provide an example in this regard (Table 1, Figures 8 and 9).

Site to site variations in κ for the tephra data from [AK2006A (tephra), AK2006B (tephra), AK2006C (tephra)] range by a factor of 3 along the KF (Table 1), while variation in κ for the moraine data [AK2006A (moraine), AK2006B (moraine), AK2006C (moraine)] range by a factor of 10 along the KF (Table 1). The variations in κ from profile to profile at each site are up to 43% (CSR, $\kappa = 30 \text{ m}^2/\text{ka}$ to $70 \text{ m}^2/\text{ka}$).

The calibration process assumes that diffusivity is constant over time, but climate has changed dramatically since 100 ka due to glacial cycles that may have caused diffusivity to fluctuate as well as climate variations from one part of the region to another. A wetter climate should increase diffusivity,

and therefore our calculated κ and slip-rates for the Izvilistaya trench site are acceptable, given that the trench site is located very near the coast on the east side of the East Kamchatka Range, whereas the other trench sites are inland and west of the East Kamchatka Range, and would experience less moisture. The transition from diffusive processes to nondiffusive processes will probably vary regionally due to climate and aggregate properties of the sediments. Soil development and vegetation may also progressively stabilize slopes and cause diffusivity to decrease over time.

The fault zone is characterized by pulses of sinistral strike-slip and normal dip-slip activity, which are evident in the seismic record (Figure 2), and in the multiple structural and geomorphic surface features recorded in this study (Figure 3, 4, 10, and 11). It is plausible, in light of observations from this and previous studies conducted in the region, that renewed faulting is imminent, with the capacity to generate significant regional shallow earthquakes ($\sim M6.5$). Arguments have previously been made that shallow earthquakes constitute a source to be considered in seismic hazard evaluations, in as much as earthquakes related to the subduction of the Pacific Plate beneath Kamchatka (Fedotov et al. 1974; Kozhurin et al. 2006; Saltykov and Kugaenko, 2000). Both the KF and the BF dip NW and are characterized by combined dip-slip normal and sinistral strike-slip motion.

Japan, for example, has similar types of structural features to those that are observed in this study. The 1999 study by Kamata and Kodama discusses classic structural features of island arc in a subduction system along the Japanese islands. Although previous works noted dextral offset moraines (Kozhurin, 1990), this dextral offset is almost certainly a local consequence of displacement transfer through the left-stepping bend of the KF. All regional geomorphic evidence points to the conclusion that the KF and BF represent normal faults or sinistral-normal oblique-slip fault systems (Figure 10). That is, if the KF had a dextral component, the left stepping fault bend within the study area would be a restraining bend, yet all observations demonstrate extension within this zone.

One important question remains unresolved, in that there are some convergence vectors that have a slight dextral component. I speculate that the dextral motion may be related to magmatic activity, a classic case of the “granite room problem,” where intrusions force extension in the upper crust (Tikoff and Teysier, 1992). This region’s structural geometry has evidence for pull-apart basin extension, which suggests that the entire EKFZ may move as an active transtensive zone, with the normal component particularly significant in the segment of the zone that forms the eastern margin of the CKD (Figure 12). Moreover, displacement on this fault zone may define a regional-scale forearc coastal block moving ESE separately from the rest of Kamchatka.

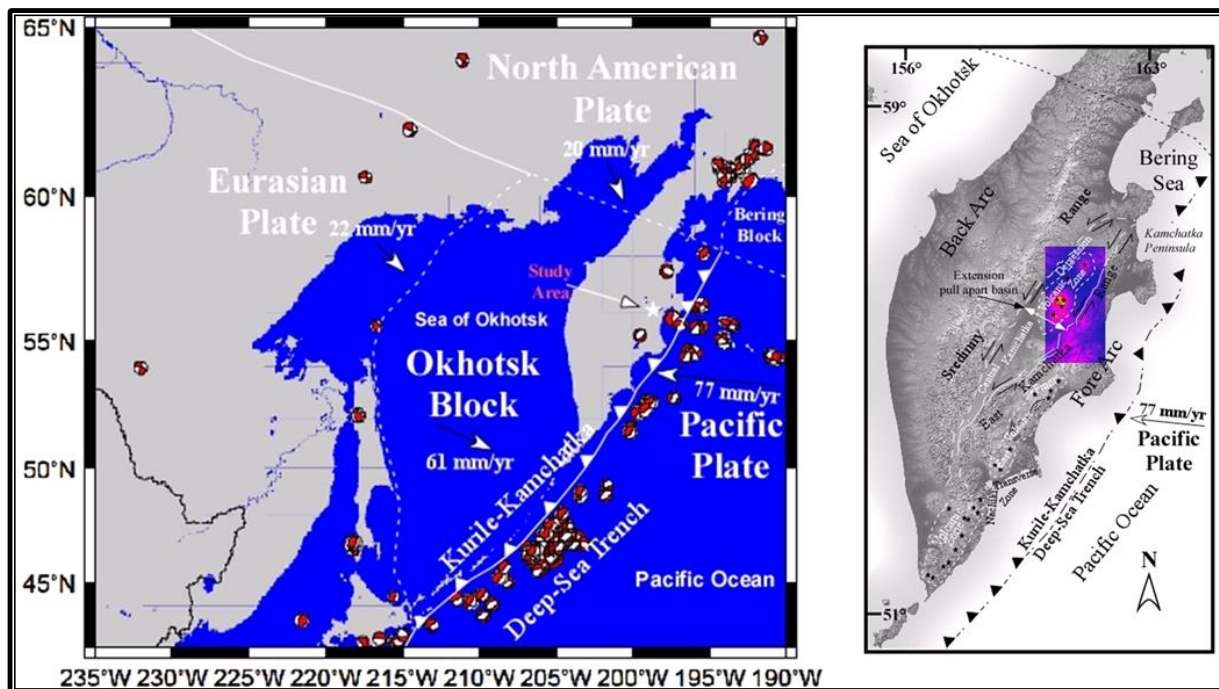


Figure 1.12. Small map shows regional tectonics, plate motion relative to Okhotsk block and shallow depth seismic focal mechanisms (0 - 30 km) in the last 5 years. Seismic data is from the Global CMT Catalog Search webpage. Plate motion was determined using UNAVCO Plate Motion Calculator webpage. White lines indicate plate boundaries. White line with “teeth” indicates overriding plate. Dashed white lines indicate assumed plate boundaries. White star indicates study area. Large map shows major Neotectonic elements of the Kamchatka Peninsula and extension motion of pull-apart basin. Solid white lines are active faults with black arrows indicating sinistral motion; large white dashed lines were inferred. Black stars mark major Holocene volcanic centers, areas bounded by dotted white lines are volcanic zones. Kurile Kamchatka trench is indicated by dashed black line with “teeth” indicating overriding plate east of the fore arc. Pull-apart basin extension motion is indicated by white line with double arrow heads. Study area is indicated by cyan color and 3D can be viewed using 3DChrom glasses. Image modified from NASA and Kozhurin et al., 2006 paper.

More importantly, this Holocene island arc setting offers the relatively unexplored possibility of carrying out paleoseismic, structural geology, and geomorphology investigations directly through 3D visualization with high resolution terrestrial or airborne Light Detection and Ranging (LiDAR) data, with 1 m or less resolution (accuracy). These methodologies can provide insights into the paleoseismic history and the temporal relationships between tectonics and volcanism. This method is a quick and inexpensive way to gather data for a regional tectonic study and establish diffusive rates of tectonic activity with high resolution data such as LiDAR.

1.9 CONCLUSION

Determination of geomorphic surface features with the use of ASTER GDEM and Landsat ETM+ data with Google Earth Pro images draped over the DEM models assists in 1) identification of geomorphic spatial patterns, and 2) understanding of active faulting associated with the active tectonics in the region. This study demonstrates that the CSR solution is a good means to estimate the time elapsed since slip initiated on a faulted surface, and therefore can be used to estimate slip-rate and relative tectonic activity more accurately than by simply dividing scarp offset by the age of the ruptured surface. Diffusion equation models such as CSR solutions replicate the morphology of multiple-event fault scarps, though care must be used for scarps more than ~25 m high. Tall scarps often exhibit hummocky topography, indicating that degradation may be controlled by nondiffusive processes such as slumping and creep (Mattson and Bruhn 2004). Offset and age data from previous paleoseismologic trench studies such as Kozhurin et al 2006, Kozhurin 2007, Kozhurin et al 2008 and Pinegina et al. 2012 can be used to calibrate diffusion equation models and generate either multiple-event profiles based on several individual rupture events, or to generate CSR profiles to estimate slip-rate for a surface offsetting at a constant rate. The application of the CSR model indicates that slip-rates vary by up to an order of

magnitude from the north (Ust-Kamchatka village) to the central (KFZ) to the south (Bystrinsky graben) and that the fault displacement is not uniform through time.

1.10 SUMMARY

This research conducted 3D virtual geomorphic mapping by employing ASTER GDEM Version 2 and Landsat ETM+ data sets by means of draping Google Earth Pro images over the DEM models. The CSR nonlinear diffusion analysis was complete for the KF, using previously collected ground trench data by Kozhurin et al. 2006 to estimate κ and slip-rates. The Kozhurin et al. 2006 calibrated ages and results from this study were then compared with Kozhurin et al. 2007, Kozhurin et al. 2008, Pinegina et al. 2012 trenching results to estimate κ and slip-rates for the Kamchatka Peninsula region. The values of diffusion constants obtained in this study are the first data of this kind ever reported for Kamchatka Peninsula, Russia, with its specific climate conditions. These results are valuable in understanding the Holocene paleoseismic history of this region, establishing a geomorphic foundation that can be used to compare it to other regions with similar tectonic and geomorphic environments, such as the Katalla area of southern Alaska.

Chapter 2: Ragged Mountain - Katalla Area, Alaska

2.1 ABSTRACT

High resolution LiDAR and aerial photography data sets are widely used for evaluation of surface manifestations of active tectonics. This study evaluates surface geomorphology using a LiDAR DEM with high resolution aerial photography draped on parts of the terrain model and discusses the pros and cons of virtual geomorphic mapping. Analysis of the high resolution digital elevation model and aerial photography are providing new insight into the role of tectonics versus gravitational deformation. This improves the understanding of the tectonic history and allows for seismic hazard assessments in the region. The study area is located in southern Alaska in the western edge of the St. Elias Orogen where the Yakutat microplate is colliding into Alaska. The study area contains hundreds of geomorphic surface features indicative of active deformation such as fault scarps, ponds, and off-set streams, but there has been a challenge in separating tectonic structures from gravitational collapse features. The LiDAR DEM together with aerial photography was used to create an accurate geomorphologic map of the study area along the length of the east flank of Ragged Mountain, which contains the Ragged Mountain fault scarp, uphill facing fault scarps, flexural-slip fault scarps, talus deposits, landslides, an alluvial fan, and stream channel patterns. In order to determine the type of displacement on fault scarps two sets of profile surveys were examined. A total of 98 short profiles and 30 long topographic profiles were constructed to distinguish thrust versus normal faulting. One working hypothesis is that uphill facing normal fault-scarps along the Ragged Mountain fault trace represent extension above a buried ramp in a thrust. We evaluate this hypothesis by developing a theoretical model related surface extension to thrust slip using a fault-parallel flow thrust model. This model indicates that relatively steeply dipping thrusts transferring slip to a flat ramp produce a hanging-wall extension that approaches the magnitude of the slip on the thrust, suggesting the Ragged Mountain extensional scarp may represent a structure produced by this process. In this hypothesis, hanging-wall extension produces the observed scarps but the thrust slip is primarily blind.

2.2 INTRODUCTION

For many years remote sensing data have been routinely used in geological studies. Some of these studies are as basic as using Google Earth applications for general reconnaissance to more sophisticated methods for energy exploration or development of active tectonic models for a region. Recent studies have utilized Light Detection and Ranging (LiDAR) data because it is a fast method for sampling the earth's surface with a high-density, high-accuracy point cloud survey that produces high accuracy Digital Elevation Models (DEMs) (Li et al. 2010; Chiang et al., 2012). In this study an evaluation was done on the geomorphic Three Dimension (3D) virtual mapping along with a discussion of the benefits and short-comings of this method.

The Ragged Mountain fault is a part of a fault system in southern Alaska that represents a suture zone that was reactivated during Neogene contraction in the western end of the St. Elias orogen (Figure 2.1). Tysdal et al., (1976) describe the Ragged Mountain fault as a very shallow (8°), west-dipping thrust fault that was reactivated in the Late Holocene by westward-directed gravity sliding. They inferred at least 180 m of normal slip, in a direction opposite to the (relative) eastward thrust transport of the structure inferred from stratigraphic juxtaposition. Most recently this gravity sliding hypothesis has been questioned (Bruhn et al. 2004; Pavlis et al. 2004; McCalpin et al., 2011). This paper uses 3D virtual geomorphic mapping observations and interpretations of high resolution topographic models constructed from the LiDAR survey to evaluate these alternative hypotheses.

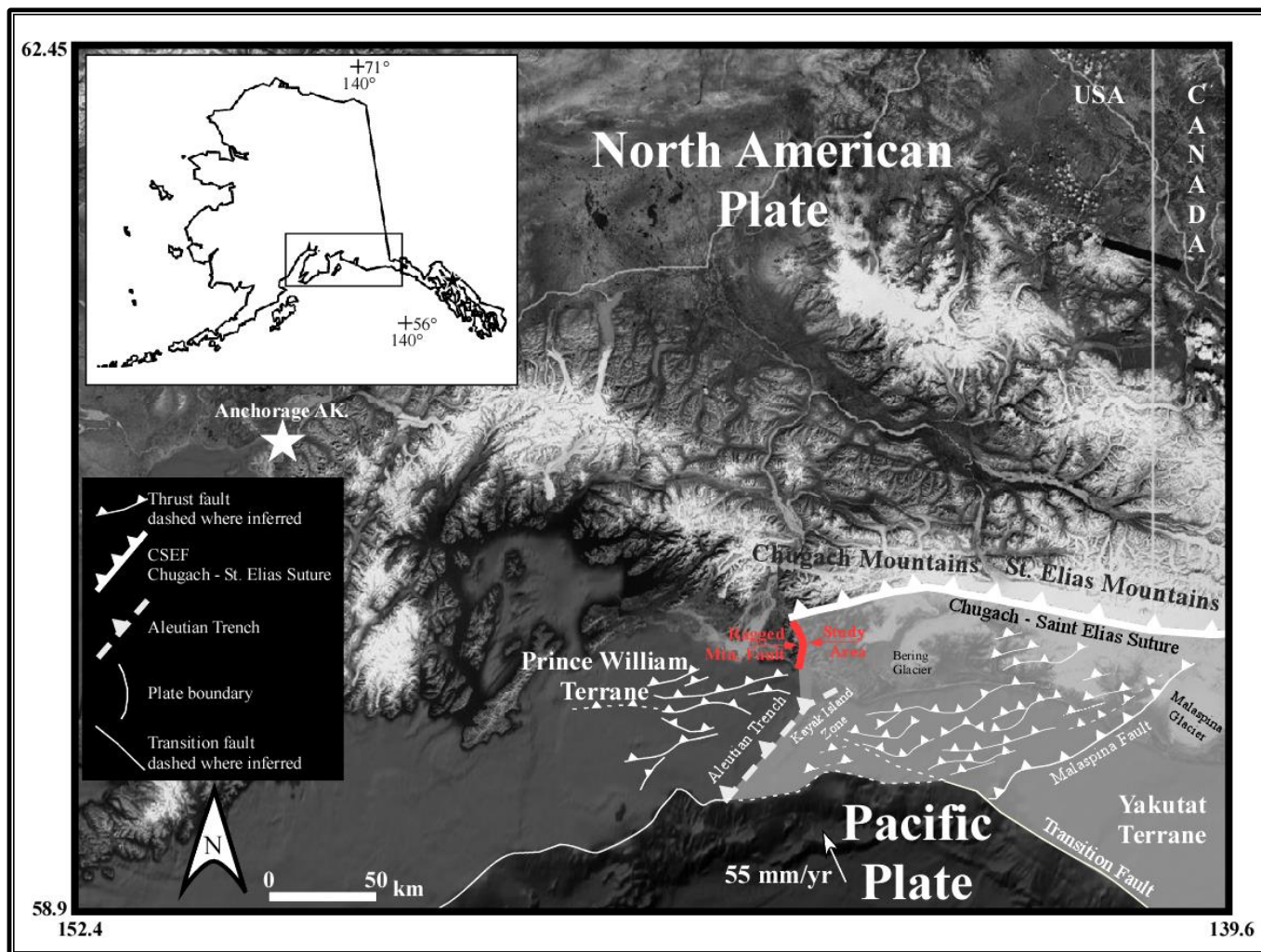


Figure 2.1: General regional tectonics map of northeastern Pacific Plate and Yakutat microplate (shaded areas) located in southern Alaska. Figure is modified from Pavlis and Bruhn (2011). Structural features and plate vector are from Bruhn et al. 2004.

The paper begins with a new geomorphologic map of the study area which is used to evaluate the origin of the Ragged Mountain fault scarp system through mapping of the scarp, talus deposits, landslides, and stream channel patterns. 134 topographic profiles were constructed on the numerous scarps to illustrate the curvature of the scarp surfaces and evaluate their origin. We then evaluate the origin of the scarps by developing a simple geometric model relating extensional fault scarps to an underlying fault ramp. We discuss the data in the context of this model and conclude that the extensional scarp structures examined by Tysdal et al. (1976) represent flexural extension above a thrust system. Analysis of scarp heights along the structure, together with the model suggest an increase in

slip from north to south along the Ragged Mountain fault from 0.6 to 11.9 m using both the models and collected data.

2.3 TECTONIC BACKGROUND AND PREVIOUS WORK

The Katalla area is located in the western portion of the Chugach - St. Elias orogen in Southern Alaska (Figure 2.1). Prior to ST. Elias Erosion/tectonic Project (STEEP), studies by Plafker (1987), Plafker et al. (1994), Bruhn et al. (2004), and Pavlis et al. (2004) established the general tectonic framework of the collision of the Yakutat microplate into Alaska along the northeastern part of the Aleutian megathrust (Figure 2.1). The Yakutat microplate is internally undeformed, but is bounded on all sides by actively deforming zones: to the east, the microplate is a slip-partitioned, dextral-transpressional orogen with strike-slip localized along the Fairweather fault and with an associated contractional flower-structure along the strike-slip system (Bruhn et al., 2004; Doser et al, 2007); to the southwest the Transition fault separates the Yakutat microplate from the Pacific plate and represents a Cenozoic strike-slip fault weakly reactivated during the collision (e.g. Gulick et al., 2000, 2007 ; Christeson et al., 2010); and the northern margin is a complex fold and thrust belt that is the object of this study. The suture at the leading edge of the St. Elias collision system is formed by the Chugach St. Elias and Ragged Mountain faults which separate Paleogene subduction-related assemblages of the Orca Group from Cenozoic sedimentary cover rocks of the Yakutat terrane (Plafker, 1987; Pavlis et al., 2004).

Bruhn et al. (2004) and Pavlis et al. (2004) showed that in the Katalla region collision of the microplate has created a structural syntaxis, deforming the suture from a roughly E-W trend along the Chugach-Saint Elias fault to NNE trend along the Ragged Mountain fault (Figure 2.1). Bruhn et al.'s (2004) mapping used structural form lines of deformed sedimentary rocks to show that these rocks were partly refolded earlier developed folds and faults within the sedimentary rocks of the Yakutat microplate. Glacial erosion and sculpturing of Tertiary sedimentary rocks deformed by thrust to oblique

slip faulting and folding creates elongated mountain blocks that are surrounded either by flat-floored valleys filled with glaciofluvial and marine sediments, steep canyons, or in some cases glaciers (McCalpin et al., 2011). The mountains are susceptible to mass wasting due to steep glacial-carved mountain slopes, rapid retreat of many glaciers from mountain walls, heavy precipitation, and strong ground motion triggered by earthquakes (Plafker, 1987; Meigs & Sauber, 2000; Jaeger et al., 2001; Bruhn et al., 2004).

Geodetic surveys of the region show that the Yakutat microplate is moving NW to NNW at ~45-49 mm/yr with respect to interior Alaska (Elliott et al., 2010; Elliott, 2011), creating considerable seismicity and generating some of the world's largest earthquakes along the Aleutian megathrust (Plafker, 1969; Shennan et al., 2008; Li et al., 2010; McCalpin et al., 2011). Elliott et al. (2007) determined velocity gradients within the interior of the microplate which they interpreted as strain accumulation above buried faults that also represent potential seismic sources. Block models of the geodetic data indicate complex interactions within the western part of the St. Elias orogen, consistent with the observed surface geologic complexities (Elliott, 2011). Similarly, seismic studies by Ruppert (2008) and Doser et al. (2007) used earthquake focal mechanism solutions to indicate the predominantly mixed strike-slip to thrust-faulting stress regime in the western Saint Elias orogen, which is consistent with NW-to-W-trending maximum horizontal compression axes. Plafker (1969) and Tuthill and Laird (1966) reported that rupture of the Aleutian megathrust during the M9.2 earthquake of March 1964 triggered coseismic uplift within the western Saint Elias orogen, and also triggered many landslides, snow avalanches, and widespread surficial deformation of Quaternary deposits.

The complex bedrock geology of the Katalla region (Miller et al., 1961; Bruhn et al., 2004) together with geodetic studies and seismicity suggest the region is actively deforming, but the surface manifestation of this deformation is poorly understood. Although numerous surface ruptures are recognized in this region, most of these structures are gravity-related sackungen (Li et al., 2010; Pavlis

and Bruhn, 2011; McCalpin et al., 2011). The Ragged Mountain fault system, however, displays one of the longest continuous surface ruptures in the orogen (Bruhn et al. 2004) and its origin is a key problem to the understanding of the Neotectonics of the orogen.

2.4 THE STUDY AREA: RAGGED MOUNTAIN

The Ragged Mountain study area (Figures 2.2 and 2.3) is dominated by Holocene and Quaternary surficial deposits. They include: 1) extensive, variably active cobble to boulder talus along the eastern flank of the Ragged Mountains; 2) unconsolidated alluvial sand and gravel in active stream channels; 3) landslide deposits; and 4) Quaternary glacial drift. In addition, loess cover is variable, leading to thick soil developments over large regions. These unconsolidated deposits rest on complexly deformed rocks that include the Eocene Stillwater and Tokun Formations of the Yakutat terrane and the metavolcanic unit of the Orca Group (Plafker, 1987). The Stillwater Formation is estimated at more than 610 m thick; consisting of mainly black, thin-to medium-bedded carbonaceous micaceous siltstone, finely laminated micaceous siltstone, and finely laminated micaceous medium-grained sandstone (Plafker, 1987). The Stillwater Formation was deposited in outer littoral to bathyal environment and the base of the Stillwater Formation is not exposed (Tysdal et al. 1976). The Stillwater Formation is strongly deformed, characterized by tight folds and sheared carbonaceous siltstone that has a “coaly” appearance (Tysdal et al. 1976). This deformation has been identified in three small outcrop areas along the front of Ragged Mountain: on the west shore of Little Martin Lake, at the drainage divide east of the easternmost part of the Ragged Mountain fault, and in the uppermost part of Clear Creek (Tysdal et al. 1976). The volcanic unit of the Orca Group (Paleocene) is described in the study area as being at least 762 m thick, light-to dark-green cliff-forming massive metavolcanic rock composed of thin- to thick-bedded agauagene tuff and tuff breccia, agglomeratic tuff, basalt, and pillow basalt.

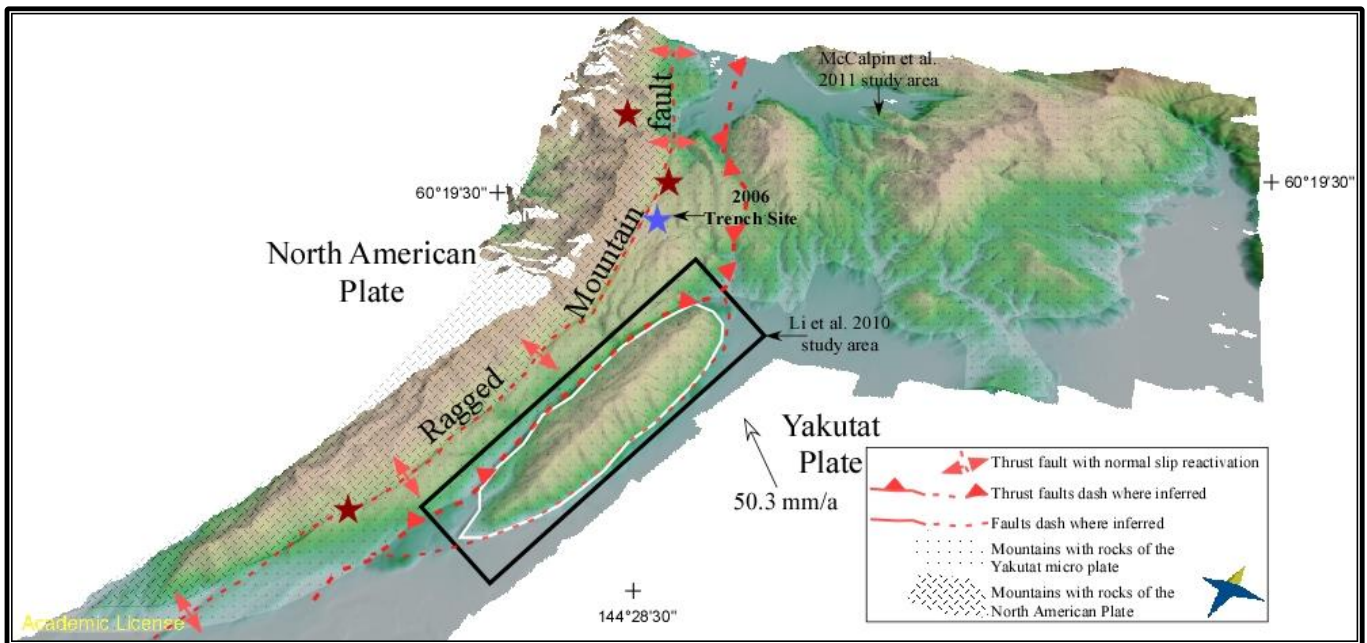


Figure 2.2: Unfiltered Light Detection and Ranging (LiDAR) data in false colors collected from the southern Alaskan data set acquired during the summer of 2005 St. Elias Erosion and Tectonics Project (STEEP) of Katalla Alaska. Spatial resolution of the LiDAR data vertical and horizontal resolution is 1 meter and 15cm, respectively. Fault traces, surface ruptures, and strike and dip data are from STEEP 2005 and 2006 field seasons, doctors Terry L. Pavlis and Ronald L. Bruhn 1998, 1999, and 2003 field seasons, and Miller 1961. Yakutat Plate motion vector is from Elliott et al., 2010 and Elliott, 2011. Modified from Li et. al. (2010).

Tysdal et al. (1976) mapped the Ragged Mountain fault for ~30 km along the eastern flank of Ragged Mountain (Figure 2.2). The trace of the fault is convex eastward with a recognizable trace from just north of Martin Lake to just south of Martin Island where it disappears offshore. Tysdal et al. (1976) recognized that the Ragged Mountains fault originated as a thrust system coincident with the Yakutat-North America suture, but inferred that the prominent Quaternary scarp formed by reactivation and back-sliding along the Ragged Mountain fault (Figure 2.2). Using the main scarp morphology and maps available at the time, they argued for 180 m of normal slip based largely on the morphology of the present scarp (Tysdal et al., 1976). Since the Tysdal et al. (1976) study no other fault scarps of similar length have been identified, even though, regionally, stresses are favorable for reverse and strike-slip faulting (Ruppert, 2008). Li et al. (2010) and McCalpin et al. (2011) focused attention on sackungen (uphill-facing scarps) or “antislope” scarps that occur within mountains throughout the region mostly to

the east of the study area (Figure 2.2). Both papers describe how most of these scarps parallel bedding planes in Tertiary strata, and offset Quaternary deposits. This observation led Carver and McCalpin (1996) to the question: “are these scarps caused by superficial deformation, or are they manifestations of tectonic processes related to active folding above buried faults?” This question led Bruhn et al. (2004) to re-examine the origin of the Ragged Mountain fault, and in 2005 and 2006 we conducted further field studies to delineate the fault and evaluate its origin.

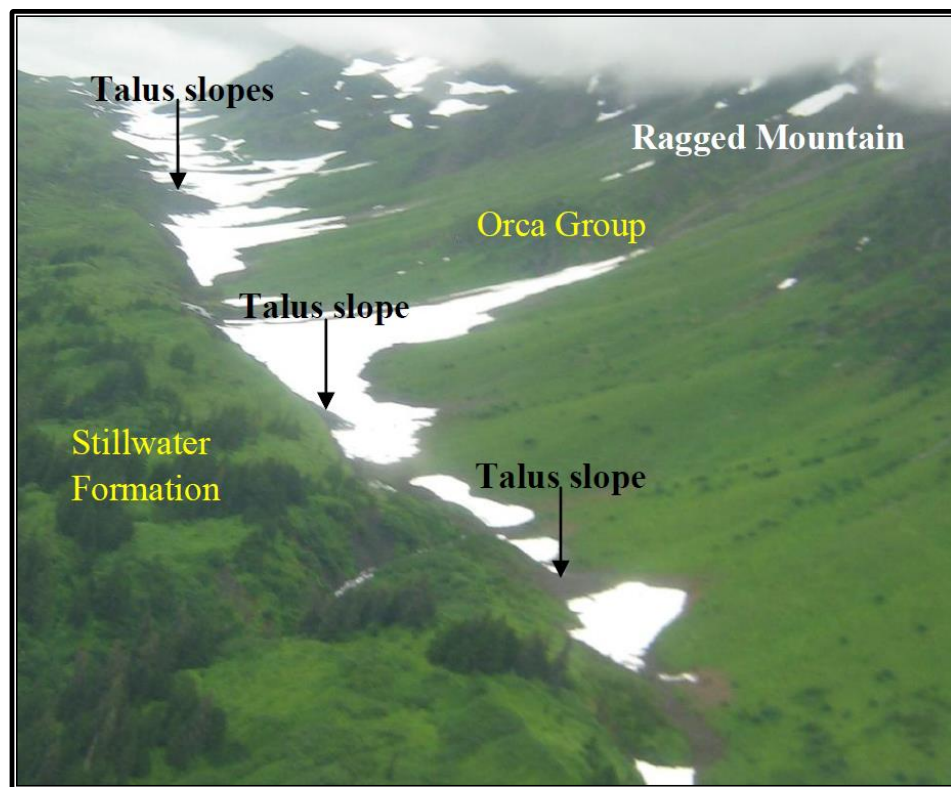


Figure 2.3: Reconnaissance photo taken in summer of 2011, looking south-southwest near the high pass in the middle of the eastern flank of Ragged Mountain which is to the right in the figure with rocks of the Orca Group cropping out of the cliffs. On the left in this figure talus slopes and the linear edge of the snow fields indicate the Ragged Mountain fault scarp location. For location of site see Figure 2.2.

The 2005 reconnaissance group discovered evidence for active thrusting along the fault and the hypothesis was tested in 2006 with a paleoseismology trench. Details of that study are reported elsewhere (McCalpin et al., in preparation) but that work showed that at least in the trench site, a thrust system reaches the surface. Unfortunately, because there is only one trench site and the main scarps of the Ragged Mountain fault system are clearly extensional this begs the question of extending the results

of the trenching to the entire fault system. Thus, this study was undertaken to address this question through a more thorough treatment of the geomorphology and the fault scarps of the Ragged Mountain system.

Tysdal et al.'s (1976) interpretation of Ragged Mountain fault as an extensional structure has profound implications for the local active tectonics, and thus, requires some discussion here. Figures 2.3 and 2.4 show two views of the trough that Tysdal et al. 1976 discussed in their report showing a prominent linear feature accentuated by snow fields in association with a prominent, uphill facing scarp and an associated trough. Tysdal et al. 1976 used the width of this fault trough, ~180m, as an estimate of the normal slip across the scarp together with ages of glacial deposits to estimate slip-rates of ~10 cm/yr. This rate seems unlikely given that plate convergence rates are half this rate, yet if the motion were entirely surficial landsliding, this rate is allowable. Nonetheless, we present evidence below that this net slip estimate is an overestimate because erosion has modified the trough and surface correlations are unreliable. Instead, the Ragged Mountain fault is a system of predominantly uphill-facing, extensional scarps, many of which lie to the west, and topographically above, the fault trace inferred from the fault-trough alone.

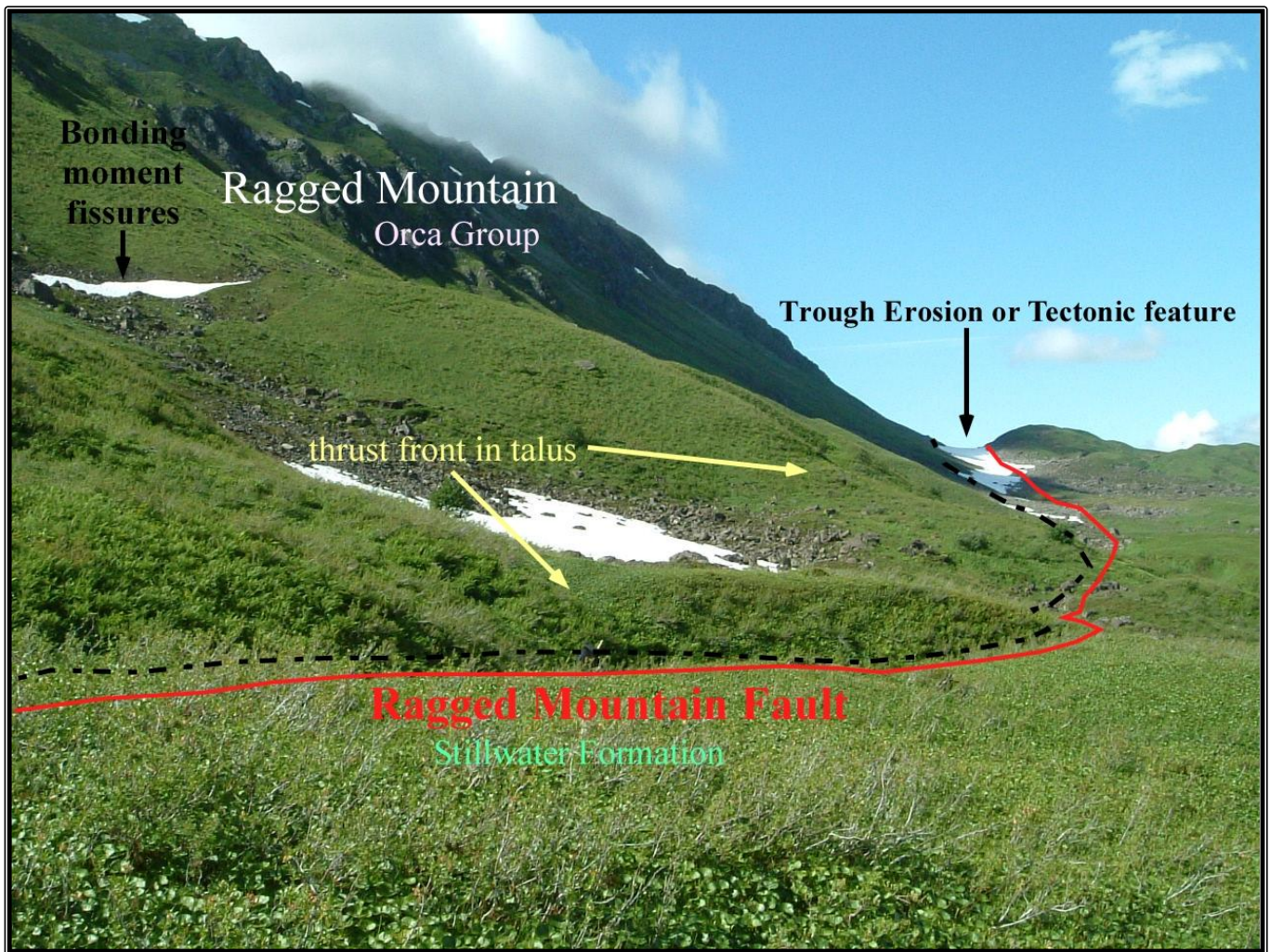


Figure 2.4: Photo taken in the summer of 2005 is looking north-northwest; Martin Lake is to the right of the trough beyond the pass. This photo shows the best view of the trough that Tysdal et al., 1976 discussed in their report. The ridge on the right side of the trough is underlain by the vertically dipping or very steeply dipping Stillwater formation bounded by the Ragged Mountain fault. The big cliffs on the left are the Orca Group. The trough itself sits in the middle of this figure. The extensional scarp is located just above the big patches of snow. There are smaller patches of snow near the Orca group (to the left in this figure) which is the western boundary where the Ragged Mountain extensional scarp starts. The extensional scarp follows down past the cliffs of the Orca group. Following the snow down the slope, where there is a small blip of green, is the end of the eastern boundary of the extensional scarp. See figure 2.2 for location.

2.5 METHODS

2.5.1 METHOD: THE DATASETS

This study is an attempt to test the alternative hypotheses for the origin of the Ragged Mountain fault scarp using new data that were acquired during the STEEP study. We began by georeferencing National Center for Airborne Laser Mapping (NCALM) high-resolution aerial photography with ~ 15 cm ground resolution using the unfiltered LiDAR data. This procedure allowed for the detailed exploration of the study area, and specific sites were selected to construct topographic profiles primarily to examine surface ruptures that are prominent throughout the LiDAR dataset. Interpretations and identification of the origin of uphill-facing scarps and reverse faulting with extensional scarps, caused by hanging wall flexure, was possible using the 2005 - 2006 and 2011 field evidence; Li et al. 2010 and Pavlis and Bruhn 2011 research, and computer visualization techniques that were carried out on the high-resolution LiDAR data. The details of the LiDAR dataset and data processing are contained in Table 1 of Pavlis and Bruhn 2011 paper and in the metadata with the data archive at www.opentopography.org.

The high resolution aerial photography was collected alongside the LiDAR data with roughly 15 cm ground resolution. Unfortunately NCALM lost the georeferencing information for these data and the aerial photography were delivered as raw data files with only a crude flight-line map. Moreover, the digital imagery was recorded as unprocessed tiff images with no automated brightness/contrast adjustments such that nearly half of the images were unrecognizable without initial processing. Therefore the imagery required significant processing to be usable and then required manual georeferencing from ground control points.

The loss of georeferencing information for the NCALM files led to a tedious recovery process that strongly limited the scope of this study. The image catalog from the study is ~14,000 images contained in 70 flight line files that had to be manually viewed to determine quality for use. Then an

automated brightness/contrast adjustment was done to all images. Those images that were still unrecognizable or blurred by poor lighting were not used. The images were then manually viewed to select sets of images that contained useful scenes for this analysis, eliminating imagery from heavily forested areas where the imagery would be of marginal use. Selected images were then manually georeferenced using ArcGIS10 Spatial Referencing Properties and orthorectified using the image software. Ground control points for the georeferencing were obtained from the shaded-relief imagery prepared from the unfiltered LiDAR DEM by direct comparison to imagery. The images were not systematically georeferenced in numerical order because some of the study area was heavily vegetated and flight lines had significant overlap (Figure 2.5). In general when manually georeferencing an image from ground control points, four points are needed, but it is ideal to have more than four. The more ground points the more accurate the match of the topography of the image. At one point a system was setup to skip every two image, but because of the crude flight path that method was thrown out in some areas, and in other areas there were no photos collected at all to assist in identification of structural or geomorphic features and aid in interpretations.

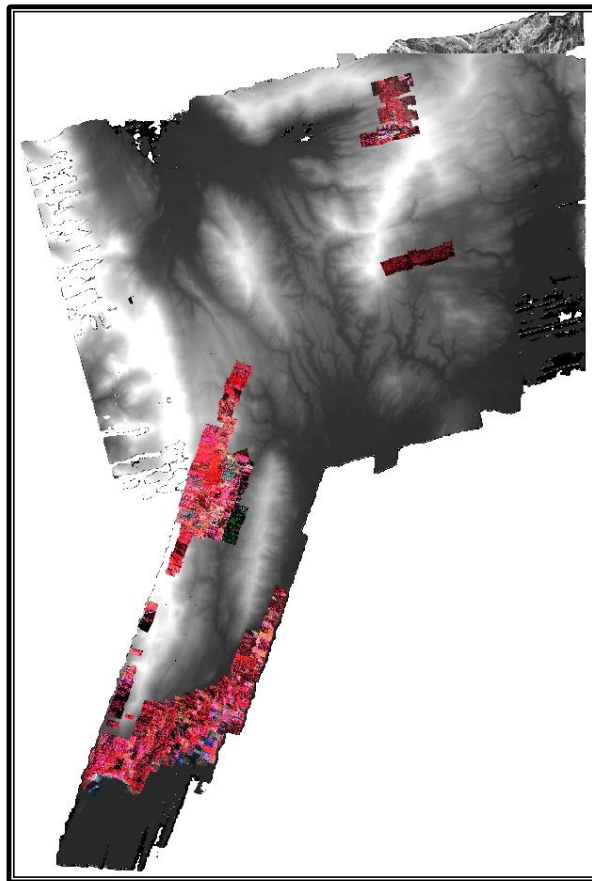


Figure 2.5: Manually georeferenced NCALM images draped over the high resolution filtered LiDAR DEM.

2.5.2 METHOD: 3D VIRTUAL MAPPING AND SURVEYING

3D virtual geomorphic and structural mapping were accomplished through analysis of previously collected field data, data collected from remote sensing datasets by means of GIS and reconstruction software; Esri's ArcGIS 10 and Midland Valley's Move 2012. The focus of the study was to map individual faults, faults scarps, and offsets recorded in bedrock and stream patterns. Initially, for data collection of fault scarp profiles, a workflow was based on the study of Mattson and Bruhn 2001; DuRoss and Bruhn 2004; Pavlis and Bruhn 2011, and Cervera Heinlein 2013 (manuscript in press) using remote sensing and computer application based approaches. Fault scarp profiles were constructed using the 3D analyst extension to ArcGIS 10. All topographic profiles were drawn from west to east for consistency and are perpendicular to fault scarps. Horizontal and vertical errors are estimated to be ~30

cm and 10 cm, respectively based on the LiDAR dataset. Scarp profile curves were initially compared with two dimension dislocation fault models to determine fault type of the scarps and assist in resolving the origin of the surface ruptures; but this did not provide any insight and this method was eventually abandoned.

In general, fault scarps represent the best recognizable natural surface expression of seismic activity along active fault systems (e.g., Wallace, 1977; Yeats et al. 1997; Baran et al. 2010). Fault scarp morphology studies have been conducted to constrain fault kinematics and particularly scarp degradation, often by using geomorphic dating techniques which are conducted along normal faults (Bucknam and Anderson, 1979; Hanks et al. 1984; Avouac 1993; Arrowsmith et al. 1998). These studies are carried out where fault scarps are continuously exposed in areas of relatively simple and uniform topography, and where single isolated fault scarp profiles can be easily acquired using labor intensive techniques such as those applied by Arrowsmith et al., 1998. These techniques are difficult to apply in areas where small scarps are exposed, or where scarps are very subtle (Baran et al. 2010). As a result the patterns that result from fault scarps that are superimposed on a more complex and dissected topography have not been adequately explored at smaller spatial scales and compared with a larger spatial scale as considered by Landgraf et al. (2009); Baran et al. (2010); Li et al. (2010); and Pavlis and Bruhn (2011). Solutions to this dilemma are provided by recently developed high resolution LiDAR scanning and terrestrial laser-scanning technologies that are rapidly developing into effective research tools in tectonic geomorphology (Baran et al. 2010).

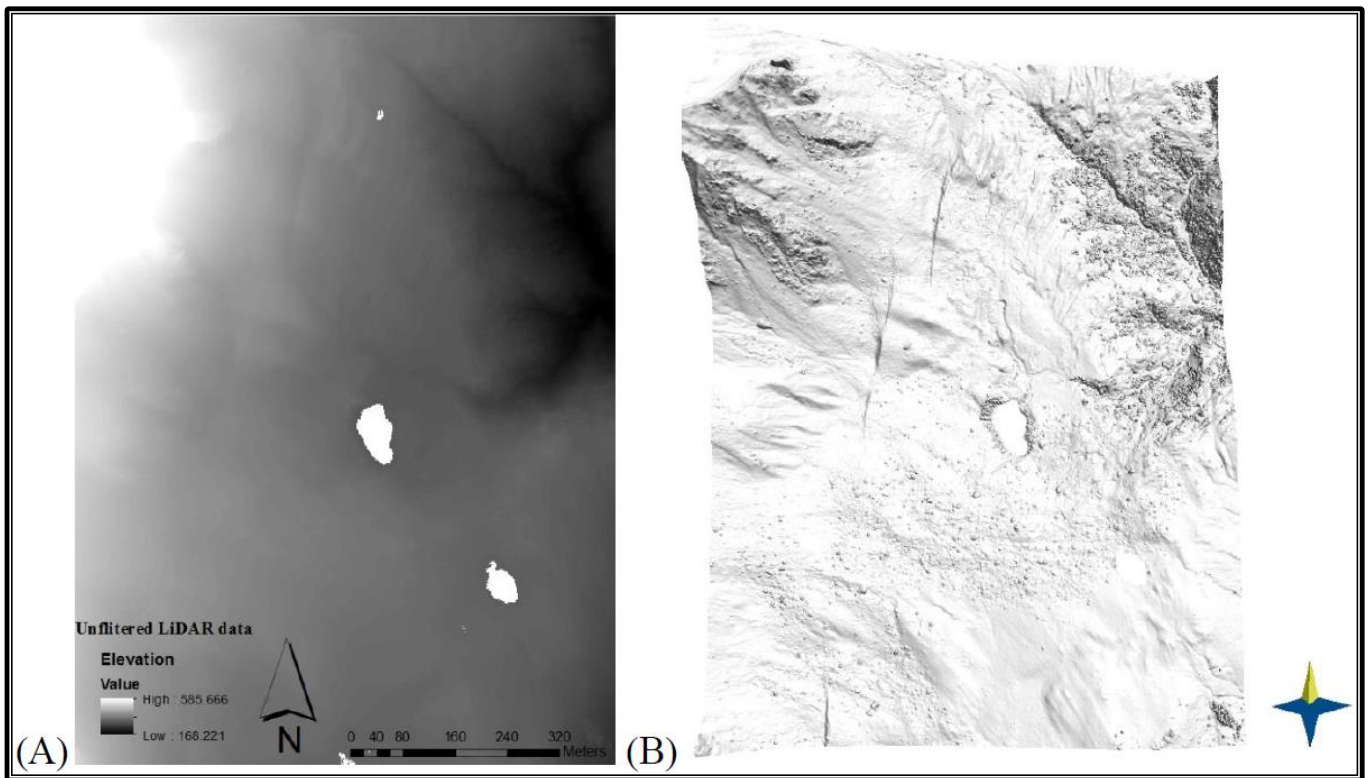


Figure 2.6: 1:5000 scale maps of the Unfiltered LiDAR data of the 2006 Ragged Mountain trench site view in ArcGIS 10 (left) and detailed LiDAR DEM viewed in Move (right).

“Sackung” is a term used to describe an uphill-facing scarp that forms by lateral spreading of mountain flanks. Li et al. 2010 explain that in modern terminology sackungen refers to linear geomorphic features produced by gravitational spreading in slopes and that scarps formed by tectonic deformation during folding may also face uphill and are similar to sackungen in appearance. Resolving the origin of the surface ruptures is important to understanding the neotectonics because sackungen are not tectonic in origin, aside from their potential correlation to hill slope failure caused by strong ground motion during earthquakes (Pavlis and Bruhn, 2011). In contrast, the alternative hypothesis is that sackungen are related to fold growth which provides important constraints on the nature and location of active tectonic structures, including the implication that there may be refolding of older structures (Bruhn et al., 2004) and is an ongoing process (Pavlis and Bruhn, 2011). In order to address the problem this study utilized the bare-earth DEM prepared by NCALM (Fig. 2.2) to produce hillside shaded-relief images within the study area (Figure 2.6 and 2.7A). Following that other computer

applications (spatial analysis) were combined (Figure 2.7B) with mosaic draped aerial photography images (Figure 2.7C), to analyze and map the structures and geomorphic surface ruptures and other subtle topographic features associated with the bedrock geology to construct three dimensional geologic models and relate those models to the surface ruptures.

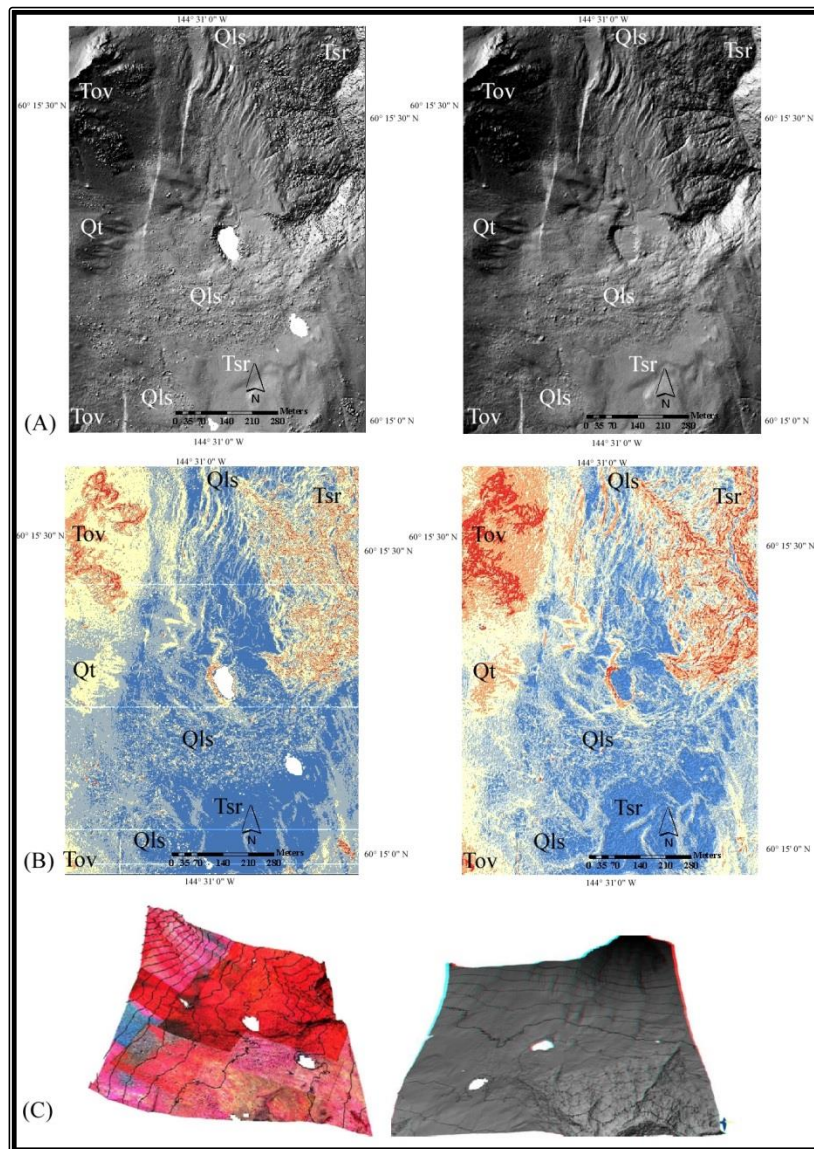


Figure 2.7: 1:5000 scale maps of different views of the LiDAR data unfiltered left side and filtered LiDAR DEMs right side (2.7A), unfiltered left and filtered right slope spatial analysis of the LiDAR DEMs (2.7B), and (2.7C) two perspective of 3D contour maps one facing north with the ALSM mosaic image draped onto the LiDAR DEM displayed in ArcGIS (left) and the other 3D contour map of the LiDAR DEM facing west displayed in Move (right), this image can be view with red blue 3D glasses. Tov = Paleocene volcanic unit of the Orca Group, Tsr = Eocene Stillwater Formation, Qt = Holocene Talus Deposits and Qls = Holocene Landslide Deposits. Blue star indicates the location of camp site in 2.7A and 2.7B.

2.6 RESULTS OF INVESTIGATION – 3D VIRTUAL MAPPING AND SURVEYING

2.6.1 The Nature of the Ragged Mountain fault scarp

A first-order observation of the Ragged Mountain area is that the trace of the Ragged Mountain fault has a distinct convex eastward shape, which is characteristic of many thrust fault systems (Figure 2.2, 2.3, and 2.8). The Ragged Mountain fault trace is not exposed throughout the study area due to unconsolidated Holocene deposits and vegetation cover, but the trace can be recognized through a series of scarps along the fault system.

In our mapping of the Ragged Mountain fault system we recognize ~37 scarp segments with individual surface rupture lengths of 40.95 m – 1420.26 m and heights that vary from 0.2 m – 1.3 m. The fault trace varies significantly along its trace, however, both in density of surface ruptures and general style. In the northern ~1/2 of the recognizable fault trace, the structure is relatively cryptic (Figure 2.8 inset A and B). In this segment, the fault is recognized only through a series of discontinuous, uphill facing scarps developed on east-facing topographic slopes of Ragged Mountain (Figure 2.8 inset A and B). In this segment, the discontinuous scarps could indicate the ruptures are relatively old because young alluvial fans, talus cones, and glacial deposits cross the fault trace uninterrupted, but it is also possible that slip is simply lower and the structures more cryptic.

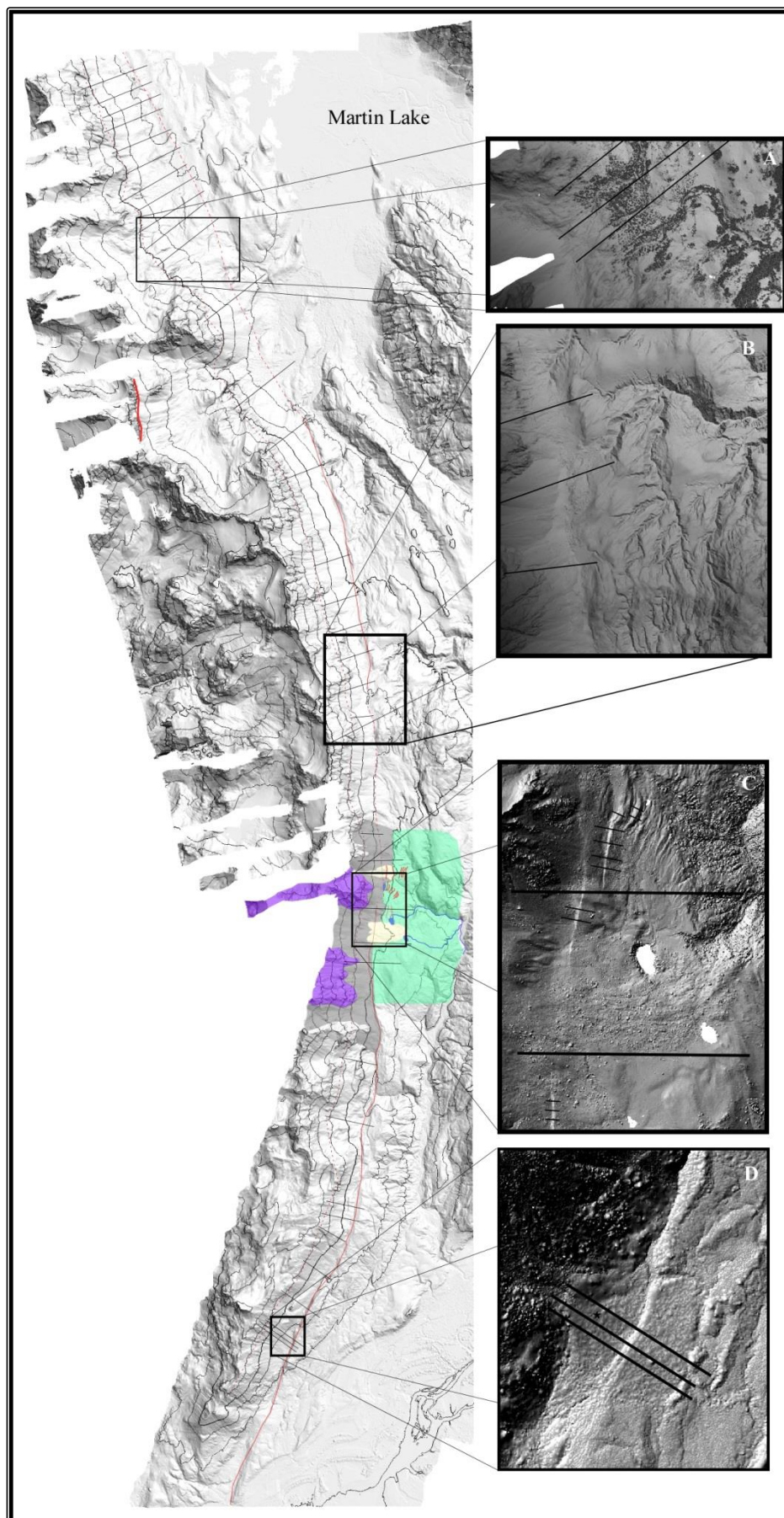


Figure 2.8: Hillside shaded relief derived from the LiDAR data with 20 m contour lines (solid black lines) of the east flank of Ragged Mountain (large image). This figure contains zoom-in shaded relief inset images (A –D) which shows the geomorphology of the surrounding area of the Ragged Mountain area.

In the central segment the fault trace which reaches higher altitude and crosses the topographic divide between the Katalla and Martin Lake Valleys (Figure 2.8 inset B) and in this area becomes a prominent system of fault scarps (Figure 2.8 inset B and C). From just north of the topographic divide to ~1.5 km south of the divide a prominent trough occupies the fault trace. This trough is the geomorphic feature that Tysdal et al. (1976) used to map the fault trace but the most prominent surface rupture is an uphill facing scarps ~100-150m west of the trough. On LiDAR shaded reliefs (Figure 2.8 inset B) the uphill facing scarp is the only feature that is demonstrably a scarp whereas the trough is a relatively irregular, variably snow filled feature with prominent glacial fluted terrain immediately to the east of the trough. These observations suggest that the trough is either a much older fault scarp system, modified by glacial erosion, or is simply an erosional trough developed along fault rocks of the Ragged Mountain system.

To the south of the topographic divide the trough disappears and the east slope of Ragged Mountain abuts against a relatively flat, glacially carved surface with minor modification by post-glacial stream erosion. The uphill facing scarp continues through this segment, ~100m west of the slope break, and its sharp geomorphic expression indicates the rupture must be relatively young. That is, the rupture cuts young talus cones with only local evidence of burial by talus accumulations.

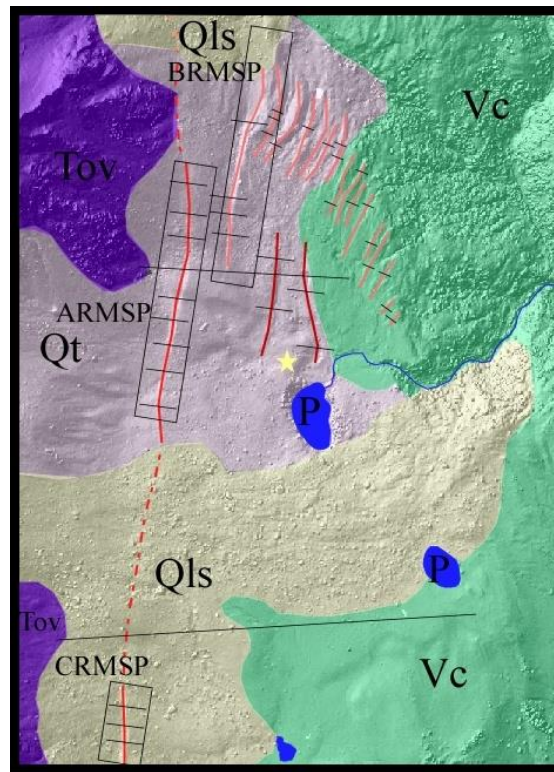


Figure 2.9: Geomorphic map with detail mapping of the trench site. Tov purple color = Paleocene volcanic unit of the Orca Group, Vc olive color = vegetation cover, Qt = Holocene Talus Deposits and Qls = Holocene landslide Deposits, Qal = alluvial fan, blue solid lines = streams, red lines = Ragged Mountain fault red dashed lines where inferred, and small blue polygons = ponds. In set map 1:5000 geomorphic and geology map of the 2005-2006 trench site.

The main scarp segment of the fault, including the trench site - located in the central portion of Ragged Mountain, is characterized by a series of discontinuous, uphill facing scarps visible in the bare ground model. A group of fault scarps at the base of the slope near the trench site (ARMSP, BRMSP, and CRMSP in Fig. 2.8 inset C and 2.9) are important in the context of the fault systems because they lie directly west of trench site that revealed a thrust-fault beneath the scarp shown in Figure 2.10. These scarps consistently lie in the hanging-wall of the thrust, and we analyze this relationship further below.

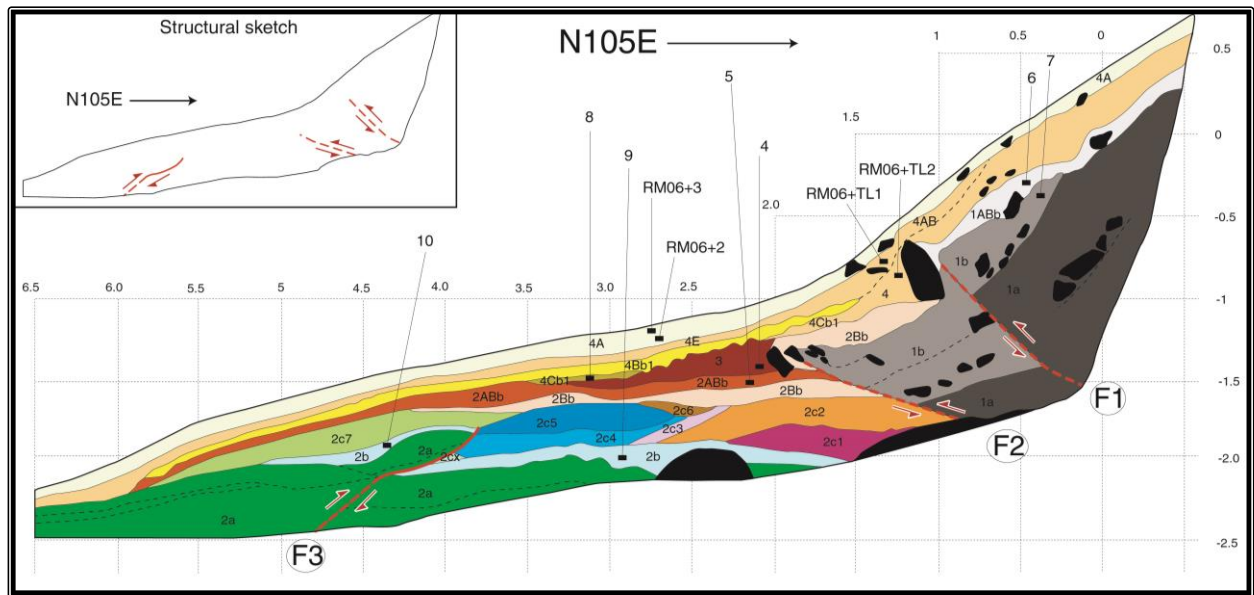


Figure 2.10: 2006 trench log of the thrust fault that confirms the association of surface features that appeared to be characteristic of a thrust scarp.

To the south, the scarp system changes character although some details are lost in the bare ground model due to insufficient removal of low brush that produces a ground texture obscuring details. Nonetheless, a key distinction in the southern 1/3 of the fault trace is the prominent uphill facing scarp observed in the central segment of the fault becomes the dominant fault scarp. That is, although some smaller scarps are present, the fault trace becomes readily traceable as a major, west-side down (uphill facing) scarp that locally ponds drainages to produce small lakes and deflects drainages along the trace. The main scarp in this segment reaches heights of as much as 11.3 m. The general form of the scarp system as well as the increase in scarp height together suggest strongly that fault slip on the Ragged Mountain fault system increases from north to south.

2.6.2 THE QUATERNARY GEOLOGY ALONG THE TRACE OF RAGGED MOUNTAIN

We began our Quaternary mapping in the central part of the Ragged Mountain fault trace, in the vicinity of the 2006 trench site where extensive ground truthing information was available. Several surface features were identified in different display formats of the LiDAR and aerial photographic data. The different views of the LiDAR data are unfiltered and filtered LiDAR DEMs (Figure 2.7A),

unfiltered and filtered slope maps of the LiDAR DEMs (Figure 2.7B), and a 3D contour map with the aerial photos mosaic image draped onto the LiDAR DEM (left image in figure 7C) and red blue 3D contour maps of a LiDAR DEM image (Figure 2.7C). Using these resources led to the geomorphic map of the trench site area (Figure 2.9).

The largest geomorphic feature in the central portion of the mapped area is a major landslide that was derived from Orca Group exposures to the west on Ragged Mountain. This landslide is easily recognized on both aerial photography and LiDAR shaded relief images due to lack of vegetative cover and large blocks carried by the slide. This is one of the youngest geomorphic features in the area based on the lack of vegetative cover and the overlap of the surface ruptures of the Ragged Mountain fault by the slide.

In addition to the landslide, some of the most conspicuous geomorphic features observed through 3D visualization at the trench site are a series of ponds. The origin of these ponds is not certain because although they may represent sag ponds, they may also have been created by damming related to the landslide or even as glacial kettle lakes. The two largest ponds in the central part of the mapped area are spatially associated with the landslide, and likely were formed when the landslide dammed local drainages to form the ponds. However, the largest pond just south of the trench site, is also spatially associated with the thrust scarp in this area and may represent a sag pond that was partially buried by the landslide. Other smaller ponds are present in the northern and southern parts of the mapped area. The origin of these ponds is also uncertain. Ponds were observed at higher elevations on the western side of Ragged Mountain fault that probably formed from high level of snow and rain during the winter season, and ponding occurred when the snow melted during the summer season. In the north, the area is heavily vegetated on the eastern side to the Ragged Mountain fault and ponds in this area are spatially associated with geomorphic features landslides, rock slides, talus slopes, and alluvial fans indicating modern erosion and deposition.

Stream patterns near the trench sites locally show small left-lateral deflections. Near the graben trench site (Figure 2.9) the stream patterns at this pond has a significantly indirect patterns. At the second pond southeast of the graben trench site a second stream also has an indirect patterns. These deflections could be produced by tectonic offsets because they occur along fault scarps, but the absence of shutter ridges or other evidence of strike-slip raises questions on a strike slip interpretation. Thus with no other geomorphic feature observed to verify this left lateral motion interpretation the alternative interpretation is that these two stream patterns deformation from gravity driven processes.

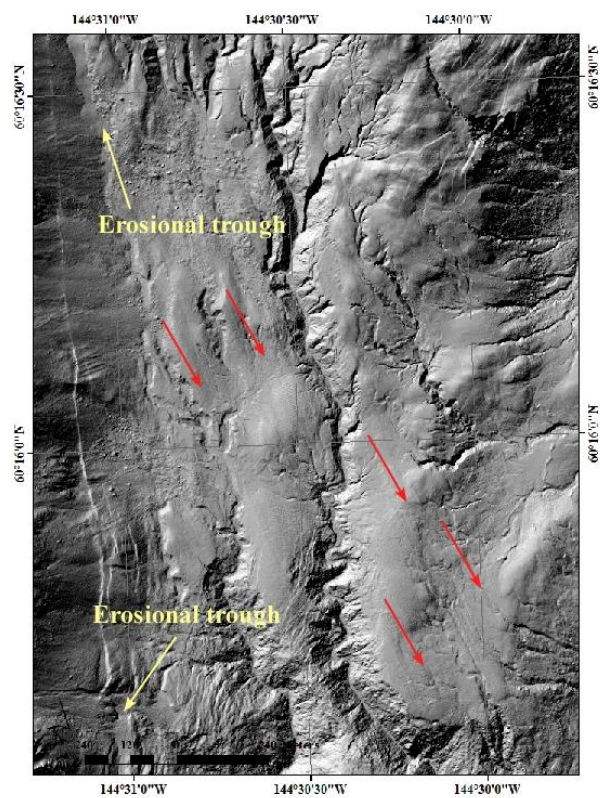
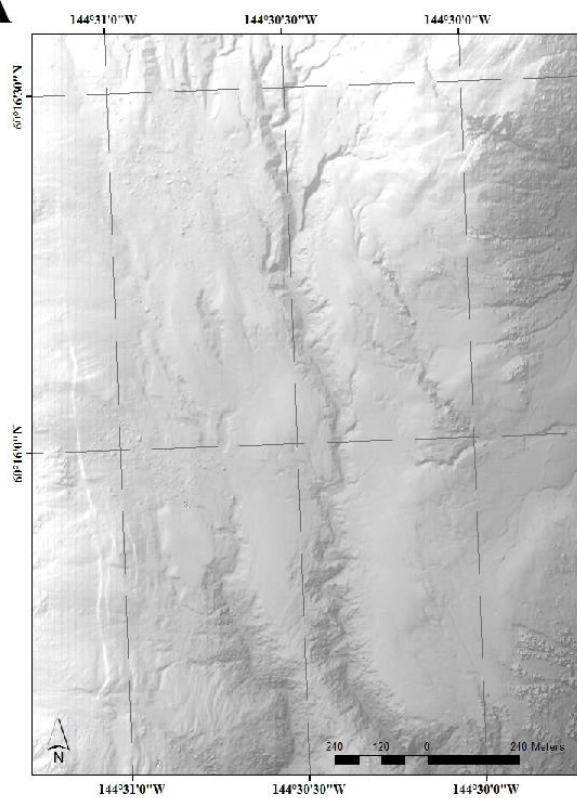
One of the more prominent geomorphic features in Figure 2.9 are a series of alternating small valleys and ridges northwest of the trench site that are interpreted as a series of half-graben fault scarps. The ridges range in strike length from ~ 120 to 180 m and range in height from 0.7 to 6.5m. The local relief is ~ 60 to 200 m across the area of the scarps descending from the main ridge axis along the E-dipping slope of the Ragged Mountain Range into a prominent stream valley to the east (Figures 2.7 and 2.8 and 2.9). Individual scarps produce local ponding and show an asymmetry suggestive of a consistent west-side down displacement. The localization of this scarp array at the headwaters of a small creek suggests strongly that these scarps are primarily gravity driven, extensional scarps above a surficial slope failure.

Another geomorphic surface feature observed in the center part of the study area just north of the trench site are a series of linear, glacially-carved valleys and ridges (Figure 2.11). These linear glacially-carved valleys and ridges are only observed on LiDAR shaded reliefs at higher elevations on uplands surfaces where vegetation cover is minimal. It is possible similar features are present at lower elevation, beneath tree cover but are not well imaged in the bare-ground DEM model. Nonetheless, the limitation of these features to higher altitudes may be real in that erosion and soil-development may have obscured similar features at lower altitude. In any case, these features reveal a glacial history for this region more complex (Figure 2.11) than implied by previous studies (e.g. Fleischer et al., 1999). In the central

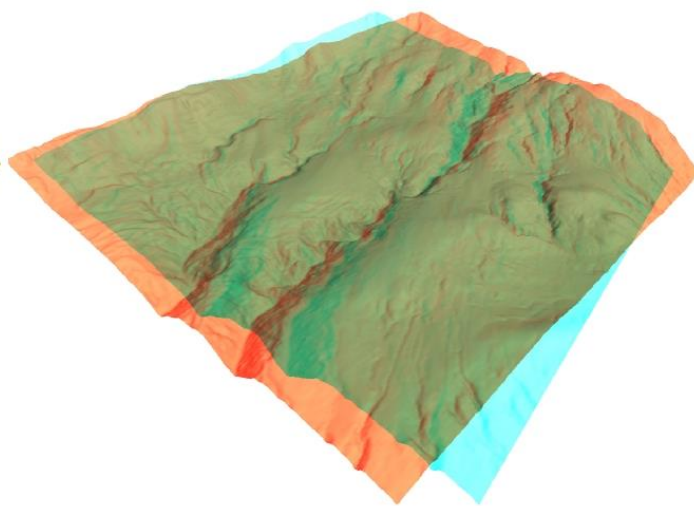
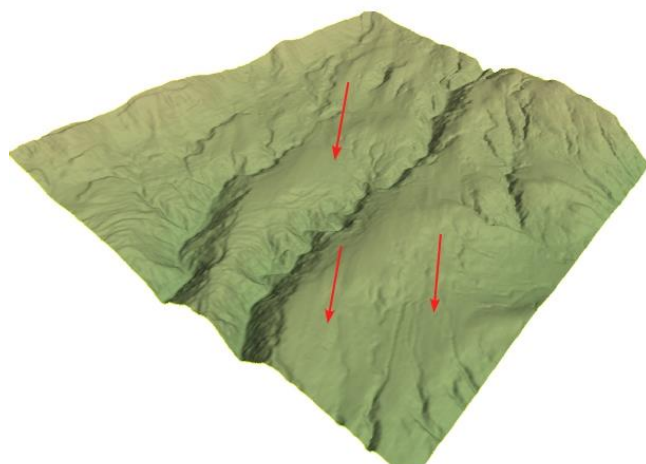
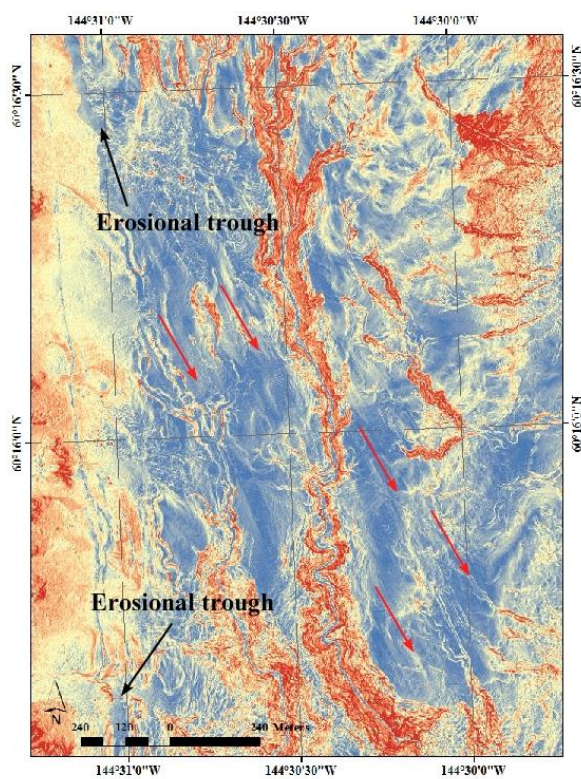
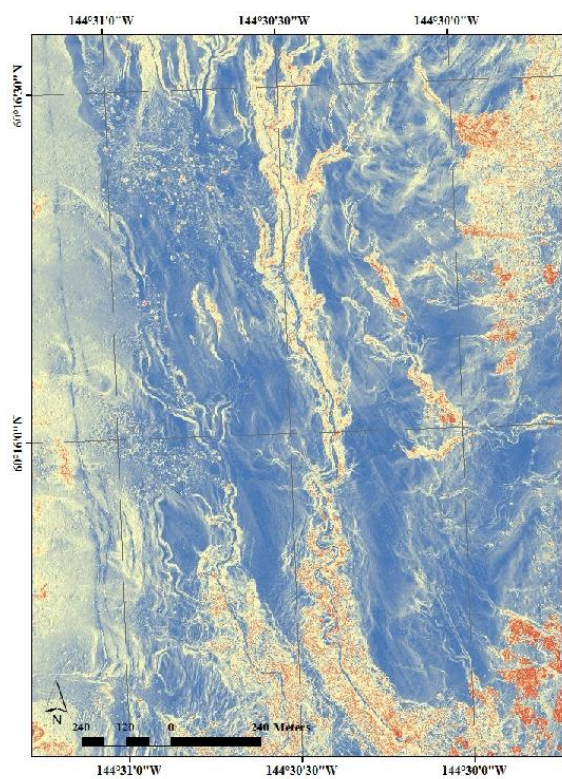
portion of the study area, along the local drainage divide, the terrain shows distinctive fluted topography (Figure 2.11 inset) with the characteristic v-shaped linear ridges that indicate flow in the direction of the opening of the v-shape. Throughout this segment (Figure 2.11 inset) these ridges suggest a flow-pattern of E-NE directed flow off the eastern face of Ragged Mountain, with flow turning toward the north. This flow pattern suggests that the latest ice flow in this region was produced by an ice mass sourced on the east-side of Ragged Mountain (Figure 2.11 inset), probably an ice cap that nearly buried the local mountain crest, and this ice mass flowed toward a topographic low to the north in what is now the Martin Lake Valley. Following the production of this glacial terrain, the area was entrenched by a series of fluvial drainages (Figure 2.11 inset). This pattern of flow (Figure 2.11 inset) is counterintuitive in the context of the glacial chronology for this region that Fleischer et al. (1999) described for this area, where they presented evidence that glaciers to the north, related to the modern Martin River Glacier, filled the Martin Lake Valley and spilled over the divide into the Katalla Valley to the south (Figure 11). Interestingly, evidence for this regional flow pattern is present to the south and east; just east of the trench site, a series of subtle, NNW trending ridges suggest a SSE ice flow and in the headwater of the Katalla Valley a series of small, erosionally modified ridges also suggest SSE directed ice flow (Figure 2.11).

Collectively, these observations suggest the glacial history of this region is more complex than that envisioned by Fleischer et al. (1999). We suggest this pattern indicates a history where an earlier history, presumably during the last glacial maximum, was characterized by ice covering the entire region, flowing southward over the drainage divide between Martin Lake valley and Katalla valley (i.e. as suggested by Fleischer et al. 1999). However, during deglaciation, or during a Holocene glacial advance, the drainage divide area retained an ice cap after ice had retreated from the Martin Lake valley, to form the younger glacial terrain associated with north-directed flow at the drainage divide.

A



B



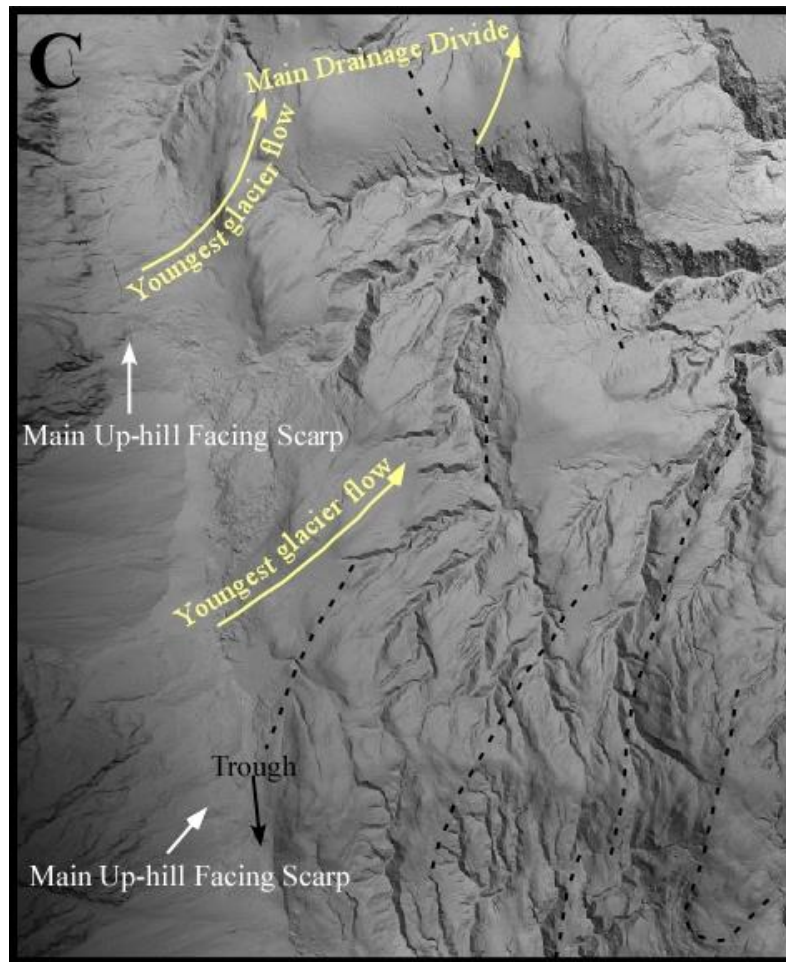


Figure 2.11: 1:5000 scale maps of different views of the LiDAR data unfiltered left side and filtered LiDAR DEMs right side (A), unfiltered (left) and filtered (right) slope spatial analysis of the LiDAR DEMs (B), and two perspective of 3D images right can be viewed with blue red 3D glasses. Red arrows indicate direction of older glacial erosional features. (C) Image shows the younger glacial erosional features and black dotted lines are bedding planes.

Some of the youngest geomorphic features in the area are Holocene talus deposits and landslides at the base of the eastern slope of the Ragged Mountains. The landslides may originate from seismogenic events along the Ragged Mountain fault, the Aleutian megathrust, or both, but the talus is simple slope deposit generated through long-term physical weathering, particularly frost shattering, in the steep terrain to the west in the Ragged Mountains (Figures 2.7 and 2.11). The talus is cut by the scarps, which implies a very young age for the scarps. In other places the slope below the uphill facing scarp is also talus covered, again probably from the most recent deposition.

Another young geomorphic feature cut by the fault is an alluvial fan along the southern flank of the Ragged Mountain, approximately 6.5 km south of the detailed study site (Figure 2.12). This geomorphic feature was revealed by examining the bare-ground LiDAR data, but was completely invisible on the high resolution aerial photography due to the vegetation. This geomorphic surface feature has an area of 154 m^2 and the steep gradient on the upper portion of the alluvial fan is $\sim 16^\circ$ while the lower portion of the alluvial fan is $\sim 11^\circ$. This alluvial fan is cut by the uphill-facing scarp of the Ragged Mountain fault. Any direct evidence of a thrust fault was not observed, but the slip on this segment must be very young to cut the alluvial fan system. A fault scarp segment of $\sim 420 \text{ m}$ length cuts across the fan, and the active fault scarp is from 4 to 9.6 m in height.

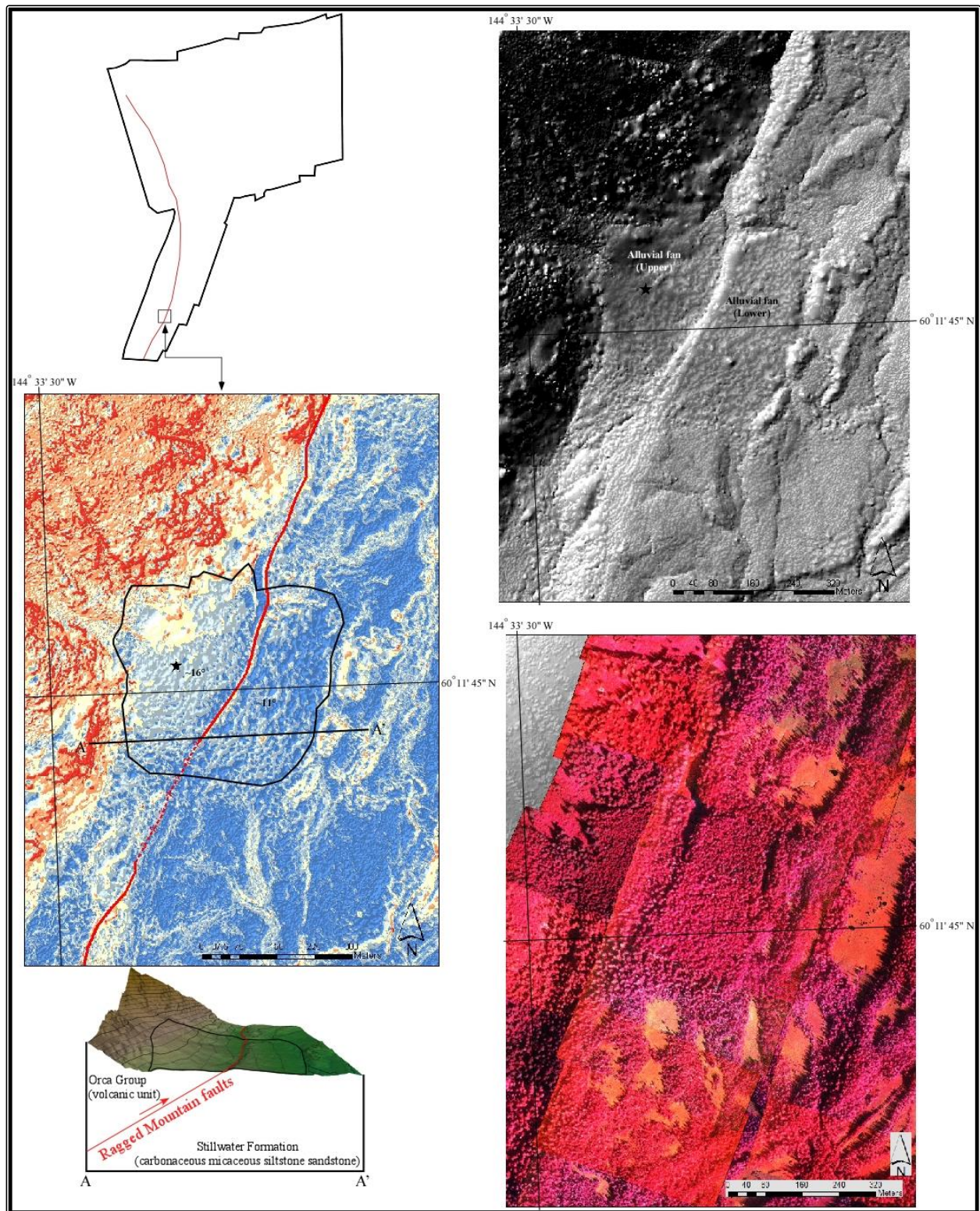


Figure 2.12: Alluvial fan observed along the southeastern flank of the Ragged Mountain Range which is cut by the Ragged Mountain fault. Surface feature has an area of 154 km^2 , a steepness of the slope is $\sim 16^\circ$ on the upper portion of the alluvial fan and $\sim 11^\circ$ on the lower portion, the length of the fan surface is $\sim 420 \text{ m}$ and its width is 458 m . Thrust faulting of the Ragged Mountain fault has resulted in the uplift of the footwall and resulted in faulting of the alluvial fan. The fault scarp segment of $\sim 420 \text{ m}$ length

cuts across the fan, and the active fault scarp measures about 40 to 96 m in height. The constituting materials of the fan are derived from steep slopes of hanging wall. Red to blue image (left center) is an image classification map used to determine the steepness of the slope in the upper and lower portion of the alluvial fan.

2.6.2.2 Slope Map Analyses

In order to highlight or enhance the identification of fault scarps that could not be identified in the different display formats (Figure 2.7), another computer application was used. The “Image Classification” toolbar in Arc GIS10 was applied on the filtered slope map (Figure 2.7B and Figure 2.13). This tool refers to the task of extracting information classes from a multiband raster image. When the raster image is not a multiband raster the program chooses an appropriate display method to render the data, in this case a histogram was computed and adjusted as needed. The resulting raster from image classification can be used to create thematic maps and in this case the thematic map is a five level color ramp display (Figure 2.7, 2.12, 2.13, and 2.14). When a classification is performed clusters of similar features are grouped (in this case the pixel cells of the data set represent different slopes in degrees within the LiDAR data set) into classes by assigning the same symbol/color to each member of the class (Figure 2.13). This application aggregates features into slope classes that enhances data visualization and pattern recognition. For example, this technique allows recognition of the trace of the Ragged Mountain fault where it was obscured in the conventional hillside shaded relief images. The definition of a class range determines which features fall into that class and affects the appearance of the map. By altering the class breaks (the boundary between classes); one can create very different – looking maps. The five level red to blue color ramp scale image was used (Figure 2.7, 2.12, 2.13, and 2.14) to image in particular the scarps spatial distribution and continuity which added in choosing the best part of the fault scarp to survey topographic profiles perpendicular to the trace of the Ragged Mountain fault scarp and assisted in determining the shape of the fault scarps (convex or concave upwards). For example, when mapping at a 1:5000 scale in the alluvial fan area along the southeastern flank of the Ragged Mountain Range (Figure 2.12) the trace of the Ragged Mountain fault scarp is

visible in the shaded relief images where it crosses the alluvial fan, but northeast and southwest of the alluvial fan, the trace of the fault was difficult to follow. However, when using the classification image the trace of the fault was easily observed by the red (very steep slopes) – yellow (moderately steep slopes) color pattern surrounded by a blue (shallow slopes) color pattern (Figure 2.13).

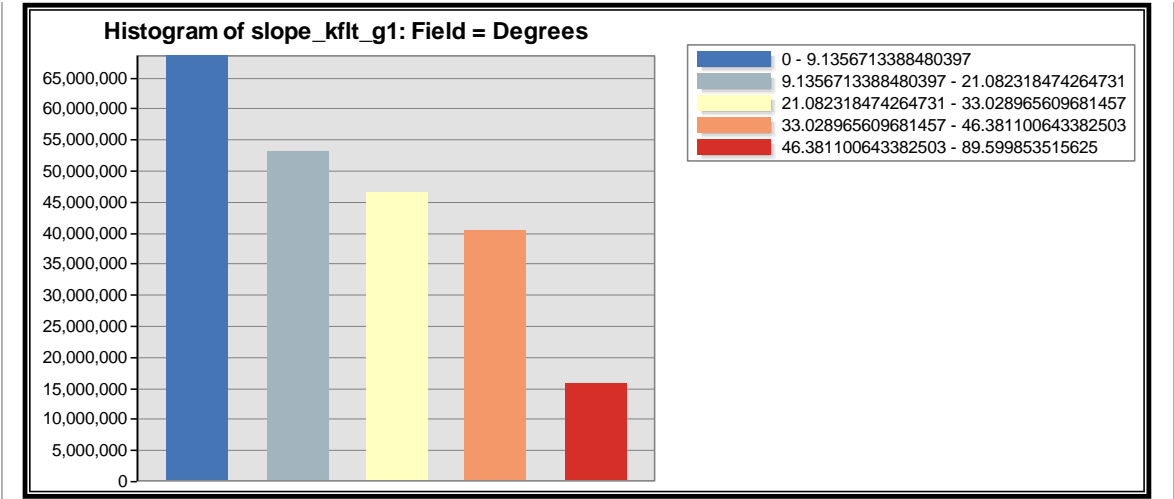


Figure 2.13: Histogram of the filter LiDAR data slope map.

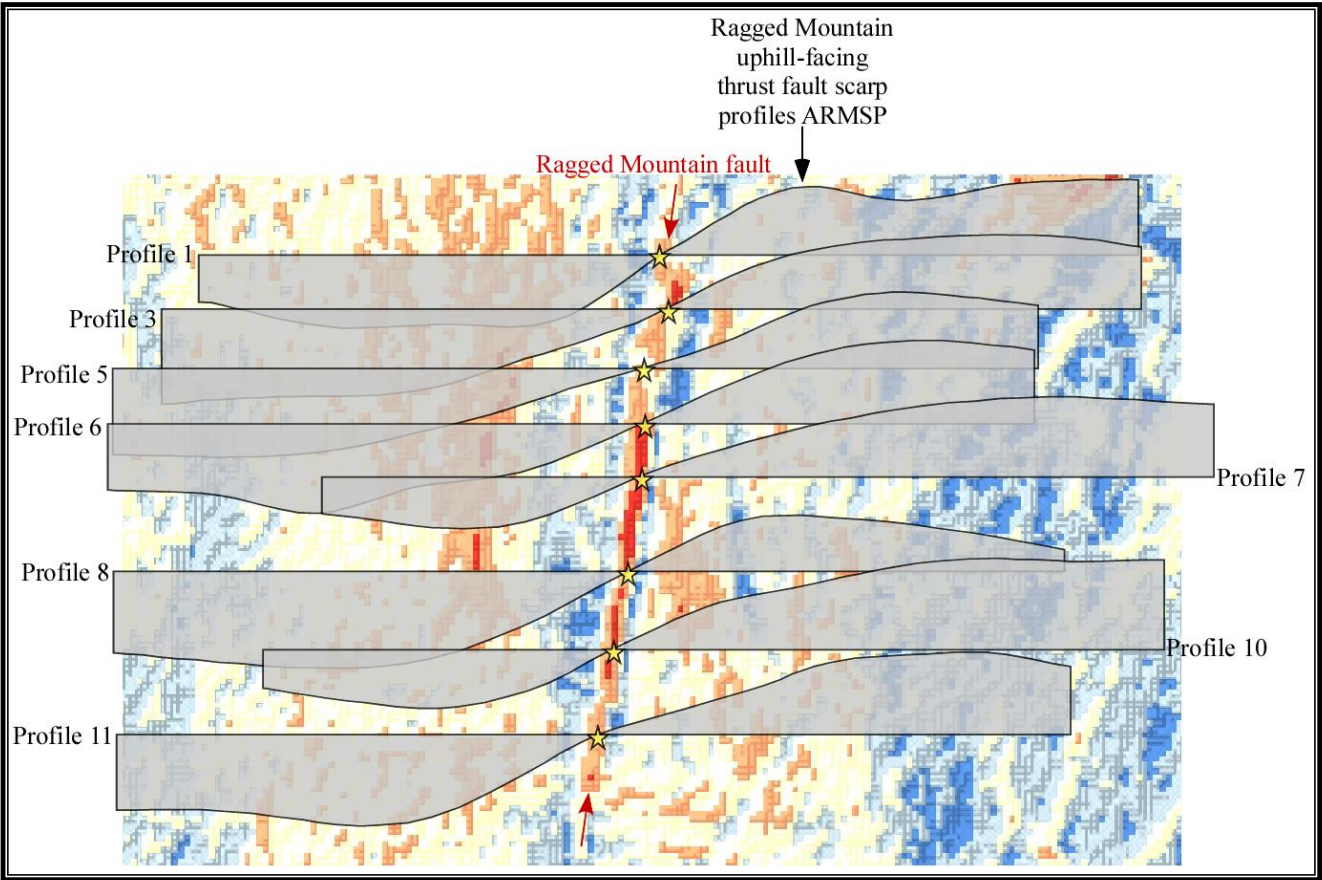


Figure 2.14: Multiple-slice topographic profiling collected along the Ragged Mountain uphill-facing fault scarp near the 2006 trench site. A total of 98 short profiles were collected which range from 6-34 m; only 8 profiles are represented here which are from the ARMSP collection. See figure 2.9 for location of ARMSP topographic profiles. Stars indicate location of where the profiles were collected and red arrows indicate location of the trace of the Ragged Mountain fault. Selection of slices was taken at ~10 m intervals as this is a 1 m DEM. The profile averages for the entire input raster object are shown as the baselines against which the curve-filling is generated plus the slope map in the backdrop. See figure 2.12 for color explanation.

2.6.2.3 Topographic Profile Analyses

Two sets of profile surveys were examined along the Ragged Mountain fault scarp system (Figures 2.14 and 2.15); 1) short profiles which range from 6 – 34 m in length were used to examine the Ragged Mountain uphill-facing fault scarps (Figure 2.14); 2) longer profiles from 700 to 2000 m in length were used to examine the morphology of the entire fault scarp system (Figure 2.15). These long profiles assisted in evaluating the convex up vs. convex down curvature. A third set of short profiles were collected along the east flank of Ragged Mountain to examine secondary and possible flexural slip scarps. The profiles were used to extract the scarp height and slope angle for each identified scarp as well as to determine the shape of the scarps; convex or concave upwards shape (Figures 2.14 and 15). The uncertainty associated with the scarp-height determinations amounts to ± 1 m (1σ).

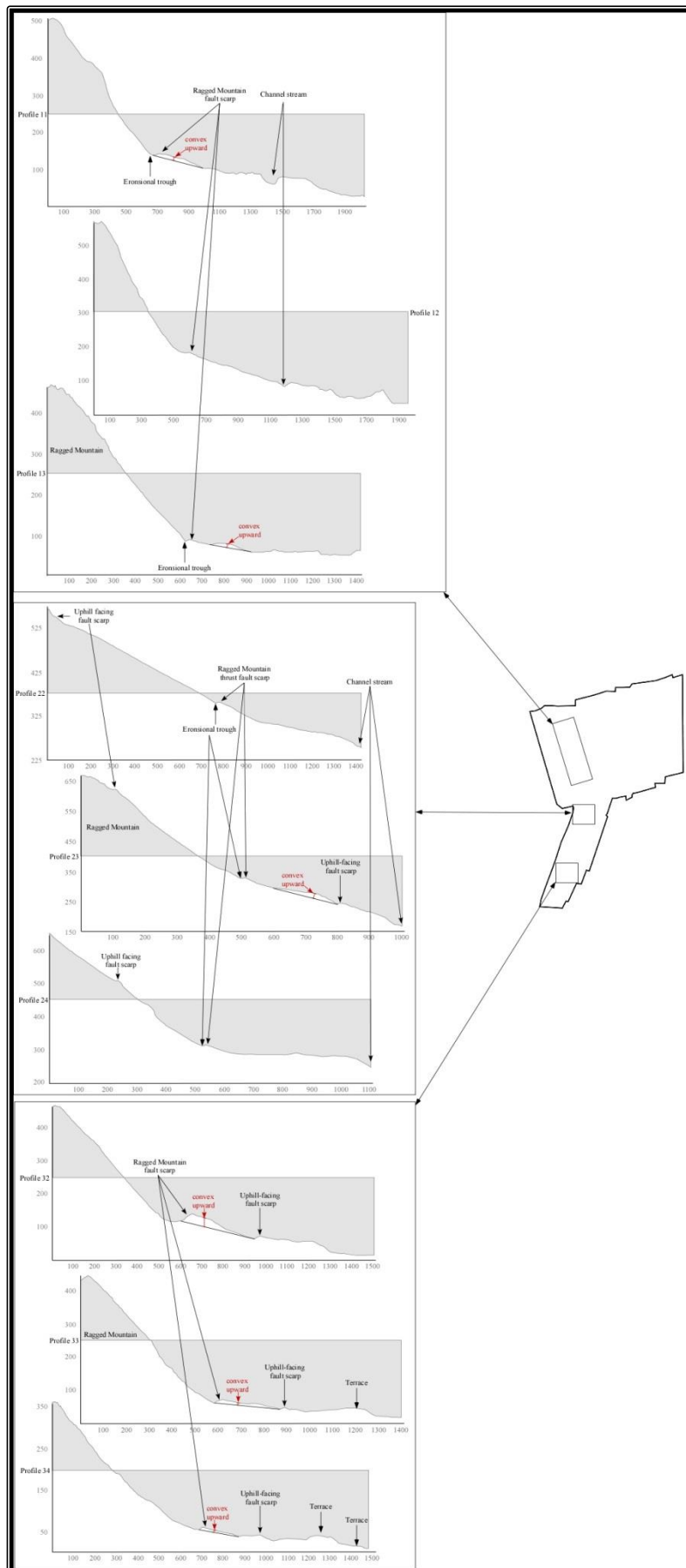


Figure 2.15: Multiple-slice topographic profiling collected along the Ragged Mountain, Ragged Mountain uphill-facing fault scarp and extends past and below the uphill facing scarp. A total of 38 long profiles were collect which range from 700 - 2000 m; only 9 profiles are represented here. Small inset outline of the LiDAR data show location where profiles were collect. The profile averages for the entire input raster object are shown as the baselines against which the curve-filling is generated.

2.6.3 Kinematic Model for the Ragged Mountain fault system

Based on our analysis of the Ragged Mountain fault scarp our working hypothesis is that the uphill facing normal fault-scarps along the Ragged Mountain fault trace represent flexural extension above a buried ramp in a thrust. To evaluate this hypothesis we assume a fault-parallel flow model for the thrusting (Egan et al., 1997, 1999) over a ramp at depth that transfers to a flat fault near the surface. In fault-parallel flow over a ramp (Figure 2.16), the hanging-wall is forced to extend as its material moves through the leading axial plane of the ramp anticline above the ramp (Egan et al., 1997, 1999). This hanging-wall extension is fixed by the geometry, with the main variables shown in Figure 2.16. Here, we assume that the uphill facing scarp records this hanging-wall extension and that the scarp forms along the leading axial plane of the ramp anticline (Figure 2.16). This assumption fixes a geometric relationship between the ramp dip (θ) and the location of the top of the ramp, and allows us to relate the hanging wall extension to the amount of thrust motion through a simple solution using trigonometry. From this geometry we first consider the length of a segment of the hanging wall that moves through the axial surface during a displacement (d). From Figure 2.16 we can calculate the initial length (L_i) through (Figure 2.17):

$$Li = \frac{d \sin(\beta)}{\sin(\gamma)} \quad (1).$$

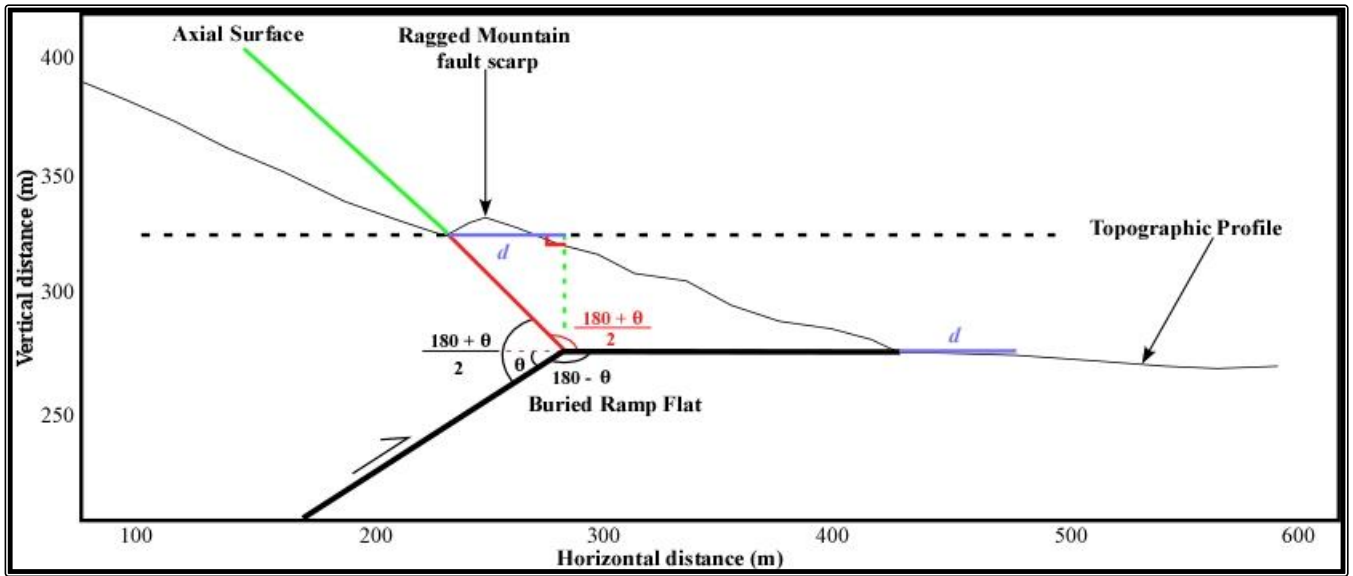


Figure 2.16: General sketch of the fault-parallel flow model of hanging-wall folding and extension. This sketch is used to calculate displacement (d) blue lines. Thick black line represents the buried ramp flat and thin black line represents topographic profile 23. (θ) is the dip angle of the intersection of the thrust fault, and (d) is displacement.

Using the Law of Sine and where γ , τ , β and ϵ represents the angle of the intersection of lines BD and BE of the L_i and the axial surface line element; the angle of the intersection of lines BE and BF the axial surface and displacement line; the angle of the intersection of lines DE and BE the displacement line and the axial surface; and the angle of line BF and EF of displacement and final length (L_f), respectively (Figure 2.17). To determine the above angles the following calculations were used:

$$\gamma = 90 - \frac{\theta}{2} - \alpha \quad (2)$$

$$\tau = 90 + \frac{\theta}{2} \quad (3)$$

$$\beta = 90 - \frac{\theta}{2} \quad (4)$$

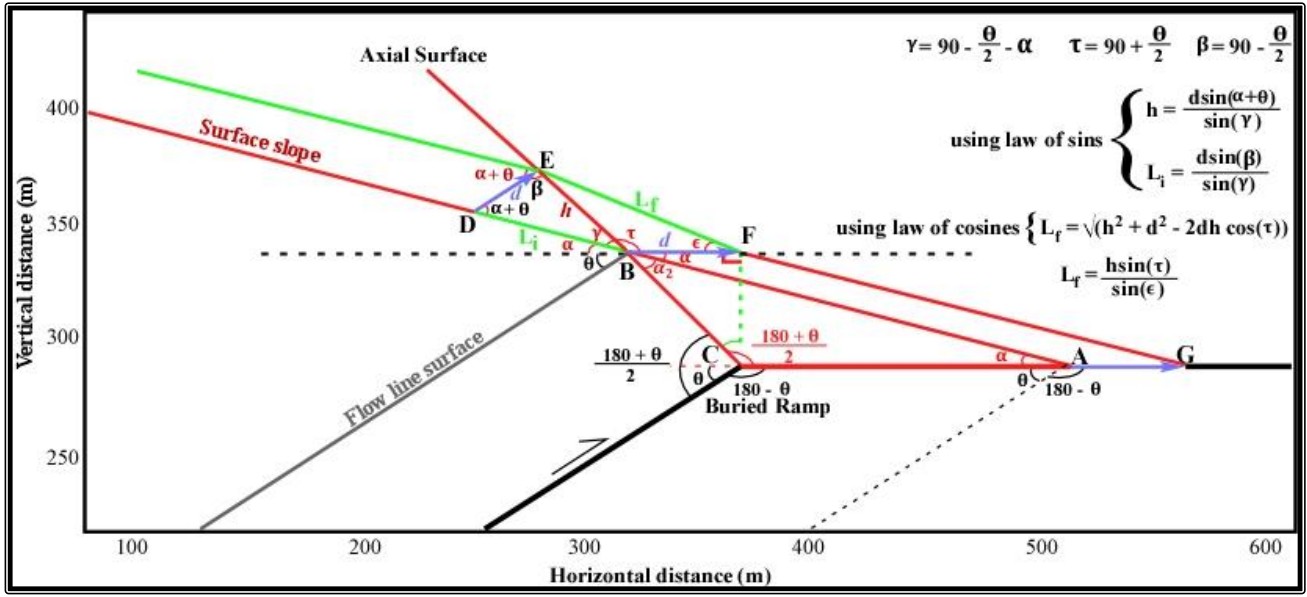


Figure 2.17: Sketch of the fault-parallel flow model of hanging-wall folding and extension. This sketch is used to calculate displacement initial length (L_i) green line BD, and final length (L_f) green line EF. Thick black line represents the buried ramp flat and thin black line represents topographic profile 23. (α) is the angle of the intersection of line AC (the buried ramp flat line) and the line AB, (α_2) is the angle of the intersection of line AB and line BC, (γ) is the angle of the intersection of line BD (the L_i green line) and the line of BE (axial surface green line), (τ) is the angle of the intersection of line BF (d blue line) and line BE (the axial surface green line), (β) is the angle of the intersection of line DE and line BE, and (ϵ) is the angle of the intersection of the L_f .

Similarly, to calculate L_f , we need to know the length h :

$$h = \frac{d \sin(\alpha + \theta)}{\sin(\gamma)} \quad (5)$$

Once h was determined L_f was resolved using a fourth intermediate obtuse triangle created along the L_i triangle (the green axial surface reference line element in Figure 2.17) which is:

$$L_f = \sqrt{h^2 + d^2 - 2dh \cos \tau} \quad (6)$$

After determining the L_i and L_f , the change in length (Δl) and the stretch (S) were calculated:

$$\Delta l = L_f - L_i \quad (7)$$

$$S = \frac{L_f}{L_i} \quad (8)$$

Within the model, each geometric parameter is sensitive to three parameters θ , d , and α , but because α can be measured directly from the DEM only θ and d are independent. Figure 2.18 shows a

graph of Δl per unit d from the model; i.e., essentially Δl is a percentage of the thrust slip component that is transferred to the hanging-wall extension during fault-parallel flow, as a function of ramp dip, with different curves from variations in surface slope α . Note that this percentage is significant, and increases with fault dip and surface slope. We evaluate the significance of this result below.

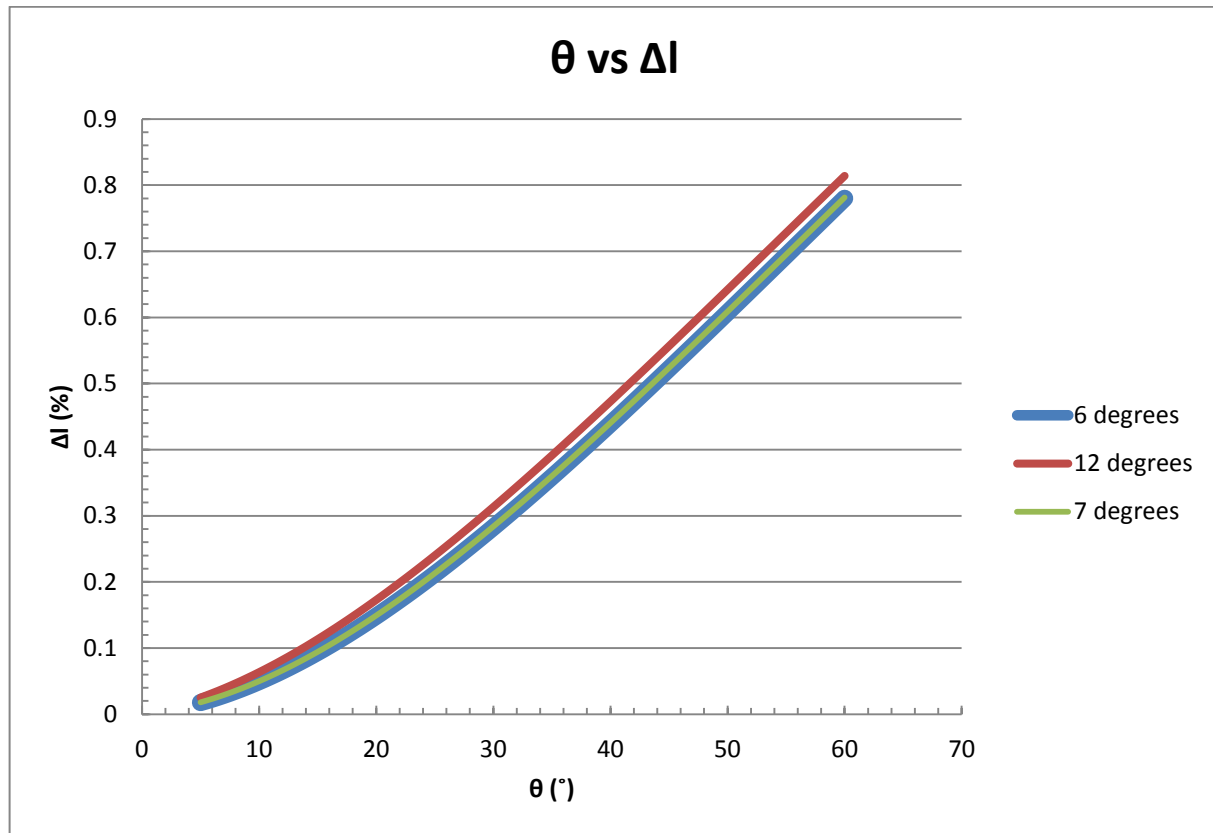


Figure 2.18: Graph showing Δl per unit d from the model; i.e., essentially Δl is a percentage of the thrust slip component that is transferred to hanging-wall extension during fault parallel flow, as a function of ramp dip, with different curves from variations in surface slope α . Note that this percentage is significant, and increases with fault dip (θ) and surface slope (red, green, and blue lines).

Figure 2.19 graphically demonstrates turning the calculation in Figure 2.18 around, for a given amount of extension (Δl) which is determined from the uphill-facing fault scarps, the thrust slip is predicted assuming a given ramp dip. In other words, if we see 5 m of extension in a given profile (in this case profile 11 having a 7° dip) using Figure 2.18 we can determine the inferred thrust displacement for a ramp dip of 45°; the inferred thrust displacement needed to produce the extension (in this example) is ~10m. Figure 2.18 shows that a shallow ramp dip will produce little extension relative to the thrust

component, but as ramp dips get large ($>40^\circ$) the extension approaches the slip on the thrust (Figure 2.18). This deformation is evident in the surface topography illustrated in the numerous topographic profiles collected in this study (Figures 2.14 and 2.15). This deformation is determined based on Figure 2.18 and a constant slip, but the dip changes. The fault could have a low dip to the north and steepen to the south, given an apparent greater extension when the only affect was geometric. This hypothesis is evaluated with the model below.

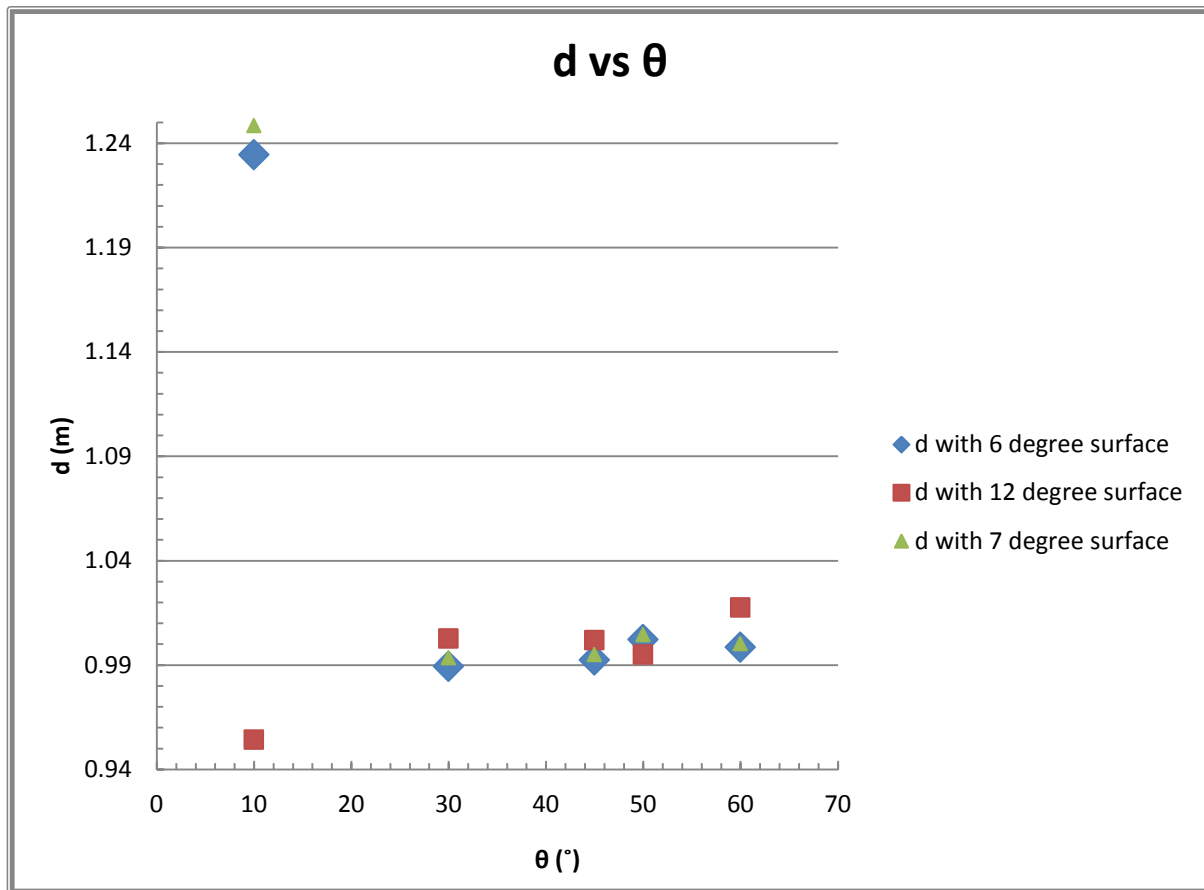


Figure 2.19: Graph showing for a given amount of extension (Δl), determine from the uphill-facing fault scarps, the thrust slip is predicted assuming a ramp dip of 10° , 30° , 45° , 50° , and 60° . When θ increases on the flat ramp the displacement decreases. This means that a shallow flat ramp will facilitate more displacement on the thrust fault (Figure 2.18) and constrains the slip component which transfers to the hanging-wall extension to produce a small extension during fault-parallel flow (Figure 2.18). Plotted on this graph are results of this calculation using profiles 11 (blue), 23 (red) and 34 (green), representing the north, central and south portions of the fault, respectively.

2.7 DISCUSSION

2.7.1 Pros and cons of virtual mapping approaches in this study

In this study the Ragged Mountain fault system is divided into segments that are separated by geomorphic units that make up the eastern flank of Ragged Mountain. 3D virtual geomorphic mapping aided in determining the geologic surface manifestations of active tectonics and inferring the properties of earth materials in the region. The active tectonics in the region primarily produced landforms that record geologically instantaneous events, including earthquakes, landslide, and sackungen. However, the landscape's relief and dense boreal forest make traditional field mapping or aerial photography methods less effective for mapping Quaternary geology features.

The high resolution LiDAR data used in this study offered two distinct advantages over customary approaches. First, the airborne platform provides broad coverage despite rugged topographic relief. Second, the energy from the laser ranging system effectively penetrates the vegetation to provide accurate elevations of the underlying ground surface. These capabilities reveal morphological features on a greater horizontal scale than field mapping and allows for mapping of structures or surface features that were hidden in the aerial photography by vegetation (e.g. as summarized by Hagerud et al., 2003).

Another observation made between the unfiltered and filtered LiDAR data were the large boulders in the open talus slopes of Ragged Mountain. In these areas the bare-earth filtering was unable to filter out the huge boulders which are clearly visible as surface textures on the filtered DEM as well. These surface deposits aided in georeferencing the NCALM photos and mapping geomorphic features. The resulting unfiltered and filtered data sets, hillside shaded relief, slope spatial analysis images, and 3D models allow for improved geological mapping of these areas, and reveal that the drainages were part of a spectacular geomorphic landscape composed of linear glacially-carved valleys and ridges (Figure 2.11), active and inactive landslides, fault scarps, and the footprint of human development (Figure 2.9). While it was known from previous studies (Tysdal et al. 1976, Li et al. 2010, Pavlis and Bruhn 2011, and McCalpin et al. 2011) that the geomorphology of the surface of the Ragged Mountain

area is composed of many uphill facing fault scarps, many indications of structural features associated with these scarps were previously unrecognizable (Figure 2.9).

2.7.2 Slip sense problem for the Ragged Mountain scarp based on geomorphology

Tysdal et al. (1976) argued that 180 m of normal slip, or a slip-rate of ~10 cm/yr, occurred on the Ragged Mountain fault based on scarp morphology and chronology. This slip-rate seems unlikely given that plate convergence rates are half this rate and geodetic studies generally predict contraction (Elliott et al., 2010; Elliott, 2011). This raises significant questions on the normal fault hypothesis, yet the prevalence of extensional scarps in the area, most of them uphill facing, (see above) could be used to support the hypothesis. Thus, the problem needs further discussion. Several observations are relevant. First, the principal feature analyzed by Tysdal et al. (1976) was the trough in the central part of the Ragged Mountain fault rupture system (e.g. Figures 2.3, 2.4, and 2.15). We suggest here that this feature is not relevant to the problem because it is not a simple scarp, but rather is an erosional geomorphic feature with the Ragged Mountain fault ruptures superimposed on the trough. The evidence for this interpretation is the shape of the trough which has a u-shape suggesting a trough carved by glaciers (Figures 2.4, 2.11, and 2.15) presumably during LGM when ice passed over and began to retreat at ~14.4 ka (Chapman et al, 2011; Chapman et al., 2009; Sirkin and Tuthill, 1987; Denton, 1974). In addition, Figure 2.11 clearly shows fluted glacial terrain with landforms that cross-over the geomorphic trough, indicating that no significant motion has occurred on the trough since the formation of these features, and potentially no Holocene motion given this cross-cutting relationship.

Second, the observations, from this study show that the Ragged Mountain fault is a semi-continuous trace as long as ~30 km in length and trends along the eastern flank of Ragged Mountain. The fault trace shows the classic bow-and-arrow rule-shape characteristic of thrust faults, convex toward the transport direction (Figure 2.2, 2.8), whereas the fault is geomorphically at odds with a normal fault hypothesis; i.e., the hanging-wall is elevated and the curvature is opposite that expected for a normal fault. Admittedly, Tysdal et al. (1976) recognized this geomorphic discrepancy and called on a late-

stage, gravitational sliding hypothesis. Nonetheless, if true, the scale of the sliding is large, with little topographic relief to drive it.

Third, regional stresses are favorable for reverse and strike-slip faulting (Ruppert, 2008), not extension. Ruppert (2008) showed that the maximum horizontal stress direction shows varied orientations and high variance values indicating that the stress field is heterogeneous. Nonetheless, recent published work by Bruhn et al. 2012 showed first motion focal mechanisms with P axis in a W-E direction and T axis in an N-S direction; data difficult to reconcile with EW extension along the Ragged Mountain fault.

Fourth, the 2006 trench across the fault shows evidence for a thrust fault at the toe of the Ragged Mountain fault in the central part of the fault trace (Figures 2.20). However, just upslope from this trench site a secondary uphill facing normal fault lies in the hanging-wall of the Ragged Mountain fault suggesting extension (Figures 2.20). A clear thrust trace is limited to only a few hundred meters of the ~30 km trace of the fault which suggests this thrust trace could be some anomalous, local gravitational feature. Unfortunately, most of the fault trace is obscured and covered either by vegetation or talus. Nonetheless, the available data are consistent with a thrust hypothesis, but would require much of the trace to be a blind thrust system during the Holocene.

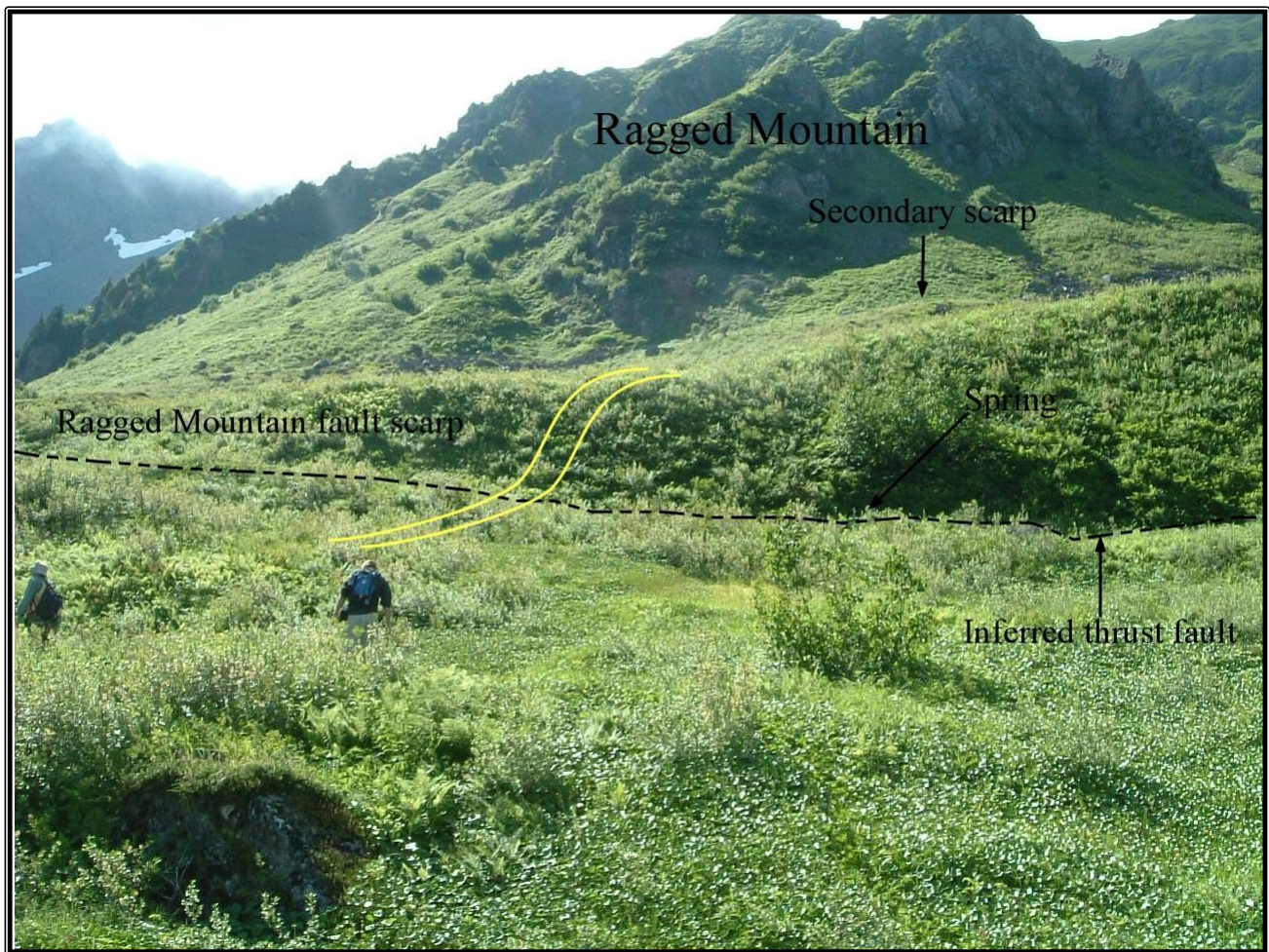


Figure 2.20: Photograph of the 2006 trench across the fault showing evidence for a thrust fault at the toe of the Ragged Mountain fault trace in the central part of the fault trace. However, just upslope from this trench site a secondary uphill-facing normal fault lies in the hanging-wall of the Ragged Mountain fault suggesting extension. Note, a clear thrust trace is limited to only a few hundred meters of the ~30 km trace of the fault which suggests this thrust trace could be some anomalous, local gravitational feature. Unfortunately, most of the fault trace is obscured and covered either by vegetation or talus.

Several observations can be used to evaluate the relative importance of surficial deformation vs. active tectonic processes in the development of the Ragged Mountain fault scarp system. One piece of evidence that suggests deformation in the area is surficial, are post-glacial geomorphic features. When the glaciers receded from the area ~ 10 ka (Fleischer et al., 1999) they had removed any evidence of surface ruptures and created an eroded surface that contains glacially-carved valleys and ridges, and lakes/ponds which were then modified or covered over by vegetation and Holocene deposits of unconsolidated materials such as landslides, talus deposits, loess, alluvial fans, and rock slides. Erosion

and deposition on this post-glacial landscape together have created the modern topography in this area, and through time the surficial mechanisms have gradually shaped the face of the ground surface. It is likely these surficial mechanisms have masked many active tectonic surface features indicative of thrusting through combinations of erosion and deposition. It could be argued that the thrust faults seen in the trench developed via landsliding and what is observed are thrust faults at the toe of this landslide. To add to this argument the thrust faults are only observed at the surface and there is no geophysical or field observation to verify where the faults cut the basement rock.

Although these observations could be used to support a surficial origin for Ragged Mountain system, we suggest that a thrust hypothesis provides the best explanation for the fault system. In addition to the basic regional relationships described above other local details are more consistent with a thrust hypothesis.

Field photos (Figure 2.21) illustrate uphill facing scarps with a convex upward slope above (Figure 2.21a) and below the uphill facing scarp (Figure 2.21b and 2.21c). The convex upward shape was also observed over large areas from elevation profiles in all three areas north, central, and southern portion of the study area (Figure 2.15). For sites where convex upward profiles occur above the uphill facing scarp (e.g. Fig. 2.21a) the slope curvature probably reflects motion on a curved normal fault, dipping toward the slope. In cases with convex upward profiles below the uphill facing scarp, however, the topographic profile would be inconsistent with a normal erosional slope, but characteristics of slopes above a curved thrust fault. We suggest here that these convex upward landforms are the results of a thrust at the toe of slope, but that thrust is largely blind except in the immediate vicinity of the trench site. We suggest further that the extensional, uphill facing scarps are the results of flexure above this largely blind thrust trace.

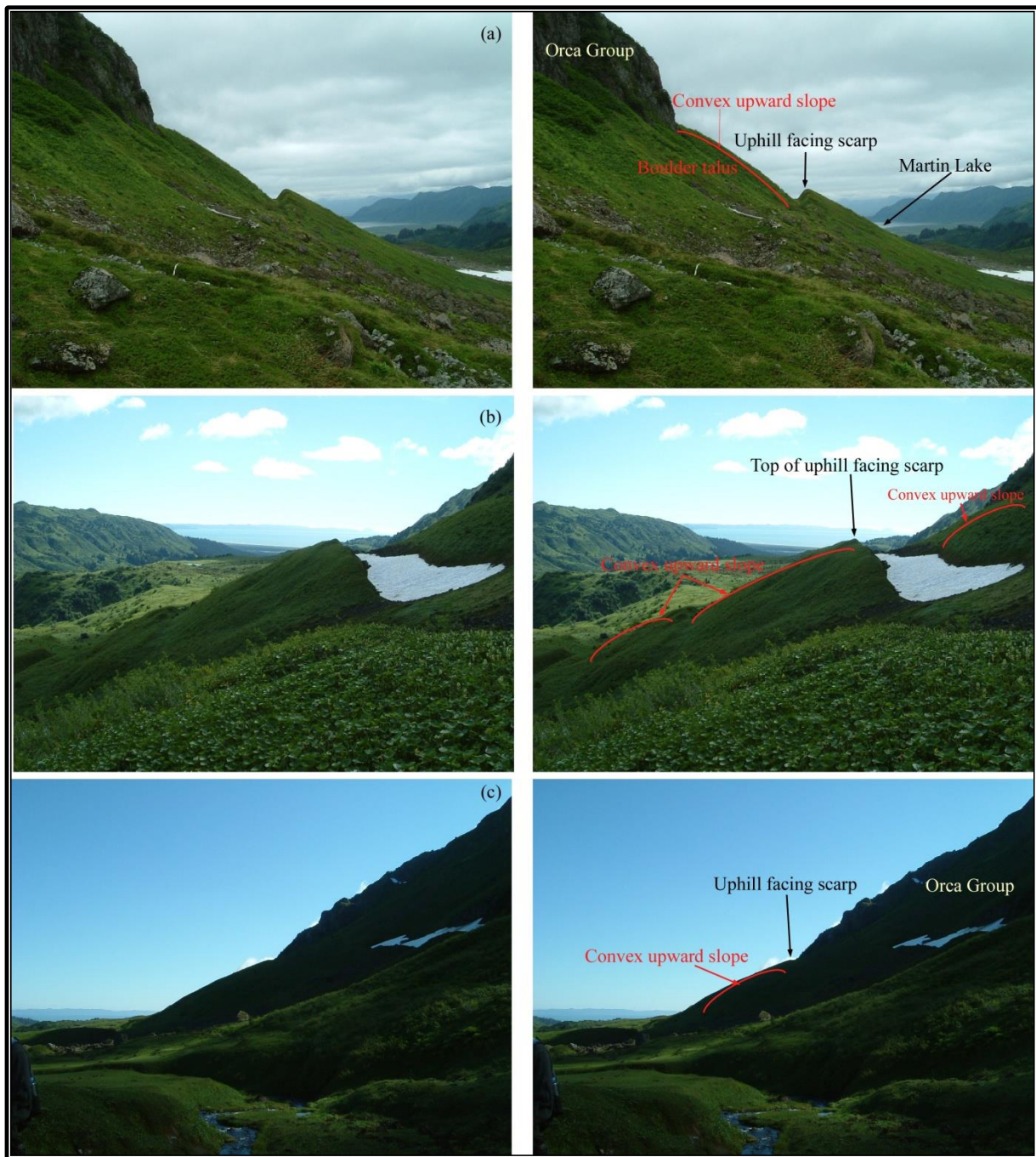


Figure 21: Field photos illustrate uphill facing scarps with a convex upward slope above (Figure 2.21a) and below the uphill facing scarp (Figure 2.21b and 21c). These photos and remotes sensing observations exemplify the evidence that favors the thrust model for this study. This convex upward shape is characteristic of the hanging-wall of the thrust systems due to the warping of materials passing over a thrust ramp, and it will displayed in the area where trenching revealed thrust ruptures. The occurrence of similar topographic profiles over a larger area suggests this geomorphology is typical of the area along the fault system.

To test this hypothesis we developed the model in Figure 2.16 and 2.17 showing the parameters needed to apply to a forward model that illustrates our hypothesis (Figure 2.22). We then follow with a reconstructed model using the topographic profiles to compare with the forward model (Figure 2.23). Move 2D software was used to develop both forward and reconstruction models.

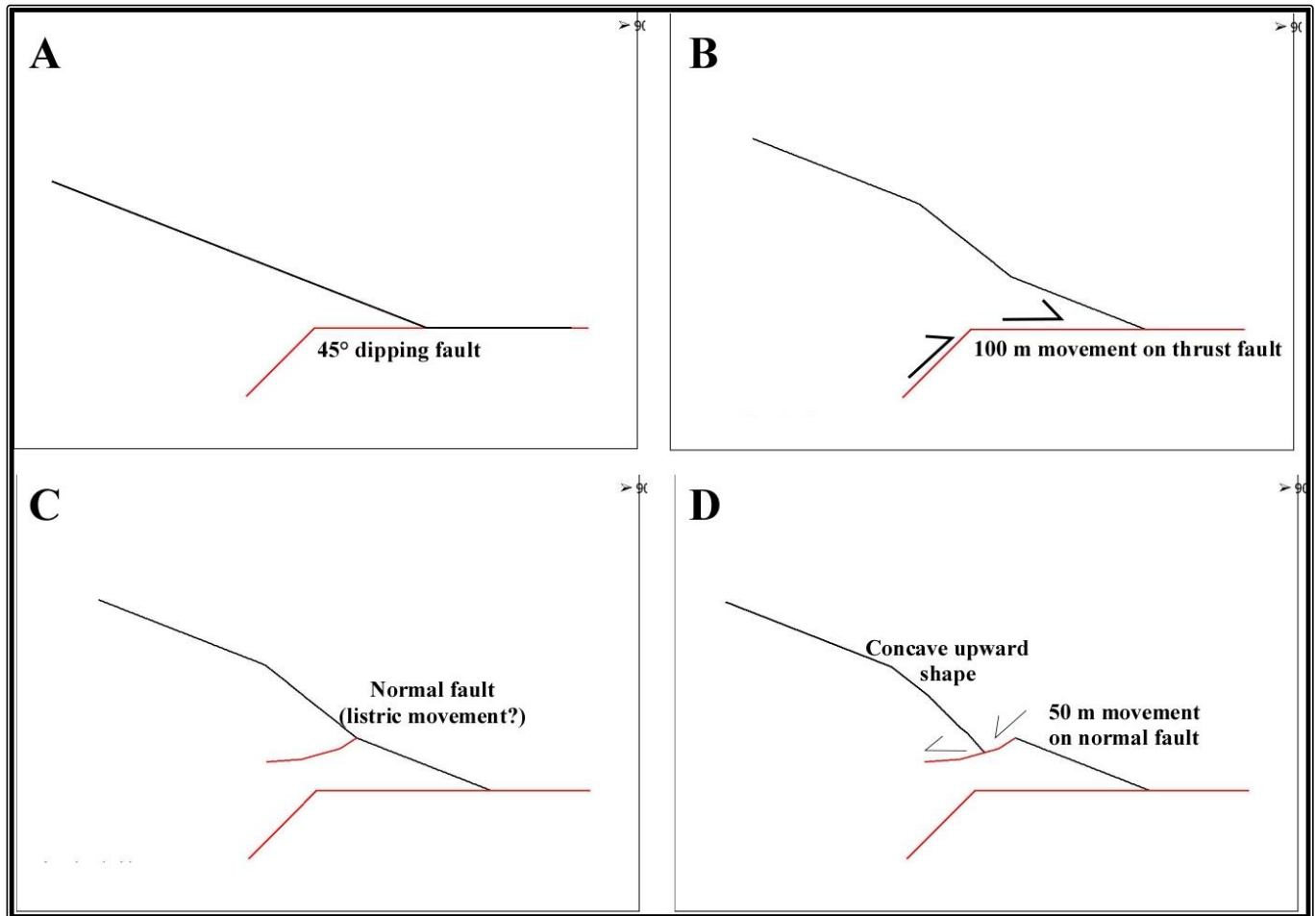


Figure 2.22: Forward model run in Move 2D based on the fault-parallel flow theory developed above. The dimension for the forward model is a 400 x 600 m rectangular model and the dip angle of 45° for the ramp. Note that the exact dimensions are irrelevant in this model other than ramp dip similar to real-world thrust systems. The 2D Move model shows the initial theoretical slope of the Ragged Mountain (A) with the 45° ramp flat, before thrust faulting. (B) Illustrates the geometric parameters of the Ragged Mountain fault just after the hanging-wall fault-motion occurs though faulting with an estimated slip of 100 m. (C) Illustrate the geometric parameters of the normal fault before faulting. The final result of the model is followed by motion of the normal fault that progress toward the foot-wall (D). Note that the model illustrates the development of the uphill facing scarps with a convex upward slope above the uphill facing scarp.

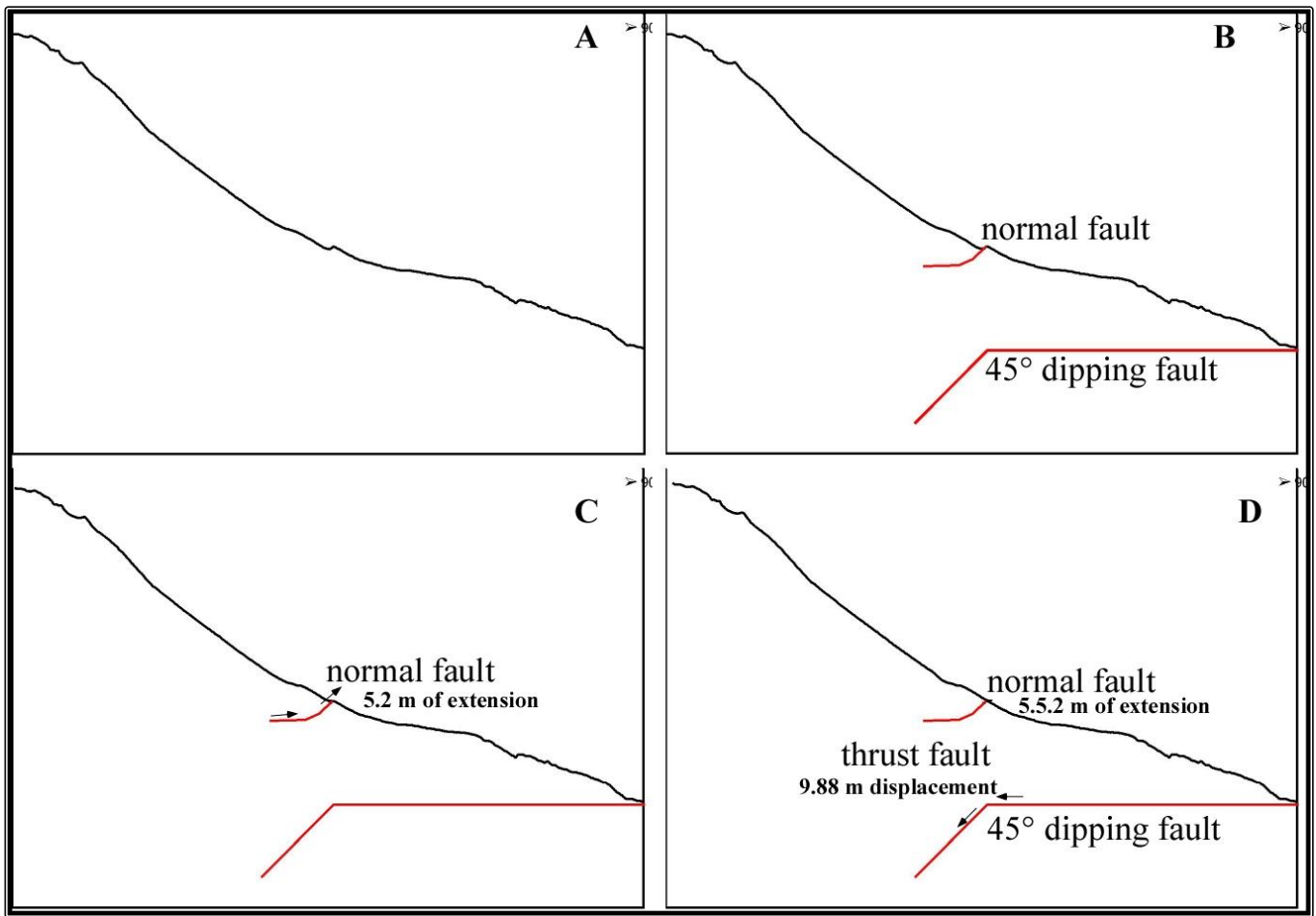


Figure 2.23: Reconstruction model run in Move 2D based on the fault-parallel flow theory developed above. The dimension for the reconstruction model was based on the collected topographic profile data (profile 23) which had a 700 x 1000 m rectangle and an assumed 45° ramp dip. The reconstruction model conducted in 2D Move retains the initial real world topographic profile (23) including the flat ramp and Ragged Mountain fault (A). The reconstruction model is run and the final result of the model shows the undeformed state of faulting of the Ragged Mountain fault (D). Note that deposition is not accounted for in the reconstruction just faulting.

2.7.3 Application of the fault flexure model for the extensional scarp

Forward and reconstruction models were run based on the theory developed above, using 2D Move software on the fault-parallel flow section which agree with the theory (Figure 2.16 and 2.17). The dimension for the forward model had a 400 x 600 m rectangular model and a dip angle of 45° for the ramp (Figure 2.22). Note that the exact dimensions are irrelevant in this model other than ramp dip similar to the real-world thrust systems. The dimension for the reconstruction model was based on the collected topographic profile data (profile 23 in Figure 2.23) which had a 700 x 1005 m rectangle and an

assumed 45° dip (Figure 2.23). Based on the forward and reconstruction models we calculated both displacement and slip amounts under different assumptions on the thrust geometry; five possible fault dips were used: a low dip of 10°, 30°, 45°, 50° dip, and a steep dip of 60°. The analysis presented here suggests the final structural geometry is sensitive to the ramp dip θ and less sensitive to surface slope.

The forward model conducted in 2D Move shows the initial theoretical slope of Ragged Mountain (Figure 2.22A) with the 45° ramp dip and a surface slope of 29° before faulting. Figure 2.22B then illustrates the geometric parameters of the Ragged Mountain fault after thrust fault motion and just before the normal fault-motion. The final phase of the model removes the extensional component (calculated from (7)) assuming a listric fault (Figure 2.22D). Note that the model illustrates the development of the uphill facing scarps with a convex upward slope above the uphill facing scarp. The reconstruction model (Figure 2.23) retains the initial real world topographic profile (23) with an assumed 45° dip of the flat ramp and Ragged Mountain fault (Figure 2.23A). The reconstruction first restores the extension through 5.2 m of slip on a curved normal fault, and then restores 9.88 m of thrusting using the theory. Note that deposition is not accounted for in the reconstruction just faulting and this model assumes all of the extension is transferred as slip to the uphill facing scarp. The resultant restoration provides a reasonable restoration of a uniform slope, prior to slip on the thrust. In the case of this profile, the thrust can be assumed to be coincident with the thrust recognized in the trench. Elsewhere in the study area, however, the thrust motion presumably was blind; a conclusion that is reasonable to the north where the uphill facing scarps are small, but harder to rationalize to the south where the scarps are large. The slip increase from north to south, based on Figure 2.19 the slip is constant, but the dip changes; that is, the fault could have a low dip (10°) to the north and steepen to the south (60°), given an apparently greater extension when the only affect is geometric.

2.7.4 Fault Slip Rate on Ragged Mountain fault

One outcome of the modeling results in Figure 2.23 is that the reconstruction allows an estimate of the Holocene net slip on the thrust, which cannot be estimated from the trench itself. For an assumed ramp dip of 45 degrees, the predicted thrust displacement is (9.2m) to restore the uphill facing scarp. This estimate is probably a maximum because steeper ramp dips would predict lesser thrust displacements and lower ramp dips would predict large thrust offsets that should not be blind along large sections of the fault. Based on this assumption, we can estimate slip rates using two Optically Stimulated Luminescence (OSL) ages from the trench, which range from $2.01 \text{ ka} \pm 0.27 \text{ ka}$ and $2.84 \text{ ka} \pm 0.41 \text{ ka}$; from the 2006 STEEP trench site data collection (McCalpin et al. unpublished work). This suggests a maximum slip rate of $\sim 49 \text{ mm/yr}$ based on a -ramp dip of 45° dip, with lower rates for steeper ramp dips. This result is intriguing because this is sufficient slip to account for all of the $\sim 45\text{-}49 \text{ mm/yr}$ of convergence in the region recognized in the geodetic studies of Elliott et al., (2010) and Elliott (2011).

2.8 CONCLUSION

The topography of Ragged Mountain area is an ideal natural laboratory for the development of high resolution aerial photography techniques and high resolution LiDAR data (1 m) of this quality for 1) understanding the active faulting associated with active tectonics and 2) identification of geomorphic spatial patterns and applications. This study demonstrates that these types of data sets are good means to collect data such as multiple fault scarp profiles which were surveyed throughout the study area and assisted in the selection of several sites which became the focus of the study. High resolution LiDAR topography, high resolution photographs, and working at a 1:5000 scale data frame are ideal for detailed 3D virtual structural and geomorphic mapping. Also the high resolution 1 m LiDAR DEMs and photograph appears close to that needed to capture all of the stream channels in the Ragged Mountain area.

Virtual geomorphic mapping of the 2006 trench site and the surrounding area including focus sites provides a fault scarp inventory and a refined analysis of geomorphic data collected in the area and a collection of elevation profiles. All of this provides an enhanced appreciation of the glacial processes along with the geomorphology and structure. The data sets used in this study assisted in the development and testing of the fault-parallel flow model to evaluate the extensional vs thrust hypothesis for the Ragged Mountain fault system. Restorations using the fault-parallel flow model replicated the morphology of the Ragged Mountain fault scarps which, together with regional observations, suggests strongly that the Ragged Mountain fault system is a thrust fault and the uphill facing, extensional scarps are related to extension above a fault ramp at depth. The absence of conspicuous thrust scarps aside from the immediate area of the 2006 trench remains a problem, but we interpret this observation as indicating the thrust is primarily blind. Based on the theory, the dominance of blind thrusting could indicate the thrust ramp is relatively steep over most of the area, but more work is needed to test this hypothesis. Offsets and slip-rates were determined from the data sets, model developed, and ages from the 2006 paleoseismologic trench site and this calculation suggests the Ragged Mountain fault system could be taking up a large fraction of the convergence in the region. The application of the fault-parallel model indicates that the slip-rates vary by up to an order of magnitude from the north to the central to the south and that the fault displacement is either not uniform through time or convergence is transferred to other structures along the fault.

2.9 Summary

The research conducted 3D virtual geomorphic mapping by employing LiDAR data and high resolution aerial photography by means of draping the photography over the DEM model. The fault-parallel flow model was completed for the Ragged Mountain fault, using previously collected ground trench data by the STEEP 2006 reconnaissance team and LiDAR data to estimate displacement and slip

rates. These results are valuable in understanding the Holocene paleoseismic history of the region, establishing a geomorphic foundation that can be used to compare it to other regions with similar tectonic and geomorphic environments such as the Kamchatka Peninsula Russia.

References Cited

- ArcGIS 10., 1995-2010. Is a Scalable framework software program for implementing Geographic Information System data for single users or many users on desktops, in servers, over the Web, and in the field. ArcGIS is an integrated family of GIS software products for building a complete GIS. ESRI.
- Arrowsmith, J.R., Rhodes, D.D., and Pollard, D.D., 1998. Morphologic dating of scarps formed by repeated slip events along the San Andreas Fault, Carrizo Plain, California: *Journal of Geophysical Research*. v. 103, 10,141-10,160.
- Andrews, D.J., and Bucknam, R.C., 1987. Fitting degradation of shoreline scarps by a nonlinear diffusion model: *Journal of Geophysical Research*. v. 92. no. B12, 12,857-12,867.
- Ayarbe, J.P., Phillips, F.M., Harrison, J.B.J., Elmore, D. and Sharma, P., 1998. Application of cosmogenic nuclides to fault-scarp chronology: Preliminary results from the Socorro Canyon Fault. In: Harrison, J.B.J. (Ed.), *Soil, Water, and Earthquakes around Socorro, New Mexico: Guidebook for the Rocky Mountain Cell of the Friends of the Pleistocene 1998 Field Conference*, 10-13 September 1998, New Mexico Tech, Socorro, p.12.
- Avouac, J., 1993. Analysis of scarp profiles—evaluation of errors in morphologic dating: *Journal of Geophysical Research*. v. 98. no. B4, 6,745-6,754.
- Baran, R., Guest, B., and Friedrich M. A., 2010. High-resolution spatial rupture pattern of a multiphase flower structure, Rex Hill, Nevada: New insights on scarp evolution in complex topography based on 3-D laser scanning. *Geological Society of America Bulletin*, 897-914.
- Belousov, A., Voight, B., & Belousova, M., 2007. Directed blasts and blast-generated pyroclastic density currents: a comparison of the Bezymianny 1956, Mount St Helens 1980, and Soufrière Hills, Montserrat 1997 eruptions and deposits: *Bull Volcanol*. doi: 10.1007/s00445-006-0109-y.
- Black, B. D., Lund, W., Schwartz, D. P., Gill, H. E., & Mayes, B. H., 2003. Paleoseismic investigation of the Salt Lake City segment of the Wasatch fault zone at the South Fork Dry

- Creek and Dry Gulch sites, Salt Lake County, Utah Geological Survey Special Study 92. Geological Survey Special Study 92, p.22.
- Bruhn, L. R., Palvis, L. T., Plafker, G., & Serpa, L. (2004, July/August). Deformation during terrane accretion in the Saint Elias orogen, Alaska. *GSA Bulletin*, 116 (7/8), 771-787.
- Bruhn, L. R., and Haeussler, J.P. (2006). Deformation driven by subduction and microplate collision: Geodynamics of Cook Inlet basin, Alaska. *GSA Bulletin*, 118, 289-303.
- Bucknam, R. C., and R .E. Anderson, 1979. Estimation of fault-scarp ages from a scarp-height-slope angle relationship: *Geology*. v. 7, 11-14.
- Camelbeeck, T., Matin, H., Vanneste, K., Verbeeck, K., and Meghraoui, M., 2001. Morphometric analysis of active normal faulting in slow- deformation area: examples in the Lower Rhine Embayment. *Netherlands Journal of Geosciences/Geologie en Mijnbouw*, 95-107.
- Carter, W., Shrestha, R., Tuell, G., Bloomquist, D., & Sartori, M. (2001, November 13). Airborne Laser Swath Mapping Shines New Light on Earth's Topography. *Eos, transactions, American Geophysical Union*, 82(46), 549-555.
- Carver, G., A, and McCalpin, J., P., 1996. Paleoseismology of compressional tectonic environments. In "Paleoseismology." (J. McCalpin, P., Ed.). International Geophysics Series. Academic Press, SanDiego. pp. 183-270.
- Caskey, S.J., 1995. Geometric relations of dip slip to a faulted ground surface: new nomograms for estimating components of fault displacement: *J. Struct. Geol.* 17, 1197–1202.
- Cervera, S. N., 2006. The Quaternary deformational history of the East Potrillo Mountains, Dona Ana County, New Mexico. M.S. Thesis, The University of Texas at El Paso.
- Chang, W.L., 1998. Earthquake hazards on the Wasatch fault—tectonically induced flooding and stress triggering of earthquake. M.S. Thesis, University of Utah, p.123.

- Chang, W.L., and Smith, R.B., 2002. Integrated seismic–hazard analysis of the Wasatch Front, Utah: Bulletin of the Seismological Society of America. v. 92. no. 5, 1904-1922.
- Chapman, J. D., Pavlis, T. L., Bruhn, R. L., Worthington, L. L., Gulick, S. P., & Berger, A. L. (2012). Structural Relationships in the Eastern Syntaxis of the St. Elias Orogen, Alaska. *Geosphere*, 105-126
- Chapman, J. P. (2008). Neotectonics of the Yakutat collision: Changes in deformation. *American Geoloical Union: Geophysical Monograph Series*, 179, 350.
- Chapman, J. P. (2008). Structural Relationships and crustal deformation in the Saint Elias Orogen, Alaska. [MS thesis]. University of Texas at El Paso, 97 p.
- Chen, Y.-G., Lai, K.-Y., Lee, Y.-H., Suppe, J., Chen, W.-S., Lin, Y.-N. N., et al. (2007). Coseismic fold scarps and their kinematic behavior in the 1999 Chi-Chi earthquake Taiwan. *Journal of Geophysical Research*, B03S02.
- Chiang, S., Chang, K., Mondini, A. C., Tsai, B., Chen, C. (2011). Simulation of event-based landslides and debris flows at watershed level. *Geomorphology*, v. 138. p. 306-318.
doi:10.1016/j.geomorph.2011.09.016.
- Christeson, G. L., Gulick, S. P.S., van Avendon, H. J. A., Worthington, L. L., Reece, R. S., and Pavlis, T. L. (2010). The Yakutat terrane: Dramatic change in crustal thickness across the Transition fault, Alaska. *Geology*. v. 38. p. 895-898. doi: 10.1130/G31170.1.
- Cluff, L.S., Brogan, G.E., and Glass, C.E., 1973. Wasatch fault – southern portion, earthquake fault investigation and evaluation—a guide to land use planning for Utah Geological & Mineral Survey: Oakland, California, Woodward-Lundgren & Associates, Project G- 12069A, 56.
- Culling, W.E.H., 1963. Soil creep and the development of hillside slopes: *Journal of Geology*. v. 71, 127-161.

- DeCelles, P. G. (2004). Late Jurassic to Eocene Evolution of the Cordilleran Thrust Belt and Foreland Basin System, Western USA. *American Journal of Science*, 105-168.
- DeMets, C.R., Gordon, R.G., Argus, D.F., Stein, S., 1990. Current plate motions: Geophys. J. Int. 101, 425–478.
- Doser, D. I., Wiest, K. R., Sauber, J.M., (2007). Seismicity of the Bering Glacier region and its relation to tectonic and glacial processes: Tectonophysics, v. 439, p. 119-127, doi:10.1016/j.tecto.2007.04.005.
- DuRoss, C. B., and Bruhn, R. L., 2004. Active Tectonics of the Nephi Segment, Wasatch Fault, Utah: Basin and Range Province Seismic Hazards Summit.
- Eichelberger, J. C. & Izbekov, P. E., 2000. Eruption of andesite triggered by dyke injection; contrasting cases at Karymsky Volcano, Kamchatka and Mt Katmai, Alaska: Philosophical Transactions of the Royal Society of London. Series A 358, 1465–1485.
- Erlich, E.N., 1973. Modern Structure and Quaternary Volcanism of the Western Pacific Rim: Nauka, Novosibirsk. p. 243 (in Russian).
- Elliott, J., Freymueller, J.T., and Larsen, C.F., 2007, Crustal deformation and strain localization in the Saint Elias orogen, Alaska observed by GPS: San Francisco, American Geophysical Union, Fall Meeting 2007, Abstract G14A-02.
- Elliott, L. J., Larsen, F. C., Freymueller, T. J., and Motyka, J. R. (2010), Tectonic block motion and glacial isostatic adjustment in southeast Alaska and adjacent Canada constrained by GPS measurements. *Journal of Geophysical Research*, B09407.
- Erlikh, E.N., Melekestsev, I.V., Shantser, A.E., 1974. Neotectonics. History of Relief Development in Siberia and Far East. Kamchatka, the Kuril and Komandor Islands: Nauka, Moscow, p. 345–368 (in Russian).
- ESRI. (1999-2006). ESRI ArcGIS ArcMap ArcCatalog.

- Exploration, M. V., 2009. Move 2D 3D 4D. Midland Valley Exploration Move 2D 3D 4D.
- Fedotov, S. A., and P. I. Tokarev, 1974. Earthquakes, characteristics of the upper mantle under Kamchatka, and their connection with volcanism (according to data collected up to 1971): Bulletin Volcanologique. v. 37, 245–257.
- Fedotov, S.A., Masurenkov, Yu.P. (Eds.), 1991. Active volcanoes of Kamchatka: Nauka, Moscow. v. 1, p.302. v. 2, p. 415 (in Russian).
- Fedorov, P.I., Shapiro, M.N., 1998. Neogene volcanics of the Kamchatka isthmus and geodynamics of the Aleutian–Kamchatka junction: Geotectonics. v. 32, 122–137.
- Friedrich, A.M., Wernicke, B.P., Niemi, N.A., Bennett, R.A., and Davis, J.L., 2003. Comparison of geodetic and geologic data from the Wasatch region, Utah, and implications for the spectral character of Earth deformation at periods of 10 to 10 million years: Journal of Geophysical Research. v. 108. no. B4, 1-23.
- Gaedicke, C., Baranov, B., Seliverstov, N., Alexeiev, D., Tsukanov, N., Freitag, R., 2000. Structure of an active arc–continent collision area: the Aleutian–Kamchatka junction: Tectonophysics. v. 325, 63–85.
- Geist, E.L., Scholl, D.W., 1994. Large-scale deformation related to the collision of the Aleutian Arc with Kamchatka: Tectonics. v. 13. no. 3, 538–560.
- Gorbatov, A., Suarez, G., Kostoglodov, V. & Gordeev, E., 1994. A double-planed seismic zone in Kamchatka from local and teleseismic data: Geophys. Res. Lett. v. 21, 1675–1678.
- Gorbatov, A., & Kostoglodov, V., 1997. Maximum depth of seismicity and thermal parameter of the subducting general empirical relation and its application: Tectonophysics. v. 277, 165-187.
- Gorbatov, A., Kostoglodov, V., Suarez, G., Gordeev, E.I., 1997. Seismicity and structure of the Kamchatka subduction zone: J. Geophys. Res. B 102 (8), 17883–17898.

Gorbatov, A., Dominguez, J., Suarez, G., Kostoglodov, V., Zhao, D., & Gordeev, E., 1999.

Tomographic imaging of the P-wave velocity structure beneath the Kamchatka peninsula:

Geophysics Journal International. v. 137, 269-279.

Gordeev, E.I., Gusev, A.A., Levina, V.I., Leonov, V.L., Chebrov, V.A., 2004. Crustal seismicity of Kamchatka. AGU Fall Meeting: EOS Trans. AGU. 85(47), Fall Meet. Suppl., Abstract T11D-1282.

Gulick, S., Hanks, T. C. (2000). The Age of Scarplike Landforms From Diffusion-Equation Analysis. *American Geophysical Union*, 313-338.

Hanson, K.L., Swan, F.H., and Schwartz, D.P., 1981. Study of earthquake recurrence intervals on the Wasatch fault, Utah: San Francisco, California, Woodward-Clyde Consultants, Sixth-annual technical report prepared for U.S. Geological Survey under contract. No. 14-08- 0001-19115, p. 22.

Hanks, T.C., Bucknam, R.C., Lajoie, K.R., and Wallace, R.E., 1984. Modification of wave-cut and faulting controlled landforms: *Journal of Geophysical Research*. v. 89, 5571-5790.

Hanks, T.C., 2000. The age of scarp like landforms from diffusion-equation analysis, in *Quaternary geochronology—methods and applications*, Noller, J.S., Sowers, J.M., and Lettis, W.R., editors, American Geophysical Union reference shelf, v. 4: Washington, D.C. American Geophysical Union. p. 313-338.

Harty, K.M., Mulvey, W.E., and Machette, M.N., 1997. Surficial geologic map of the Nephi segment of the Wasatch fault zone, eastern Juab County, Utah: Utah Geological Survey Map 170, scale 1:50,000.

Haugerud, R. H. (2003). High-resolution Lidar topography of Puget Lowland, Washington—A Bonanza for Earth Science. *GSA Today*, 4-10.

- Hochstaedter, A.G., Kepezhinskas, P.K., Defant, M.J., Drummond, M. S., Bellon, H., 1994. On the tectonic significance of arc volcanism in northern Kamchatka: *J. Geol.* v.102, 639–654.
- Izbekov, P. E., Eichelberger, J. C., Patino, L. C., Vogel, T. A., & Ivanov, B. V., 2002. Calcic cores of plagioclase phenocrysts in andesite from Karymsky: *Geological Society of America.* v. 30. no. 9, 799-802.
- Izbekov, P., Gardner, J. E., & Eichelberger, J. C., 2004. Comagmatic granophyre and dacite from Karymsky volcanic: *Journal of Volcanology and Geothermal Research.* v. 131, 1-18.
- Jackson, M., 1991. Number and timing of Holocene paleoseismic events on the Nephi and Levan segments, Wasatch fault zone, Utah: *Utah Geological Survey Special Studies*, v. 78, 23.
- Jaeger, J.M., Hallet, B., Pavlis, T., Sauber, J., Lawson, D., Milliman, J., Anderson, S., and Anderson, R., 2001, Orogenic and glacial research in pristine southern Alaska: *Eos (Transactions, American Geophysical Union)*, v. 82, p. 213–216, doi: 10.1029/01EO00112.
- Kao, H. and Chen, W., 1994. The double seismic zone in Kuril-Kamchatka: The tale of two overlapping single zones: *Journal of Geophysical Research.* v. 99, no. B4, 6913-6930.
- Kamata, H., & Kodama, K., 1999. Volcanic history and tectonics of the Southwest Japan Arc: *The Island Arc.* v. 8, 393-403.
- Kelsey, H. M., Sherrod, B. L., Nelson, A. R., & Brocher, T. M. (2008). Earthquakes generated from bedding plane-parallel reverse faults above an active wedge thrust, Seattle fault zone. *Geological Society of America Bulletin*, 1581-1597.
- Kepezhinskas, P.K., 1987. Origin of Cenozoic volcanic series of Komandorsky basin framing according to geochemical and experimental data: *Geologicky Zbornik-Geologica Carpathica.* v. 38, 71–81.
- Konstantinovskaya, E.A., 2003. Margins of East Asia: tectonics, structural evolution and geodynamic modeling: *Transactions 549 Scientific World.* Moscow. p. 223 (in Russian).

- Kozhurin, A.I., 1988. The Kuril–Kamchatka island arc: neotectonic zoning, Late Quaternary structure of Central Kamchatka, tectonic layering of the lithosphere in Central Kamchatka, some general features of the neotectonic structures of the circum-Pacific mobile belt. In: *Neotektonika i sovremennaya geofinamika podvizhnykh poyasov*. Nauka, Moskva. pp. 67–115 and 135–151 (in Russian).
- Kozhurin, A.I., 1990. Recent strike-slip faults in the Kumroch Range and Kamchatsky peninsula area, Eastern Kamchatka: *Tikhookeanskaya Geologiya*. v. 6, 45–55 (in Russian).
- Kozhurin, A., 2004. Active faulting at the Eurasian, North American: *Tectonophysics*. v. 380, 273-285.
- Kozhurin, A., Vocella, V., Kyle, P.R., Lagmay, F.M., Melekestsev, I. V., Ponomareva, V., Rust, D., Tibaldi, A., Tunesi, A., Corazzato, C., Roviola, A., Sakharov, A., Tengonciang, A., Uy, H., 2006. Trenching studies of active faults in Kamchatka, eastern Russia: Palaeoseismic, tectonic and hazard implications: *Tectonophysics*. v. 417, 285-304.
- Kozhurin, A., 2007. Kamchatka island arc: two modes of extension in the overriding plate: *Geophysical Research Abstracts*, v. 9.
- Kozhurin, A.I., Ponomareva, V.V., Pinegina, T.K., 2008. Active faulting in the south of central Kamchatka: *Vestnik KRAUNTS Nauki o zemle*, v. 12. no. 2, 10-27 (in Russian).
- Legler, V.A., 1976. Deformation of the subducting lithospheric plate and longitudinal shifts of the Kuril–Kamchatka island arc. *Tectonics of the Lithospheric Plates (Dynamics of the Subduction Zone)*. P.P.Shirshov. Institute of Oceanology AN SSSR, Moscow, p. 103–147 (in Russian).
- Levin, V., Shapiro, M., Park, J., Ritzwoller, M., 2002. Seismic evidence for catastrophic slab loss beneath Kamchatka: *Nature*. v. 418, 763–767.
- Li, Z., Bruhn, R., Pavlis, T., Vorkink, M., & Zeng, Z. (2010). Origin of sackung uphill-facing scarps in the Saint Elias orogen, Alaska: LIDAR data visualization and stress modeling. *Geological Society of America Bulletin*, 1585-1599.

- Mackey, K., Fujita, K., Gunbina, L., Kovalev, V., Imaev, V., Koz'min, B., Imaeva, L., 1997. Seismicity of the Bering Strait region: evidence for a Bering block: *Geology*. v. 25/11, 979–982.
- Mattson, A., & Bruhn, R. L., 2001. Fault Slip-rates and Initiation Age Based on Diffusion Equation Modeling: Wasatch Fault Zone and Eastern great Basin: *Journal of Geophysical Research*. v. 106. no. B7, 13,739-13,750.
- McCalpin, J.P., Bruhn, L. R., Pavlis, L. T., Gutierrez, F., Guerrero, J., Lucha, P., 2011. Antislope scarps, gravitational spreading, and tectonic faulting in the western Yakutat microplate, southe coastal Alaska. *Geosphere*, 1143-1158.
- Meigs, A., and Sauber, J., 2000, Southern Alaska as an example of the long-term consequences of mountain building under the influence of glaciers: *Quaternary Science Reviews*, v. 19, p. 1543–1562, doi:10.1016/S0277-3791 (00)00077-9.
- Melekestsev, I.V., 1974. Main stages of development of the modern relief of the Kuril–Kamchatka region. In: Luchitsky, I.V. (Ed.), *History of Relief Development in Siberia and Far East Kamchatka, the Kuril and Komandor Islands*: Nauka, Moscow, p. 337–344 (in Russian).
- Miller, D.J., 1961, *Geology of the Katalla district, Gulf of Alaska Tertiary Province, Alaska*: U.S. Geological Survey Open-File Report.
- Move2012.1. A complete structural modelling solution for 2D and 3D structural modelling. Midland Valley Exploration.
- Muller, J. R. (2007). Using LIDAR Surface Deformation Mapping to Constrain Earthquake Magnitudes on the Seattle Fault in Washington State, USA. *Urban Remote Sensing Joint Event*.
- Nash, D.B., 1980. Morphologic dating of degraded normal fault scarps: *Journal of Geology*, v. 88, 353-360.

- Nelson, A.R., and Personius, S.F., 1993. Surficial geologic map of the Weber segment, Wasatch fault zone, Weber and Davis Counties, Utah: U.S. Geological Survey Miscellaneous Investigations Series Map I-2199, v. 22. p. pamphlet, scale 1:50,000.
- Page, J. S., 2001. Fold-thrust system overprinting syn-rift structure on the margin of an inverted rift basin: Indio Mountains, West Texas [MS thesis]. University of Texas at El Paso, 68 p.
- Park, J., Levin, V., Lees, J., Peyton, V., Gordeev, E., Ozerov, A., 2002. A dangling slab, amplified arc volcanism, mantle flow and seismic anisotropy in the Kamchatka Plate Corner. In: Stein, S., Freymueller, J.T. (Eds.), Plate Boundary Zones. Geodynamics Series, v. 30, 295–324.
- Pavlis, T.L., Picornell, C., Serpa, L., Bruhn, R.L., and Plafker, G., 2004, Tectonic processes during oblique-collision: Insights from the Saint Elias orogen, northern North American Cordillera: Tectonics, v. 23, TC3001, 14 p., doi:10.1029/2003TC0011557.
- Pavlis, T. L., & Bruhn, R., 2011. Application of LIDAR to resolving bedrock structure in areas of poor exposure: An example from the STEEP study area, southern Alaska. *The Geological Society of America Bulletin*. 206-217.
- Pedoja, K., Bourgeois, J., Pinegina, T., and Higman, B., 2006. Does Kamchatka belong to North America? An extruding Okhotsk block suggested by coastal neotectonics of the Ozernoi Peninsula, Kamchatka, Russia: Geology. v. 34, 353-356. doi: 10.1130/G22062.1.
- Perritt, S., & Roberts, M. (2007). Flexural-slip structures in the Bushveld Complex, South Africa? *Journal of Structural Geology*, 1422-1429.
- Pinegina, T.K., Kozhurin, A.I., and Ponomareva, V.V., 2012. Seismic and tsunami hazard for the Ust-Kamchatsk village, Kamchatka, from paleoseismological investigations: Vestnik KRAUNTS Nauki o zemle. v. 19, p. 138-159 (in Russian).
- Plafker, G., 1969, Tectonics of the March 27, 1964, Alaska Earthquake: U.S. Geological Survey Professional Paper 543-I, 74 p.

- Plafker, G., 1987, Regional geology and petroleum potential of the northern Gulf of Alaska continental margin, in Scholl, D.W., Grantz, A., and Vedder, J.G., eds., *Geology and resource potential of the continental margin of western North America and adjacent ocean basins: Beaufort Sea to Baja California*: Houston, Circum-Pacific Council for Energy and Mineral Resources, Earth Science Series, p. 229–268.
- Plafker, G., Moore, J.C., and Winkler, G.R., 1994, Geology of the southern Alaska margin, *in* Plafker, G., and Berg, H.C., eds., *The Geology of Alaska*: Boulder, Colorado, Geological Society of America, *Geology of North America*, v. G-1, p. 389–449.
- Plafker, G., and Thatcher, W., 2008. Geological and geophysical evaluation of the mechanisms of the great 1899 Yakutat Bay earthquakes, Freymueller, J.T., et al., eds., *Active Tectonics and Seismic Potential of Alaska*: American Geophysical Union Geophysical Monograph. v. 179, p. 215–236.
- Portnyagin, M., and Manea, V. C., 2008. Mantle temperature control on composition of arc magmas along the Central Kamchatka Depression: *Geology*. v. 36, 519–522. doi: 10.1130/G24636A.1.
- Ruppert, N. A., Lees, J. M., & Kozyreva, N. P., 2007. Seismicity, Earthquakes and Structure along the Alaska-Aleutian and Kamchatka-Kurile Subduction Zones: A Review. *Geophysical Monograph Series* 172. doi: 10.1029/172GM12.
- Ruppert, N. A., Ridgeway, K. D., Freymueller, J. T., Cross, R. S., and Hansen, R. A., 2008. *Active Tectonics of Interior Alaska: Seismicity, GPS Geodesy, and Local Geomorphology*. *Geophysical Monograph Series* 179. American Geophysical Union. doi: 1029/179GM06
- Saltykov V.A., Kugaenko Yu.A., 2000. Seismic quiescence before two strong earthquakes on Kamchatka, 1996: *Journal of Volcanology and Seismology*. v. 22. no. 1, 87–98.
- Scharman, R. M., Palis, L. T., Day, M. E., and O'Driscoll, J. L., 2011. Deformation and structure in the Chugach metamorphic complex, southern Alaska: Crustal architecture of a transpressional system from a down plunge section. *Geosphere*, 992–1012.

- Shennan, I., Bruhn, B., and Plafker, G., 2008 Multi-segment earthquakes and tsunami potential of the Aleutian megathrust. *Quaternary Science Reviews*, 7-13.
- Spencer, E. J., 2010. Structural analysis of three extensional detachment faults with data from the 2000 Space-Shuttle Radar Topography Mission. *GSA Today*. 4-10.
- Svyatlovsky, A. E., 1867. Outline of History of Quaternary Volcanism of Kamchatka: Nauka, Moscow. p. 219 (in Russian).
- Thorleifson, H., Berg, C. R., Russell, A.J.H., 2010. Geological mapping goes 3-D in response to societal needs. *GSA Today*. 27-29.
- Tikoff, B., and Teyssier, C., 1992. Crustal-scale, en echelon “P-shear” tensional bridges: a possible solution to the batholithic room problem: *Geology*. v. 20, 927-930.
- Tikhonov, V.I., 1968. Thrust faults in East Kamchatka: *Geotektonika*. v. 3, p. 88–101 (in Russian).
- Wallace, R.E., 1977. Profiles and ages of young fault scarps, north–central Nevada: *Geological Society of America Bulletin*. v. 88, 1267- 1281.
- Tuthill, S.J., and Laird, W.M., 1966, Geomorphic effects of the earthquake of March 27, 1964, in the Martin-Bering rivers area, Alaska: U.S. Geological Survey Professional Paper 543-B, 29 p.
- Tysdal, G.R., Hudson, T., and Plafker, G., 1976. Geologic Map of the Cordova D-1 quadrangle and northern part of the Cordova A-2 quadrangle, south-central Alaska: U. S. Geological Survey Miscellaneous Field Studies Map MF-783, scale 1:63 360. 1 sheet.
- Wallace, R.E., 1977, Profiles and ages of young fault scarps, north–central Nevada: *Geological Society of America Bulletin*, v. 88, p. 1267-1281.
- Wells, D. L. (1994). New Empirical Relationships among Magnitude, Rupture Length, Rupture Width, Rupture Area, and Surface Displacement. *Bulletin of the Seismological Society of America*, 974-1002.

- Winkler, G.R., and Plafker, G., 1993, Geologic map of the Cordova and Middleton Island quadrangles, southern Alaska: U.S. Geological Survey Map I-1984, scale 1:250,000.
- Yeats, R. S., 1986, Active faults related to folding, in Active tectonics: Washington, D.C., National Academy Press, p. 63–79.
- Yogodzinski, G.M., Lees, J.M., Churikova, T.G., Dorendorf, F., Wörner, G., Volynets, O.N., 2001. Geochemical evidence for the melting of subducting oceanic lithosphere at plate edges: *Nature*. v. 409, 500–504.
- Zhiyong, L., Bruhn, L. R., Pavlis, L. T., Vorkink, M., Zuoxun, Zeng,. 2010. Origin of sackung uphill-facing scarps in the Saint Elias orogen, Alaska: LIDAR data visualization and stress modeling. *Geological Society of America Bulletin*, 1585-1599.

Vita

Dr. Sarah N. Heinlein was born and raised in El Paso, Texas as Sarah N. Alvarez the daughter of Catalina Alvarez and biological Father Raul Alvarez (who she only saw twice in her life). She graduated from Montwood High School as Sarah N. Cervera in the spring of 1998 happy to take the surname of her stepfather Arturo Cervera.

Dr. Heinlein earned her bachelor's degree in Geology in the fall of 2004 and her master's degree in Geology in the fall of 2006 from the University of Texas at El Paso. After completing her MS she taught GEOL 1311 in the spring of 2007. She accepted a position as Geomorphologist with TRC Solutions Inc. from 2007 to 2008. In the summer of 2008 she decided to return to UTEP to pursue her PhD in Geology. She married her husband John Heinlein in the spring of 2012 and they welcome their son in the spring of 2013.

Dr. Heinlein has been the recipient of numerous honors and awards including Outstanding Thesis award, Vernon G. and Joy Hunt Endowed Scholarship, and ConocoPhillips Scholarship through the University of Texas at El Paso Geological Sciences Department. She was also a recipient of numerous UTEP Geology Department Annual Colloquium presentation awards as well as a SACNAS national conference awardee. While pursuing her degree, Dr. Heinlein worked as a Scientist in Residence for the UTEP GK-12 program (NSF funded) and interned as an NSF Researcher with the University of Alaska Fairbanks PIRE project.

Dr. Heinlein dissertation entitled, "*Application of Various Remote Sensing and Aerial Photography Data Sets to Resolve Surface Structure in Areas of Poor Exposure: Examples from Kamchatka Peninsula, Russia and Katalla Area, Alaska USA*" was supervised by Dr. Terry L. Pavlis.

Dr. Heinlein has recently accepted a position as Geologist with WorleyParsons Group INTECSEA in Houston Texas, USA.

Permanent address: 4331 Haven Glen Dr.
Kingwood, Texas 77339

This dissertation was typed by Sarah Natalie Heinlein.